SANDIA REPORT

SAND2005-2340
Unlimited Release
Printed May 2005

Design and Fabrication of a Meso-scale Stirling Engine and Combustor

Brent Haroldsen
Jacqueline Chen
Alfredo M. Morales
Michelle A. Hekmaty
Karen L. Krafcik
Tom Raber
Bernice Mills
Joseph T. Ceremuga
Tarek Echekki
Jeremiah Lee
Shiling Liu
Adonis Karpetis

Prepared by
Sandia National Laboratories
Albuquerque, New Mexico 87185 and Livermore, California 94550

Sandia is a multiprogram laboratory operated by Sandia Corporation,
a Lockheed Martin Company, for the United States Department of Energy's
National Nuclear Security Administration under Contract DE-AC04-94AL85000.

Sandia National Laboratories

Issued by Sandia National Laboratories, operated for the United States Department of Energy by Sandia Corporation.

Available to DOE and DOE contractors from
U.S. Department of Energy
Office of Scientific and Technical Information
P.O. Box 62
Oak Ridge, TN 37831

Telephone: (865)576-8401
Facsimile: (865)576-5728
E-Mail: reports@adonis.osti.gov
Online ordering: http://www.osti.gov/bridge

Available to the public from
U.S. Department of Commerce
National Technical Information Service
5285 Port Royal Rd
Springfield, VA 22161

Telephone: (800)553-6847
Facsimile: (703)605-6900
E-Mail: orders@ntis.fedworld.gov
Online order: http://www.ntis.gov/help/ordermethods.asp?loc=7-4-0#online

SAND2005-2340
Unlimited Release
Printed May 2005

Design and Fabrication of a Meso-Scale Stirling Engine and Combustor

Brent L. Haroldsen, Jacqueline Chen, Alfredo M. Morales, Michelle A. Hekmaty, Karen L. Krafcik, Tom Raber, Bernice Mills, Joseph T. Ceremuga, Tarek Echekki, Jeremiah Lee, Shiling Liu, Adonis Karpetis

Sandia National Laboratories
PO Box 969
Livermore, CA 94551-0969

ABSTRACT

Power sources capable of supplying tens of watts are needed for a wide variety of applications including portable electronics, sensors, micro aerial vehicles, and mini-robotics systems. The utility of these devices is often limited by the energy and power density capabilities of batteries. A small combustion engine using liquid hydrocarbon fuel could potentially increase both power and energy density by an order of magnitude or more. This report describes initial development work on a meso-scale external combustion engine based on the Stirling cycle. Although other engine designs perform better at macro-scales, we believe the Stirling engine cycle is better suited to small-scale applications. The ideal Stirling cycle requires efficient heat transfer. Consequently, unlike other thermodynamic cycles, the high heat transfer rates that are inherent with miniature devices are an advantage for the Stirling cycle. Furthermore, since the Stirling engine uses external combustion, the combustor and engine can be scaled and optimized semi-independently. Continuous combustion minimizes issues with flame initiation and propagation. It also allows consideration of a variety of techniques to promote combustion that would be difficult in a miniature internal combustion engine.

The project included design and fabrication of both the engine and the combustor. Two engine designs were developed. The first used a cylindrical piston design fabricated with conventional machining processes. The second design, based on the Wankel rotor geometry, was fabricated by through-mold electroforming of nickel in SU8 and LIGA micromolds. These technologies provided the requisite precision and tight tolerances needed for efficient micro-engine operation. Electroformed nickel is ideal for micro-engine applications because of its high strength and ductility. A rotary geometry was chosen because its planar geometry was more compatible with the fabrication process. SU8 lithography provided rapid prototypes to verify the design. A final high precision engine was created via LIGA.

The micro-combustor was based on an excess enthalpy concept. Development of a micro-combustor included both modeling and experiments. We developed a suite of simulation tools both in support of the design of the prototype combustors, and to investigate more fundamental aspects of combustion at small scales. Issues of heat management and integration with the micro-scale Stirling engine were pursued using CFD simulations. We found that by choice of the operating conditions and channel dimensions energy conversion occurs by catalysis-dominated or catalysis-then-homogeneous phase combustion.

The purpose of the experimental effort in micro-combustion was to study the feasibility and explore the design parameters of excess enthalpy combustors. The efforts were guided by the necessity for a practical device that could be implemented in a miniature power generator, or as a stand-alone device used for heat generation. Several devices were fabricated and successfully tested using methane as the fuel.

ACKNOWLEDGEMENTS

We would like to thank the LIGA team at Sandia, California (orgs. 8753 and 8751), for the fabrication of SU8 and LIGA parts. Lois Johnston is gratefully acknowledge for assistance with radiography. Sandia is a multiprogram laboratory operated by Sandia Corporation, a Lockheed Martin Company, for the United States Department of Energy under contract DE-AC04-94AL85000.

TABLE OF CONTENT

This page intentionally left blank.

INTRODUCTION

Justification for micro engines

There is an increasing demand for small, high-density power sources for both military and consumer applications [ref. 1,2]. Almost any device that currently uses batteries could benefit from an improved power source. Consumer applications for micro-power generation include power tools (drills, saws, vacuum cleaners, etc), laptop computers, video recorders, cell phones, pagers, hearing aids, smoke detectors, and burglar alarms. Similarly, Table 1 shows components of the Land Warrior Program with their power requirements [ref. 3]. Estimates of the energy density needed to meet the future requirements for that program range from 794 Wh/kg to 4763 Wh/kg [ref. 4]. By comparison the MIL/BA5590/U Lithium Sulfur Dioxide battery has a gravimetric energy density of about 230 Wh/kg. For many military applications, the available power technology determines the mission profile. This has lead DARPA to invest heavily in micro-power technology under the Palm Power program, the MEMS Micro Power Generation program, and the Micro Aerial Vehicle Program [ref. 5].

Table 1: Land Warrior Subsystems[3]

Subsystem	Operating Power W)
Computer	14.8
Hand-Held Flat Panel Display	6.4
Soldier Radio	
Receive	1.4
Transmit	6.0
Squad Radio	
Receive	2.0
Transmit	12.0
Global Positioning System	1.5
Video Capture	1.0
Laser Detectors	0.6
Helmet-Mounted Display	4.9
Image Intensifier with Integrated Flat Panel Displays	0.1
Laser Rangefinder	0.1
Laser Aiming Light	0.1
Digital Compass	0.4
Thermal Weapon Sight/Close Combat Optic	5.5
TOTAL	57.0

The energy density of liquid hydrocarbons is almost two orders of magnitude larger than the best batteries. For example the enthalpy of combustion for octane (lower heating value) is 12,300 Wh/kg. Consequently, even if an engine is only twenty percent efficient, it will still be ten times better than a battery in terms of energy storage density. In short, a micro-power source using a liquid hydrocarbon fuel offers the potential for an order of magnitude or more improvement over the best batteries.

Other work

Table 2 includes several examples of recent or on-going micro engine research projects. The term "micro engine" encompasses a range of sizes. Some researchers use the term to refer to MEMS devices with characteristic dimensions of micrometers. Others refer to engines with one millionth of the output of industrial scale engines. In most cases, including this report, micro engine is a generic term for small engines designed to produce from 1 to 100 watts. This size range is based primarily on the large number of potential applications. The term Meso-scale is also used to describe this size range and might be more accurate.

Table 2: Examples of Micro-Engine Programs

University or company	Engine type	Power range
MIT	Gas turbine	~50 Watts
UC Berkeley	Wankel engine	~30 Watts
Honeywell	Free piston HCCI engine	~50 mW
Georgia Tech	Free piston engine	
GE	Piston engine	
D-Star	Diesel engine	
USC	Thermoelectric generator	~100 mW
Washington State	Palouse Piezoelectric Power	
M-DOT	Gas turbine for micro UAV	

Scaling laws

Table 3 shows how various physical parameters scale with length according to classical scaling laws. These relationships can be used to estimate the size and performance of a micro-engine. For example, assume that a macro-scale engine produces 90 kW, weighs 135 kg (300 pounds), and has dimensions of 0.3 m X 0.3 m X 0.6 m (1 ft X 1 ft X 2 ft). Since power scales with the length squared, the linear scaling factor for a 20 watt engine is:

$$\text{Scale Factor} = (20/90{,}000)^{0.5} = 0.015.$$

Assuming the scaling laws apply, the dimensions of the micro-engine can be calculated by multiplying the dimensions of the macro-engine by the scaling factor:

$$(0.3\text{ m})(1000\text{ mm/m})(0.015) = 4.5\text{ mm}$$

The dimensions of the micro-engine would be 4.5 mm by 4.5 mm by 9 mm. Similarly, the weight is proportional to the cube of the length so the estimated weight of the micro-engine is:

$$W = (135\text{ kg})(0.015)^3 = 0.45\text{ grams.}$$

Table 3: Scaling Laws

Area (A) $\propto L^2$	Power $\propto W/t \propto L^2$
Volume (V) $\propto L^3$	Torque $\propto F*L \propto L^3$
Mass (M) $\propto V \propto L^3$	Angular velocity (ω) $\propto \theta/t \propto 1/L$
Pressure (P) $\propto 1$	Angular acceleration $\propto \theta/t^2 \propto 1/L^2$
Strength $\propto L^2$	Ang. momentum $\propto \omega*L^2*M \propto L^4$
Force (F) $\propto P*A \propto L^2$	Deformation $\propto F/S \propto L$
Stiffness (S) $\propto A/L \propto L$	Viscous stress $\propto v/L \propto 1/L$
Time (t) $\propto L$	Friction force $\propto L^2$
Velocity (v) $\propto L/t \propto L/L \propto 1$	Life $\propto$ L/erosion rate $\propto L$
Acceleration $\propto v/t \propto 1/L$	Heat capacity $\propto V \propto L^3$
Frequency $\propto 1/t \propto 1/L$	Thermal conductance $\propto A/L \propto L$
Work (W) $\propto F * L \propto L^3$	Thermal time constant $\propto L^2$

By comparison, a battery for a laptop computer might weight 250 grams and produce 50 watt-hours of electricity. Table 4 shows the attributes of two common batteries – one military and one commercial. Figure 1 shows the comparison in size and weight between a Lithium Sulfur Dioxide battery and an engine using heptane assuming different efficiencies and different fuel storage capacities. A 20-percent-efficient engine with 70 grams of fuel would deliver the same energy as a battery but would be 14 percent of the volume and 7 percent of the weight. Similarly, for the same weight, the engine would last 15 times as long.

Table 4: Attributes of Lithium Ion Batteries

	BA-5590 (military)	Polystor (commercial)
Power	50 W	7.4 W
Volume	880 cc	13.9 cc
Weight	1100 grams	38.5 grams
Volumetric density	200 W-hr/li	360 W-hr/li
Gravimetric density	160 W-hr/kg	130 W-hr/kg

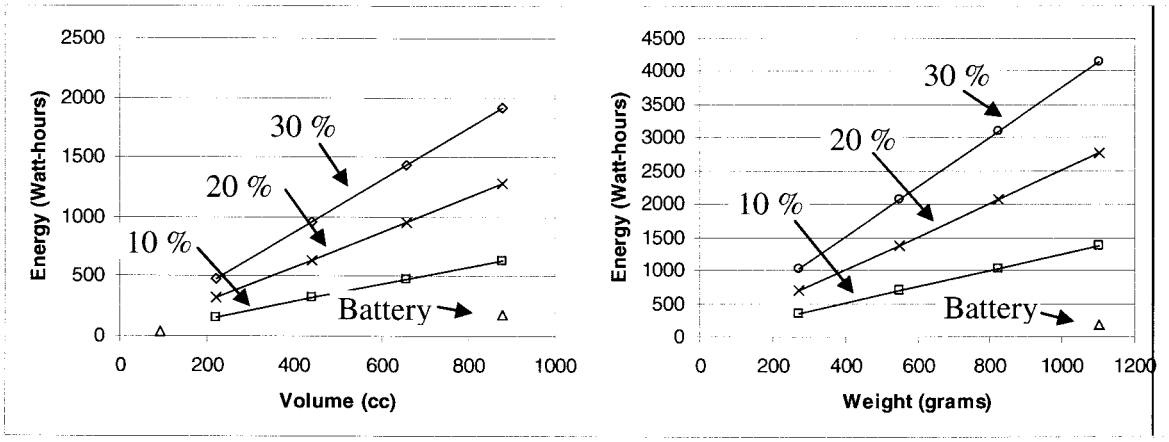

Figure 1: Comparison of Lithium Sulfur Dioxide Batteries and micro-engines

The scaling laws also provide insights into important attributes and potential problems with micro-engines. Perhaps most important of these is heat transfer. As the scale gets smaller, the ratio of surface area to volume gets larger and heat transfer becomes more important. The thermal time constant scales with the length squared, so temperatures equilibrate much more quickly than in a macro-scale engine. Consequently, the reduced scale should benefit thermal cycles that are based on isothermal processes, but will be detrimental to those with adiabatic processes. Regardless of the engine cycle, however, heat losses will be proportionately greater in a micro-engine. Furthermore, all heat engines operate between a high temperature source and a low temperature sink and the maximum thermal efficiency is proportional to the temperature difference between them. As the distance separating the hot and cold regions of the engine decreases, it becomes increasingly difficult to maintain a large temperature difference. This presents a fundamental obstacle to the efficient operation of a micro-engine.

Other important scaling attributes concern time and operating frequency. Frequency is inversely proportional to the linear scaling factor, meaning that a small engine should operate at high speed. In the example above, if the large engine operates at 3000 rpm, the scaled micro-engine would operate at 200,000 rpm. Similarly, the life of the engine, in hours of operation, will scale inversely with the size, so the life of the micro-engine will be proportionately shorter. If we assume the life of the large engine is 3000 hours, the expected life the micro-engine would be only 45 hours, which is comparable to a disposable or non-rechargeable battery. This has several implications. First, the engine must be viewed as a disposable item rather than a durable commodity. Consequently, it must be inexpensive and amenable to mass production. Second, the total amount of fuel that the engine will consume in its functional life is small. Unlike macro-scale engines, which are refueled at regular intervals to minimize the amount of fuel that is stored with the engine, it is completely reasonable to package the micro-engine with enough fuel to last for its entire functional life. This offers several advantages. The entire package can be sealed for improved safety and reliability and there will be no logistics issues associated with fuel supply. Furthermore, the choice of fuel can be based solely on engine performance without regard to availability in the field. For example, instead of using traditional fuels like gasoline or diesel, it can be designed to use a pure hydrocarbon like heptane that is easier to vaporize and less likely to foul the engine.

Three other scaling factors worth noting are viscous stress, angular momentum, and pressure. As the scale decreases, the viscous stress increases, so lubrication is more difficult on micro-engines. Angular momentum scales with length to the fourth power, meaning it is very small in micro-devices. Consequently flywheels do not work well. Pressure is not affected by scale so, in theory, engines of any scale should operate at the same pressure. Generally, the power and efficiency of an engine increase as the operating pressure increases. The operating pressure is chosen as a tradeoff between performance and other factors such as weight or materials of fabrication. As a practical consideration, the cost of materials is less important in micro-devices, the weight of the engine is less significant because it is dominated by the weight of the fuel, and fabrication limitations often result in heavier structures than are needed for the stresses involved. In short, micro-engines do not necessarily have the same trade-offs as macro-scale engines so it might be feasible to operate at considerably higher pressure. In that case, the power density would be greater than predicted by the scaling laws.

The scaling laws also have implications for combustion in micro-devices. The heat generated in a flame is roughly proportional to the volume while the heat loss is proportional to the area. As the size of the flame decreases the heat losses increase relative to the heat generation. At some point, the heat loss will be too great and combustion will no longer occur without catalysts or other methods of enhancing the reaction. Furthermore, the process of igniting and propagating a flame in an internal combustion engine becomes more difficult. For example, the voltage and electrode gap for a sparkplug do not scale, the initiation time and chemical kinetics remain unchanged even though the engine runs much faster, and there is less turbulence to promote uniform mixing and combustion. All of these factors favor engine designs with continuous, external combustion. Specifically, an external combustor can be scaled semi-independently from the engine to accommodate separate scaling concerns, there is no need for repeated flame initiation and propagation, and the design can easily incorporate catalysts and advanced heat management concepts without compromising the engine.

In a real engine, some aspects of the design will not scale per the classical laws. For example, it is unlikely that a micro engine will operate as efficiently as its macro-scale counterpart. This will have little effect on the conclusion of the above analysis, however, since most of the weight is from the fuel. Consequently, the parameter that most affects the size and weight of the system is the efficiency of the engine. In this regard, it is important not to judge the performance of a micro-engine by comparison with an analogous larger engine. Rather, the engine should be judged in comparison with competing power sources in the range of 10 to 100 watts. Large internal combustion engines have benefited from over a hundred years of engineering development and refinement. Furthermore, there are fundamental thermodynamic reasons why a micro-engine will be less efficient. While a large gas turbine with an efficiency of ten percent would be of little interest to an electric utility company, a micro-turbine producing 20 watts at 10 percent efficiency would be an order of magnitude improvement over existing batteries.

This page intentionally left blank.

STIRLING ENGINES

Overview of the Stirling Cycle

A Stirling engine is a closed cycle, external combustion engine. The working fluid is a gas. The ideal Stirling Cycle is shown in Figure 2. From point 1 to 2, the gas is expanded in a constant temperature process. This is the power stroke. During this stroke heat is added from an external source (a combustor in our case). In the second stroke, from 2 to 3, heat is rejected in a constant volume process. Ideally the heat is transferred to a regenerator rather than being lost. The third stroke, from 3 to 4, is a constant temperature compression stroke in which waste heat is rejected. In the final stroke, from 4 to 1, the fluid is heated in a constant volume process, ideally recovering the heat from the regenerator. When used with a regenerator, the theoretical efficiency of the Stirling cycle matches the Carnot efficiency for the same operating temperatures, making it the most efficient engine cycle possible.

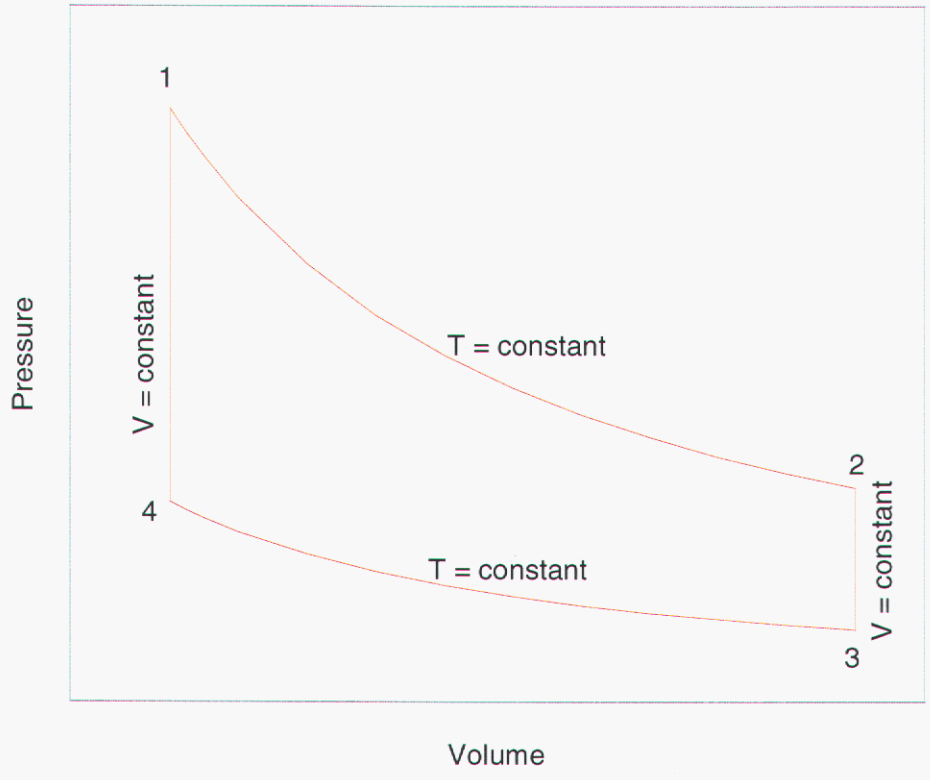

Figure 2: Ideal Stirling Engine Cycle

Practical implementation of the Stirling Cycle

In practice, the cycle can be implemented in various ways. The most common, shown in Figure 3, uses two pistons, typically 90 degrees out of phase. Figure 4 tracks the pistons through the cycle while Figure 5 show the resulting pressure / volume diagram compared to the ideal cycle.

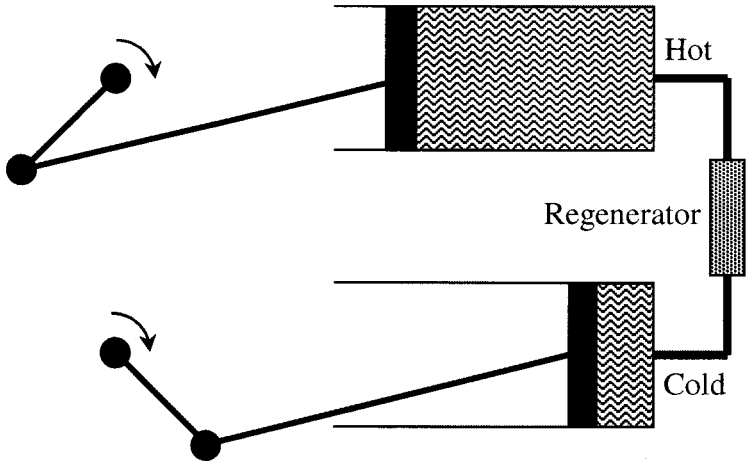

Figure 3: Schematic of a Two Piston Stirling Engine

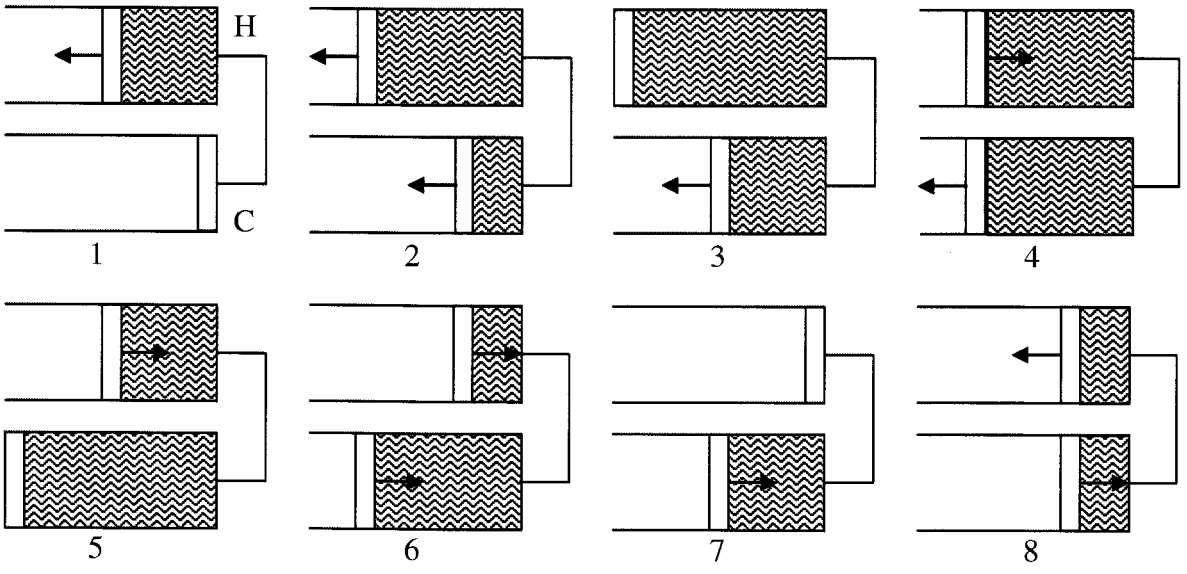

Figure 4: Illustration of Piston Motion Throughout the Engine Cycle

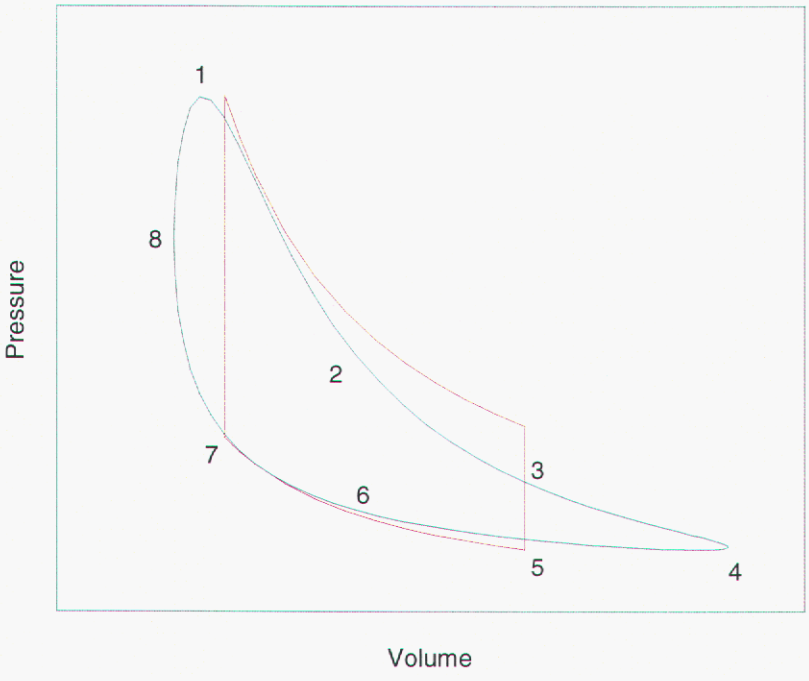

Figure 5: Comparison of Ideal and Real Pressure / Volume Cycle

Several observations can be made from the ideal cycle and the basic engine schematic. Mechanically the Stirling engine is quite simple. There are no valves, no cam shafts, and no spark plugs. Furthermore, the piston geometry is flexible since there are no concerns with turbulence, mixing, and flame propagation. This is advantageous for a micro-engine since the geometry can be chosen to match the capabilities of the fabrication process.

One end of the engine remains at a constant high temperature while the other end remains cold. As with any engine cycle, the greater the temperature difference, the more efficient the engine will be. However, any parasitic heat transfer between the two ends, such as conduction through the structure, decreases the efficiency of the engine. In a micro-engine, the separation between the two ends is small and parasitic heat transfer becomes a bigger concern. This is a fundamental limitation of micro-engines.

The regenerator is a key element of the engine which enables the high theoretical efficiency. In practice, there are at least three inherent losses in the regenerator. First is imperfect heat transfer which prevents 100 percent heat recovery. This is a smaller problem in a micro engine than in a large engine because of the improved heat transfer. Second is parasitic heat transfer from the hot to the cold end of the engine through the regenerator material. Third is pressure loss as the gas flows through the regenerator. Since the feature sizes are small, the Reynolds Number in a micro-engine is inherently low and the flow is laminar. Consequently, the pressure losses are proportionately greater than in a larger engine.

Any unswept or dead volume in the cylinders or in the regenerator decreases the volume ratio (the ratio of the maximum volume to the minimum volume) and will therefore decrease the engine performance. Figure 6 shows the effect if the dead volume is 30 percent of the swept volume. In the extreme case where the dead volume equals the swept volume, the engine will produce no work.

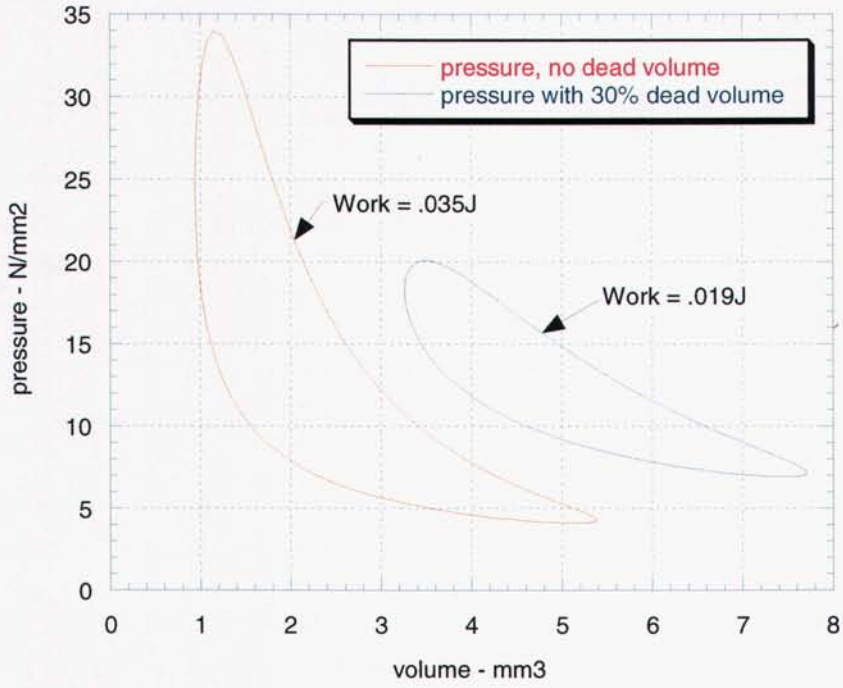

Figure 6: Effect of Unswept Volume on Stirling Engine Performance

Each of the considerations just described places constraints on the design of the regenerator section of the engine. The section must be long enough to provide a reasonable separation between the hot and cold ends of the engine. The flow passages must be large enough to limit the pressure loss. The volume must be small to minimize the dead volume in the engine. Clearly there must be a tradeoff between these competing constraints.

While the efficiency of the ideal cycle depends only on the high and low temperatures, the work per cycle depends on the amount of gas in the working volume and the heat capacity of the gas. Therefore, for a given engine displacement, the work can be increased by increasing the nominal pressure of gas or by selecting a gas with higher heat capacity. The effect of pressure is shown in Figure 7. Since these factors increase the work that is produced without increasing the friction losses, in a real application they should also increase the efficiency. Large Stirling engines frequently use helium or hydrogen as the working fluid because they have good heat transfer properties. In a small engine, where heat transfer is less of a concern, it might be better to use a gas with high specific heat. Since the engine has a fixed volume displacement, it is the molar specific heat that matters, not the mass specific heat.

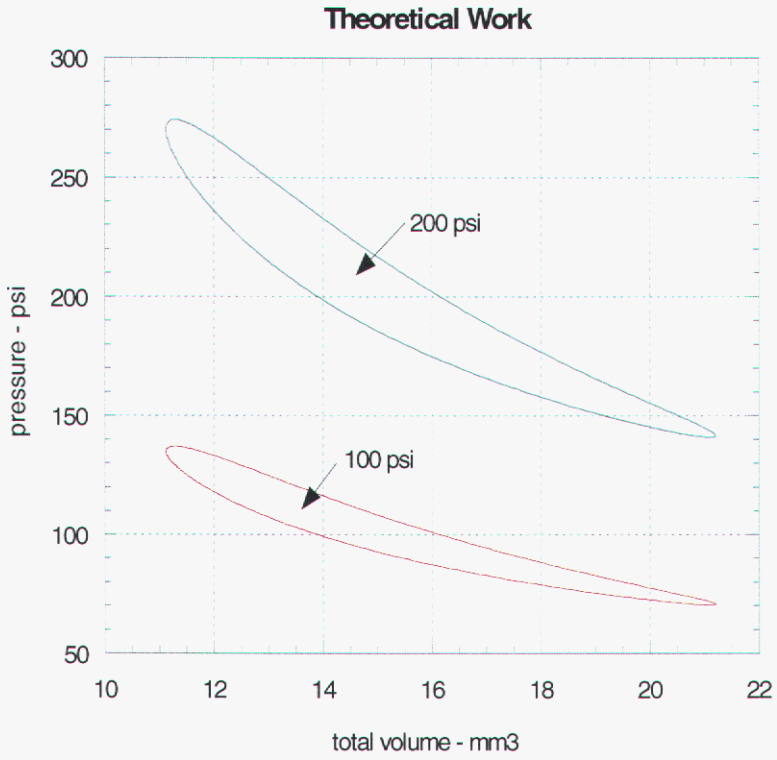

Figure 7: Effect of Mean Operating Pressure on Work

The engine design shown in Figure 3 above requires twice as many pistons and cylinders as a conventional internal combustion engine. In other words, a single volume of gas going through the four strokes of the cycle requires two cylinders. To reduce the number of cylinders, some Stirling engines use a single cylinder with both a piston and a displacer [ref. 6]. This, however, is a more complicated design. Another option is to chain multiple pistons together as shown in Figure 8 so each cylinder has two working volumes and each working volume has two pistons. For a micro-engine, this configuration is less desirable because it places the hot and cold zones too close together. Another option would be to use double-acting hot and cold pistons as shown in Figure 9. This option allows greater separation between the hot and cold zones, but limits the engine to two cylinders. With only two cylinders, there is period when both cycles are in the compression stroke and the combined torque from the engine is negative. Without a flywheel or similar torque leveling mechanism, the engine will stall. As described earlier, flywheels are difficult at small scales.

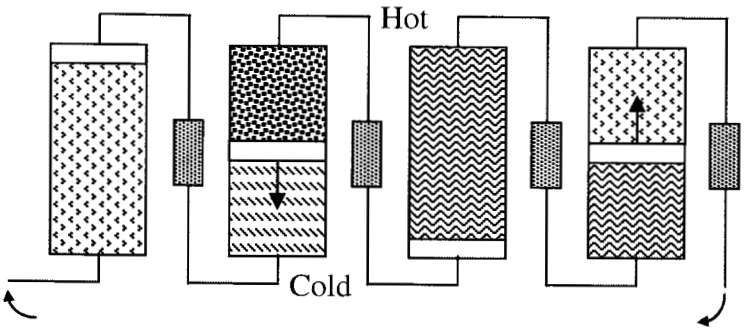

Figure 8: Example of a Four-Pistons Stirling Engine

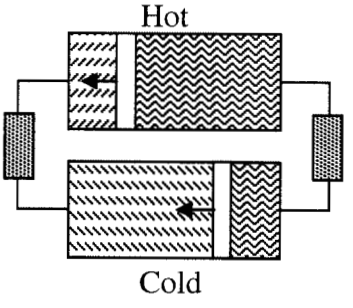

Figure 9: Example of Two-Piston Stirling Engine With Hot and Cold Pistons

Advantages of the Stirling Cycle for Micro-engines

Most meso and micro-engine designs are scaled versions of common macro-engines such as the gas turbine (Brayton Cycle) or internal combustion engine (Otto Cycle). These designs suffer from several inherent scaling effects. The increased ratio of surface area to volume leads to excessive heat loss and decreased efficiency. Micro-fabrication techniques are not compatible with conventional engine geometries and materials. Combustion dynamics and kinetics require different scaling considerations than do the engine mechanisms. The proximity of combustor walls coupled with the comparatively large surface area leads to flame quenching and makes ignition and propagation difficult. Engine seals become more difficult at small scale. Mechanically complex designs with valves, spark plugs, and fuel injectors are difficult to duplicate at a small scale.

In contrast, a Stirling engine should benefit from many scaling effects and offers several advantages for miniaturization. Since the Stirling engine uses external combustion, the combustor and engine can be scaled and optimized semi-independently. Continuous combustion minimizes issues with flame initiation and propagation. It also allows consideration of a variety of techniques to promote combustion such as catalysts, heat recirculation, high-pressure combustion, and novel fuel vaporizers that would be difficult in a micro internal combustion engine.

Unlike other engine cycles in which heat transfer from the working fluid to the walls represents a loss, the Stirling engine requires high heat transfer rates during all four processes in the cycle. Consequently, the Stirling engine should benefit from the proportionately larger surface area at small scale.

The Stirling engine is simple and the geometry is flexible. This means the engine can be designed to enhance the capabilities of micro-fabrication processes, which typically favor planar geometries. Since the engine uses a closed cycle, it can be hermetically sealed. Consequently, the piston seals are less critical than in other engine designs. Furthermore, the internal atmosphere can be completely controlled so the working components are not exposed to corrosive or oxidizing conditions.

Larger Stirling engines have been considered for various applications over the years. The technology was developed extensively in the 50's and 60's by companies such as Philips and General Motors [ref. 6]. Stirling engines have not competed successfully with the established internal combustion engine or gas turbine for several reasons. The Stirling engine is typically larger than the equivalent internal combustion engine. Because part of the engine must operate at a sustained high temperature, it requires more expensive materials of construction such as high-nickel alloys. Furthermore, despite the higher theoretical efficiency, the actual efficiency is comparable to other engine cycles. This to a large extent is because the real compression and expansion processes deviate significantly from the ideal isothermal conditions due to inherent heat transfer limits.

As the scale decreases, these issues all improve. At small scales, the difference in size and weight is insignificant, and is easily outweighed by the factors stated above. The cost of micro devices is determined more by the fabrication process than by the materials and many processes are well suited to high-temperature materials. Temperatures naturally approach isothermal conditions as conduction distances decrease and relative surface area increases. For all of these reasons, the Stirling engine appears to be well suited for micropower applications.

This page intentionally left blank.

MICRO-ENGINE DESIGN

Overview of Engine Project

Sandia's Micro Stirling Engine Project had five major components:

- Develop a model of the micro engine to evaluate design options.
- Design, fabricate, and test a conventionally machined engine.
- Design fabricate, and test an engine using through-mold electroforming in SU8 and LIGA micromolds.
- Develop micro-combustion modeling capability.
- Design, fabricate, and test one or more micro combustors.

The intent of the conventionally-machined engine was to allow us to begin testing quickly. The LIGA process was chosen for the second design because it offered high aspect ratio components, tight tolerances needed for efficient engine operation, the potential for fabrication of multiple parts on a single wafer, and flexibility in materials of construction including nickel or ceramics for high temperature use. It also provides the potential for further scale reduction. Although LIGA parts for the second engine were successfully fabricated, they were not assembled into a full engine before the end of the project due to problems fabricating the center shaft, which was not a LIGA part.

The original plan included development of an integral generator to provide an electrical output from the engine. This was not pursued due to insufficient budget. Instead we purchased a commercial, 17-watt, DC micro motor and coupled it to the output shaft of the engine. The motor is shown in Figure 10. A characteristic of Stirling engines is that they can operate in a reverse mode as a refrigeration or heat pump cycle. Much of the testing was done in this mode, with the electric motor driving the engine. This eliminated the need for a combustor during the testing. The engine and combustor were developed separately.

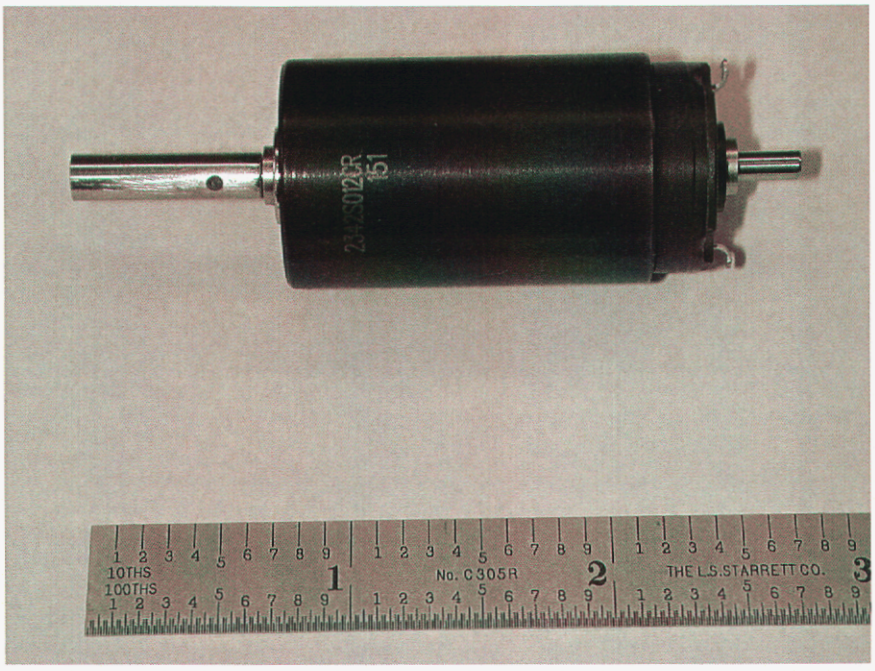

Figure 10: Micro Motor Used With Micro Stirling Engine

Engine Model

We developed a detailed computer model of the engine that calculates the mass, temperature, and pressure of gas in each volume of the engine throughout the complete cycle and calculates work and torque. Using this model we performed parametric studies to select the size and operating conditions. Items of particular interest were the pressure loss in the regenerator and the effects of leakage past the pistons. Figure 11, for example, shows the estimated loss in performance for leakage past a 1 micron gap around the piston. The model did not account for heat transfer, but simply imposed a temperature on the gas at each location.

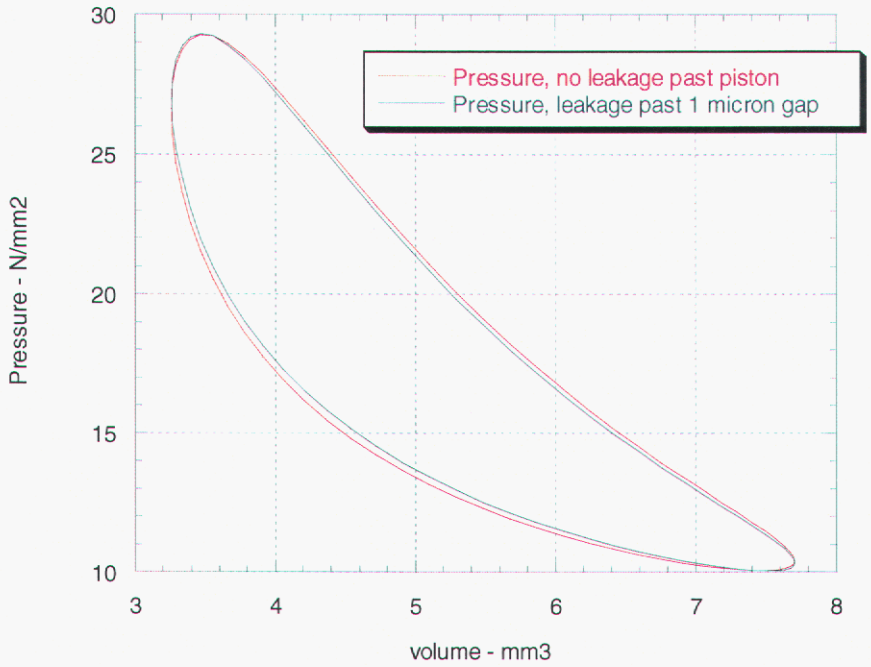

Figure 11: Calculated Loss In Performance Due to a 1 micron Gap Around the Pistons

Engine Designs

With both engine designs we wanted to operate at an elevated nominal pressure for the reasons described earlier. For the system to remain pressurized over a reasonable storage and operating life, there must be a hermetic seal between the engine and the outside atmosphere. Consequently, the primary seal to the outside cannot be a dynamic seal, since such seals will always have some leakage. With the simplest Stirling engine configuration, shown in Figure 3, the primary seal occurs at the piston rings, which is a sliding seal. With this design, any leakage past the piston seal is lost. With a double-acting piston as shown in Figure 8 or Figure 9, leakage past the piston results in reduced work on each cycle, but no loss of gas from the system. However, these designs require a dynamic seal around the piston rods, so they still have the same basic problem. Ultimately we chose to place all moving components, including the crankshaft and the electrical generator, inside the pressurized volume so only the wires penetrated outside of the boundary. That way there were no dynamic seals to the outside and the entire assembly could be hermetically sealed.

Piston Engine

For the conventionally machined engine, we opted for cylindrical pistons in a rotary configuration as shown in Figure 12. There were two hexagonal pistons blocks (Figure 13) – one at the hot end and one at the cold end – separated by a Macor ceramic block that served as a thermal insulator and regenerator housing (Figure 14). Each cylinder in the hot end was connected by a capillary tube through the ceramic block to a corresponding cylinder in the cold end. The metallic capillary walls served as the regenerators. Later we tried a steel regenerator housing also. The regenerator housing also held miniature ball bearings for the crankshaft (Figure 14). Initially the engine used a Macor crankshaft, but it was replaced later with a steel shaft.

A minimum of three piston pairs are needed to maintain a positive torque at all angles of the crank shaft. We designed the system with six simply because they fit conveniently in the hexagonal configuration. This meant that there were a total of 12 cylinders.

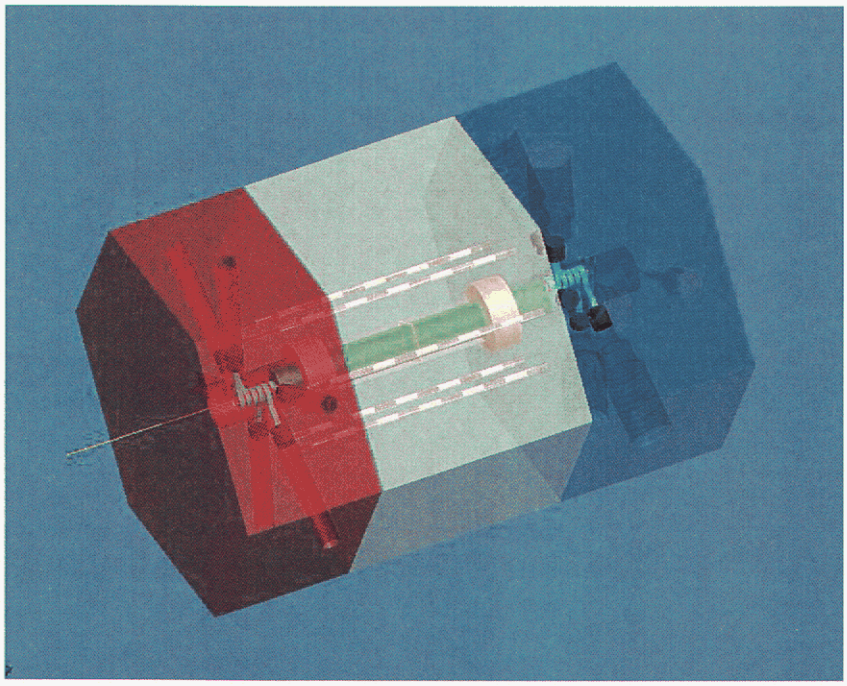

Figure 12: Radial Piston Meso-scale Stirling Engine

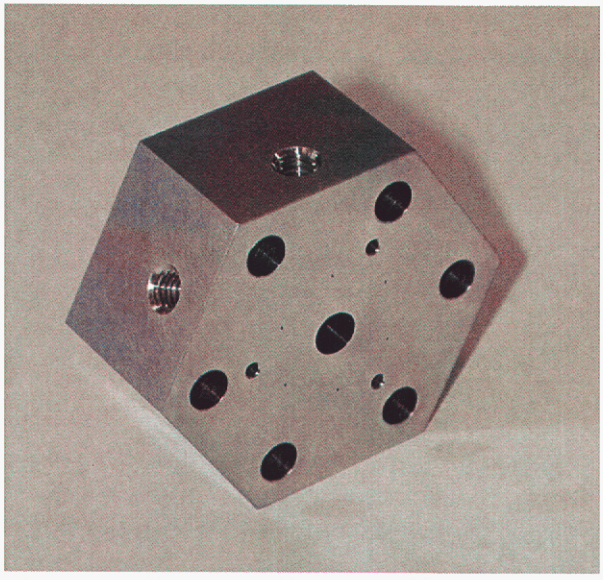

Figure 13: Piston Housing

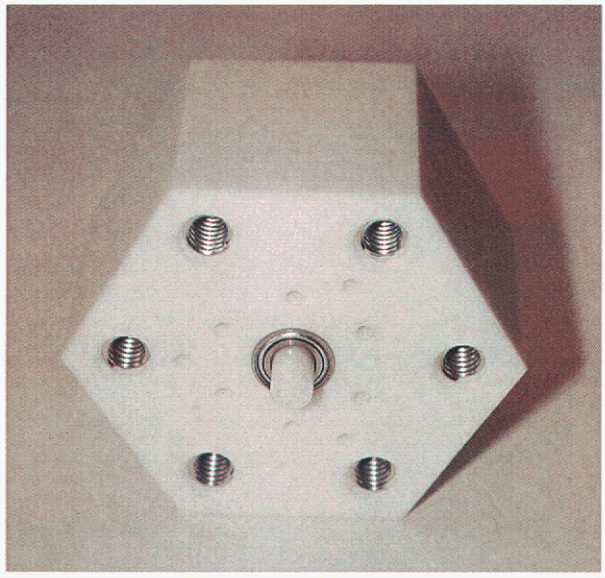

Figure 14: Regenerator Block and Crank Shaft

Since the crank shaft was inside the pressurized volume, there was a constant back pressure on each piston equal to the average pressure inside the cylinder during the cycle. For roughly half of each cycle the pressure in the cylinder was greater than the back pressure and the connecting rod was in compression. For the other half of the cycle, the pressure in the cylinder was less than the back pressure and the connecting rod was in tension. Although this did not change the theoretical work produced during the cycle, there were some practical implications. The pressure differential across the piston was never as great as it would have been with just atmospheric pressure on the back side of the piston. This reduced the peak forces and resulting stresses on the pistons and connecting rods, but it increased the significance of frictional forces, since they constituted a greater fraction of the total force. The reduced pressure differential presumably also resulted in less leakage past the piston seals.

The engine used sapphire jewel bearings to connect the piston rods to the crank shaft. We initially tried to use sapphire pins to connect the rods to the pistons as well, but were unable to install the pins. Instead we used hardened steel pins. Figure 15 shows the pieces of the piston assembly and Figure 16 shows an assembled piston and connecting rod.

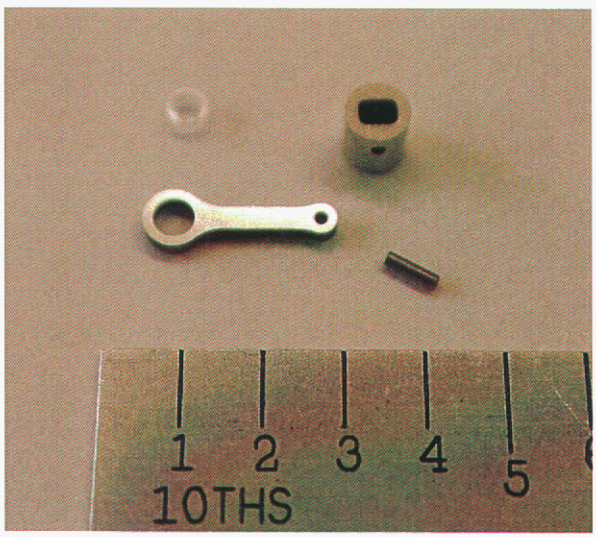

Figure 15: Piston, Rod, Pin, and Jewel Bearing

Figure 16: Assembled Piston and Connecting Rod

The cylinder housings were made from 304 stainless steel. Initially, the pistons were made from non-galling Nitronic 60 stainless steel and the engine was operated without lubrication and without piston rings. Reasonable piston seals were achieved by machining the pistons and cylinders to tight tolerance (0.1 mil or 2.5 micron on the diameter) with line-to-line fit at maximum material condition. During assembly, some of the pistons had to be individually hand-polished so they would slide in the cylinders. This all-steel design was desired for high-temperature operation. In later iterations, we tested two alternative designs to improve the seal and decrease the friction. One design used Torlon pistons as shown in Figure 18. The other design used Nitronic 60 pistons with Torlon rings (Figure 17). Each piston had two split rings with the splits opposite each other. Split rings served two functions. First they were needed for assembly since a solid ring could not be stretched enough to slide over the head of the piston into the groove. Second, with the split, the slightly oversized rings acted as springs to maintain constant contact against the cylinder walls. Figure 19 shows all of the engine components prior to assembly.

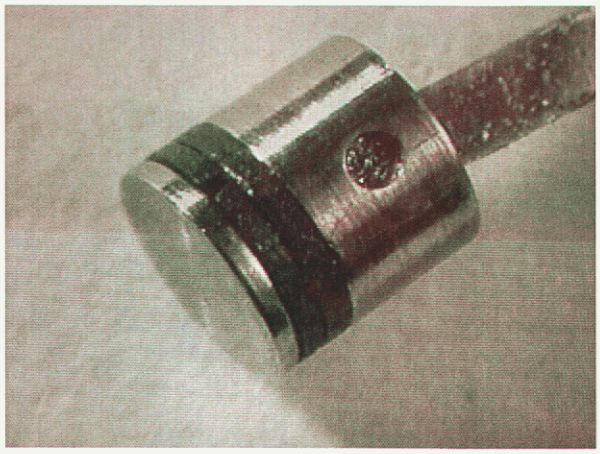

Figure 17: Steel Piston with Torlon Rings

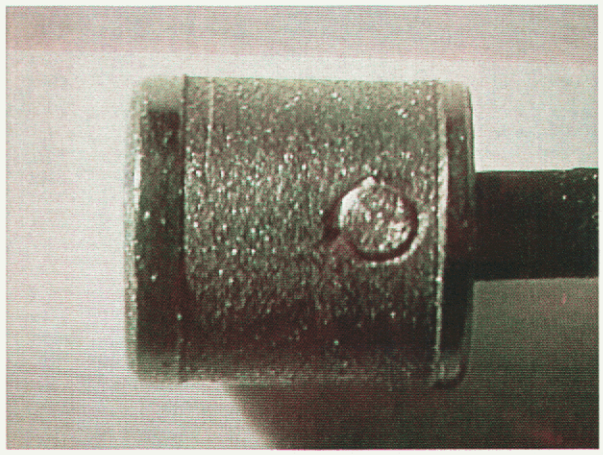

Figure 18: Torlon Piston

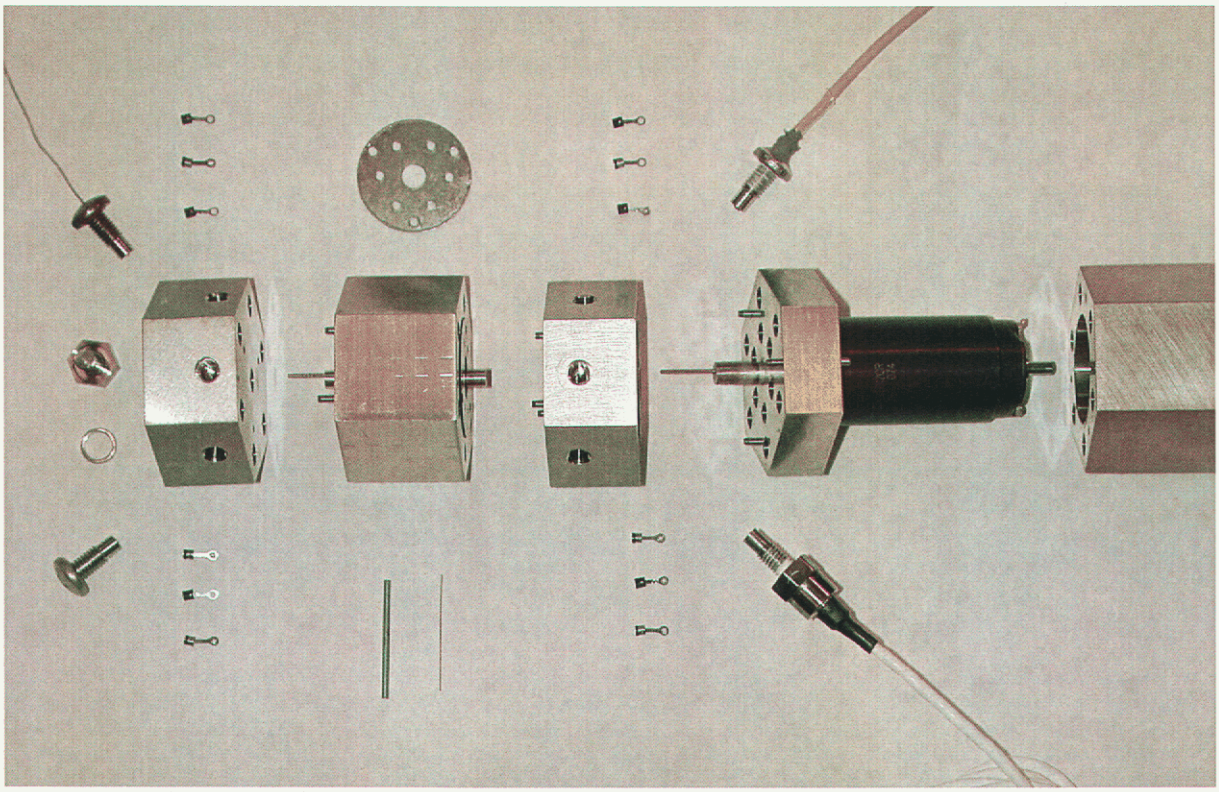

Figure 19: Unassembled Meso-scale Stirling Engine

Test results

For testing we used the electric motor to turn the engine and we recorded the resulting pressures and temperatures in the cylinders. In this mode, the Stirling cycle worked as a heat pump. This allowed us to measure friction, compression, and other engine parameters without supplying a heat source. The test setup is shown in Figure 20. The engine was instrumented with pressure transducers and thermocouples. Average motor voltage and current were also recorded.

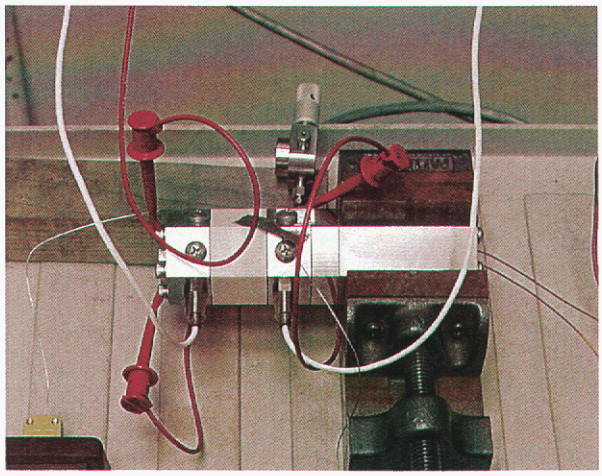

Figure 20: Engine Test Setup

Initially the system was operated at slow speed with the cylinder ends open (no compression) to measure the frictional torque. The combined torque of the engine and motor was about 2 mm-N (0.28 oz-in). The manufacturer specifications listed the frictional torque of the motor alone as 0.14 oz-in, meaning the friction from the engine was comparable to the motor.

The system was then tested at different pressures and engine speeds using air, helium, argon, and carbon dioxide as the working gas. Initial tests showed considerably less compression than was expected. This was apparently due to two factors. One was excessive dead volume in the regenerator and at the ends of the cylinders. Since the swept volume was small, the dead volume from seemingly insignificant features like thread relief or clearance gaps around the transducers was significant. The pressure transducers were modified to decrease the dead volume in the cylinders and the regenerator design was modified, but the problem was not completely eliminated.

The second cause was leakage past the pistons. Figure 21 shows a comparison of the expected pressure curve for the appropriate operating temperatures and the actual measured curve. These data were generated with the system operating at 70 hz with argon. The effect of the dead volume has been accounted for in the calculated pressure so the difference is apparently entirely due to leakage. As described earlier, we tried adding Teflon piston rings to decrease leakage past the pistons. They appeared to provide little benefit, but the tests were inconclusive because other parts of the engine were beginning to deteriorate by the time they were tested.

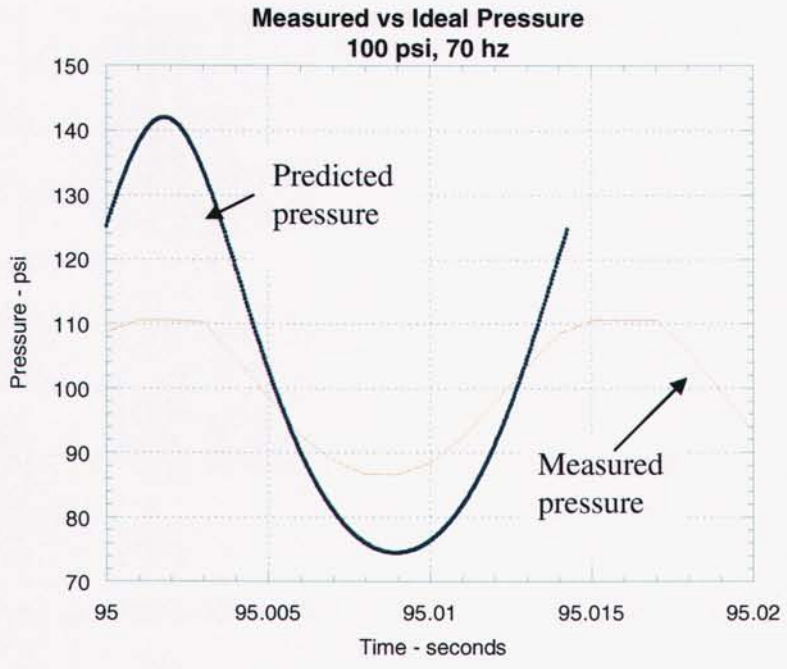

Figure 21: Measured Versus Calculated Pressure Without Leakage

The issue of leakage might not be as bad as it appears from these data because the engine was operated at relatively low frequency on these tests. At higher speeds, there is less leakage on each cycle because there is less time before the pressure differential is reversed and the gas begins to leak the other way. This effect is evident in Figure 22, which shows the increasing pressure swing with increasing engine frequencies. With perfect seals, the pressure would be independent of frequency. The highest frequency in these tests was 70 hz. An engine this size should operate around 2500 hz. We were unable to operate at that speed for several reasons, discussed later, but had we done so, the compression would presumably have been much better.

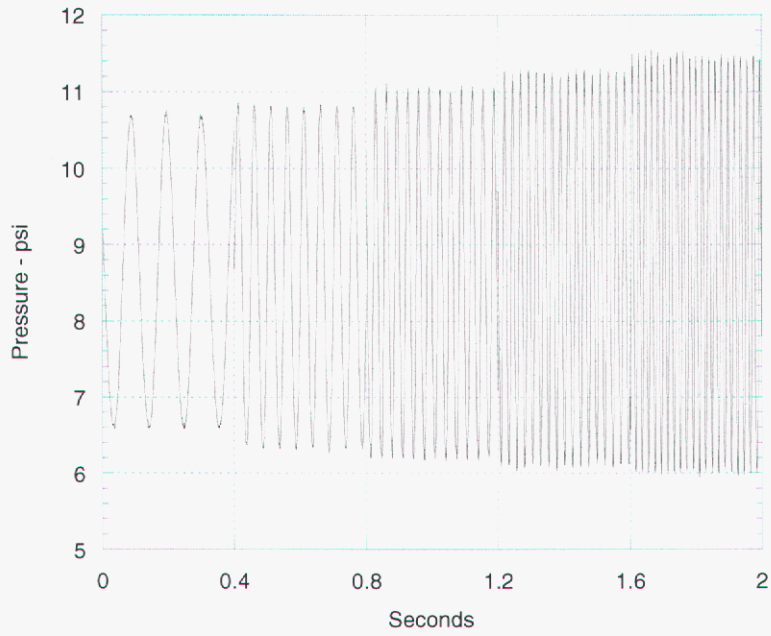

Figure 22: Cylinder Pressure at Different Engine Speeds

Despite these limitations, we were able to observe the expected heat pumping effect. This is shown if Figure 23. The working fluid in this test was argon. At the start of the test, the voltage to the motor was increased in steps from zero to five volts. The voltage controlled the engine speed so this produced a change in engine speed from 0 to about 50 hz. Next, the nominal pressure was increased from 10 to 100 psi in four increments while the engine speed remained constant. This was done by adding gas to the central volume around the crankshaft which then leaked into the individual cylinders. At 100 psi, the voltage was increased again to 7 volts (~70 hz) and then the pressure was increased again to 125 psi. Finally the power was turned off.

With each step in either voltage or pressure, the temperature difference between the hot and cold ends of the engine increased as heat was pumped from the cold end to the hot end. In theory the cold end should have gotten colder, while the hot end got hotter. There was an initial small decrease in temperature at the cold end and a few temporary step decreases later on, but the major effect was at the hot end and, overall, the temperature at the cold end actually increased. This was due to frictional heating. Had there been no heat pumping, both ends of the engine would have heated up. The effect of the heat pumping then was to slow the heating rate of the cold end while accelerating the heating at hot end. This is apparent at the end of the test, when both ends equilibrated at a higher temperature than at the start of the test. It appears that the heating affect was worsening toward the end of the test suggesting that the engine might have been deteriorating. The entire test lasted about 8 minutes.

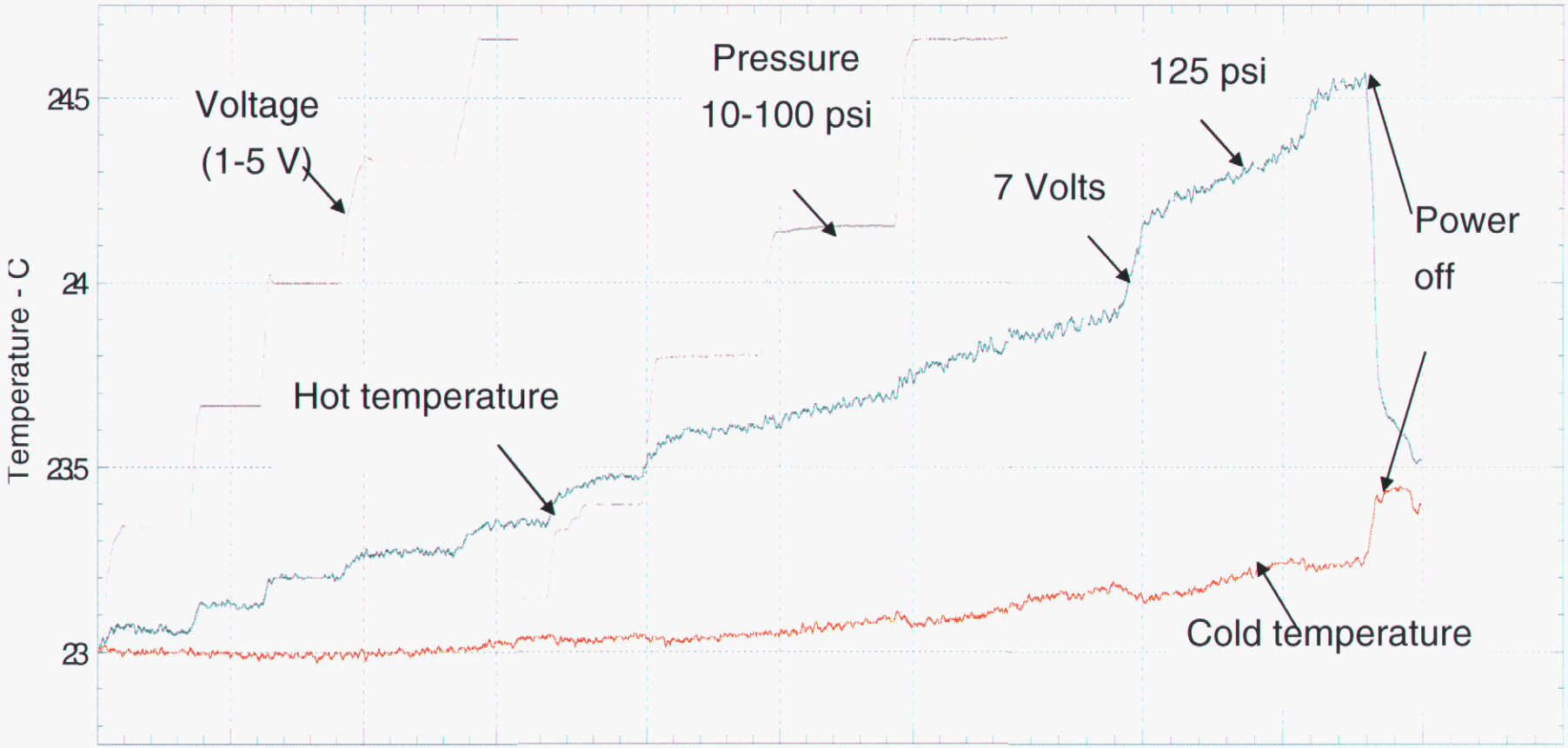

Figure 23: Temperature Difference Due to Heat Pumping

The observed temperature difference on these tests was quite small – only about 1.5 degrees. Although this might appear to be insignificant and indicative of poor performance, it is not. The temperature difference that is generated by a heat pump is only what is needed to supply or dissipate the pumped energy at each end. In this case, the bulk temperature of the metal at both ends was the same and the heat transfer was good so minimal temperature gradients were generated. The real question is how much heat was moved. Since the heat capacity of the structure on this test was large compared to the amount of heat involved it was impossible to measure a bulk temperature change. However, the test data suggest that the heat pumping rate was comparable to the heat generation rate due to friction. From our earlier measurement of frictional torque, we estimate that the frictional heating at 50 hz was about 0.5 watts. Assuming half of this was at each end, the device was pumping about 0.25 watts at 50 hz and 100 psi. Both theory and experiment show that the power scales linearly with both frequency and nominal pressure. This suggests that, had we been able to operate at 1000 psi and 500 hz (still a modest speed) the device should have pumped 25 watts. Unfortunately, the jewel bearings failed rapidly and the device stalled when we attempted to operate at higher power levels so we could not demonstrate this.

Three attempts were made to operate the device as an engine by heating one end and cooling the other end. In these tests, the entire end of the device was heated with a resistance heater. Consequently, far more heat was applied than was needed. Instead we needed to supply a few watts at each cylinder and minimize the heating of the bulk structure. Furthermore, we did not have a good insulator in the regenerator section. Consequently, we were not able to generate the temperature differential that we wanted and the tests were inconclusive. The engine did not turn by itself, but the current draw of the motor decreased. These tests illustrated two fundamental issues that we did not resolve in this project. One is how to maintain a reasonable temperature difference without excessive parasitic heat transfer and the other is how to efficiently dissipate the waste heat to the atmosphere.

Beyond the thermodynamics issues, there were several mechanical design problems with the engine. One concerned bearings. Miniature ball bearings worked well at the cold end of the crank shaft, but could not be used in the hot end. The size of the bearings was marginal and they could not be used if the engine size were reduced any further. Jewel bearings were not suitable for the forces and frequencies that were required and they failed frequently during testing. When they failed, they fractured into small pieces that gouged the piston and cylinder walls and damaged other parts of the engine. Figure 24 shows a piece of a failed jewel bearing.

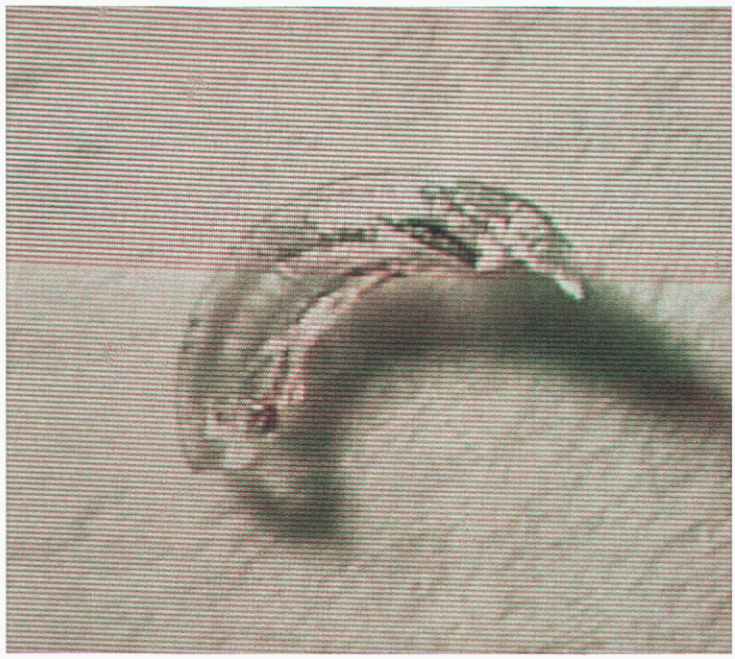

Figure 24: Piece of Failed Jewel Bearing

Although the DC motor we used was adequate for testing the engine, it was larger than the engine and was limited to about 8500 rpm – well below the desired operating frequency. Ultimately a custom designed generator is needed. Preferably the rotor would be integrated into the regenerator to minimize volume.

Materials of construction were also an issue. Initially we limited the design to materials suitable for temperatures as high as 800°C. This basically limited the choices to metals and ceramics. For static seals between segments of the engine, we used Grafoil sheets. However, even with high-temperature materials, it is questionable whether the higher temperatures can be achieved without also overheating the cold end. Later we chose to limit the device to about 400 °C and accept a lower efficiency to allow a greater choice of materials including Teflon and PEEK.

Rotary Engine

As mentioned earlier, a goal of the second engine design was to fabricate the components using through-mold electroforming in micromolds. This is a versatile way to produce high aspect ratio prismatic microparts from metals. Molds can be produced by either SU8 or LIGA. SU8 technology utilizes a commercially available thick UV photoresist [ref. 7] and thus only clean room facilities and a UV lithography source are needed. LIGA, an acronym from the German words for Lithography, Electroforming, and Molding, produces high aspect ratio prismatic micromolds by irradiating Polymethylmethacrylate (PMMA) with synchrotron generated x-rays. Both techniques produce microparts that must subsequently be hand-assembled into systems [ref. 8].

Both electroforming techniques start by lithographically exposing the resist (Figure 25). Then, the exposed photoresist is developed in either a PGMEA (Propylene glycol methyl ether acetate) based developer for SU8 or a GG developer (2-butoxyethoxy-ethanol, morpholine, 2-aminoethanol, and water) for LIGA PMMA. Nickel is electroformed in the developed mold and then released. Electroformed nickel is ideal for microengine applications because of its high strength and ductility [ref. 9].

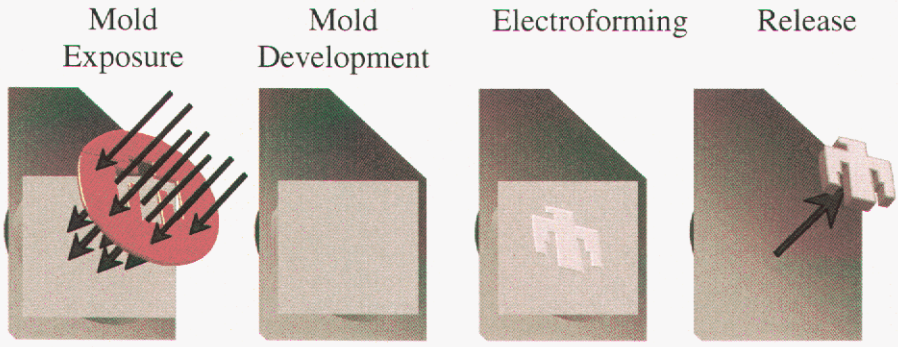

Figure 25: Fabrication steps for through-mold electroforming.

Despite the utility of these techniques, they are limited to prismatic geometries. For this reason we selected a rotary engine design for our second engine. Conceptually, the rotary micro-Stirling engine operated much like the piston version except that the pistons were replaced with two rotary mechanisms. Each mechanism used the same geometry as a Wankel engine with an epitrochoidal housing and a triangular rotor as shown in Figure 26. The two rotors, one at the hot end and one at the cold end, were physically attached to the ends of the regenerator housing so that the regenerator rotated with the rotors. The regenerator housing included three capillaries for the gas to move continuously back and forth between the hot and cold ends. Each volume in the hot epitrochoid was mated with the lagging volume in the cold epitrochoid.

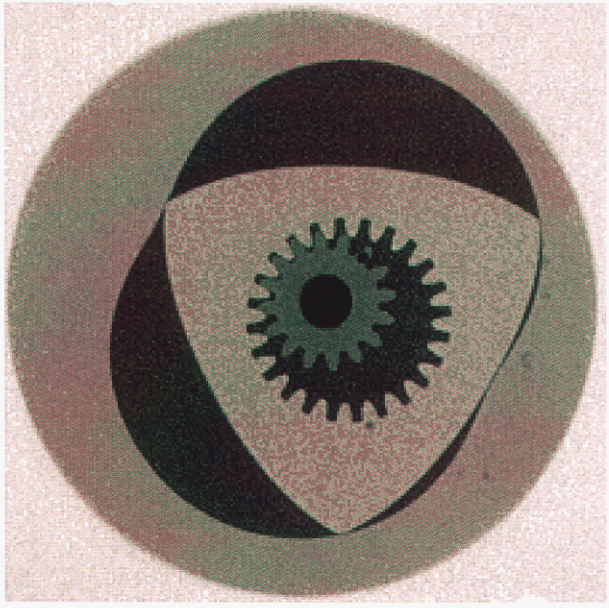

Figure 26: Epitrochoidal Housing, Rotor, and Gear for Rotary Engine

Some advantages of a rotary Stirling engine are that the planar geometry enhances heat transfer to the working gases, the rotary motion can be easily coupled to an electrical generator, and the motion is inherently smooth, eliminating the need for a flywheel. A disadvantage is that the volume between the epitrochoid and the rotor is never zero. This inherent dead volume decreases the engine performance as described earlier.

Figure 27 shows the design of the first generation of the rotary micro Stirling engine. Later versions were conceptually the same, but had small changes to simplify the fabrication and assembly. The components included the epitrochoidal housings, the rotors, the stationary gears, the gear plates that held the stationary gears, the top plate, the regenerator, the eccentric shaft, and an outer sleeve. LIGA was used to fabricate all of these parts except the regenerator, the eccentric shaft, and the sleeve. As with the piston engine, the design included a commercial DC motor/generator.

The design used miniature ball bearings at the cold end and jewel bearings at the hot end. Locating pins held the parts in the proper alignment. As with the piston design, the engine relied on a tight fit between the components to provide sufficient sealing. The LIGA process can maintain tight feature tolerances but has greater variation on part thickness. For the concept to succeed, the housing and rotor had to be the same thickness. This was accomplished by fabricating the housing and rotor on the same wafer.

Three iterations of the rotary engine were fabricated, but none was assembled into a complete engine.

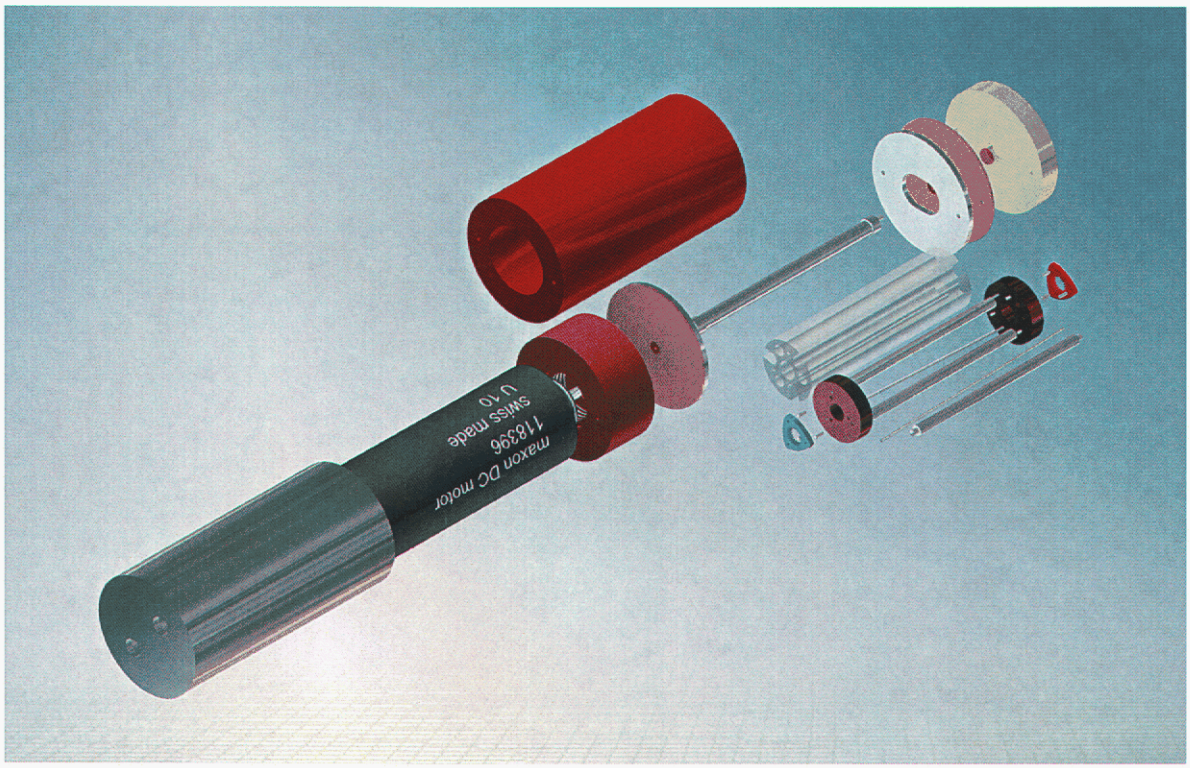

Figure 27: Rotary Micro Stirling Engine

SU8 Based Fabrication

Two different iterations of micro-Stirling engine designs were electroformed in molds created by patterning a Sandia thick SU8 formulation with a broadband UV aligner [refs. 7 and 10]. For each set of molds, a 1.2 mm thick Si wafer was first metallized with 750 angstroms of Ti followed by 4000 angstroms of copper. A 450 micron total thickness SU8 coat was applied to the wafer in two spin coats. For the first spin coat, approximately four milliliters of SU8 were poured onto the center of the metallized wafer, spun at 640 rpm for 15 sec, and baked on a hot plate at 95°C for 25 min. For the second spin coat, approximately four milliliters of SU8 were poured onto the center of the metallized wafer, spun at 640 rpm for 15 sec, and baked on a hot plate at 95°C for 35 min. The edge bead was then removed by squirting acetone on the edge of the wafer while spinning the wafer at 600 rpm. To relieve internal stresses in the SU8 coat, a post apply bake was carried out by heating the wafer on a hot plate from room temperature to 95°C at a rate of 45°C/hr, holding at temperature for 4 hours, and then cooling back down to room temperature at a rate of 60°C/hr.

The wafer was then exposed with a Karl Suss MA6 broadband UV aligner under soft contact to a total dose of 8.096 J/cm2 measured at 365 nm. A post exposure bake was carried out by heating on a hot plate from room temperature to 85°C at 60°C/hr, holding at temperature for 1 hour, and then cooling back down to room temperature at a rate of 60°C/hr. The wafer was then immersion developed in a puddle of PGMEA based SU8 developer (MicroChem, Newton, MA, USA) for about 1 hour and 40 minutes.

A copper layer was deposited into the molds from a copper sulfate bath at 15 mA/cm2 for twenty minutes. This layer acts as both a plating base and as a release layer for the final removal of the plated microparts. The molds were then placed in a nickel-Watts electroplating bath with saccharin as a stress reliever [ref. 11] and 200 microns of nickel were electroformed at 15 mA/cm2. After plating, the bulk of the SU8 was fractured off the wafer by thermally cycling the wafer repeatedly from room temperature to 77K in a LN2 bath. The microparts were then released by etching away the underlying copper in an etch consisting of one part vol DI water, one part vol aqueous ammonium hydroxide, and one part vol 3% aqueous hydrogen peroxide. The large plugs of SU8 in the crevices of larger parts were removed by heating at 80 °C in saturated aqueous KOH. The smaller plugs of SU8 were manually extracted with fine point tweezers.

Once cleaned, microengine parts electroformed in SU8 molds had sidewall surface roughnesses of the order of 1 micron rms or better (Figure 28). The cleaning step proved to be crucial in obtaining electroformed parts that could be assembled without interference between debris and surface. After evaluating several solvent systems for use as SU8 debris cleaners the following cleaning protocol was adopted:

1. Soak parts in MagnaStrip (commercial remover)
2. Sonicate 20 minutes
3. Wash in acetone
4. Sonicate in acetone for 2 minutes
5. Wash in acetone
6. Dry with N2 gun.

This cleaning protocol removes virtually all SU8 debris (Figure 29).

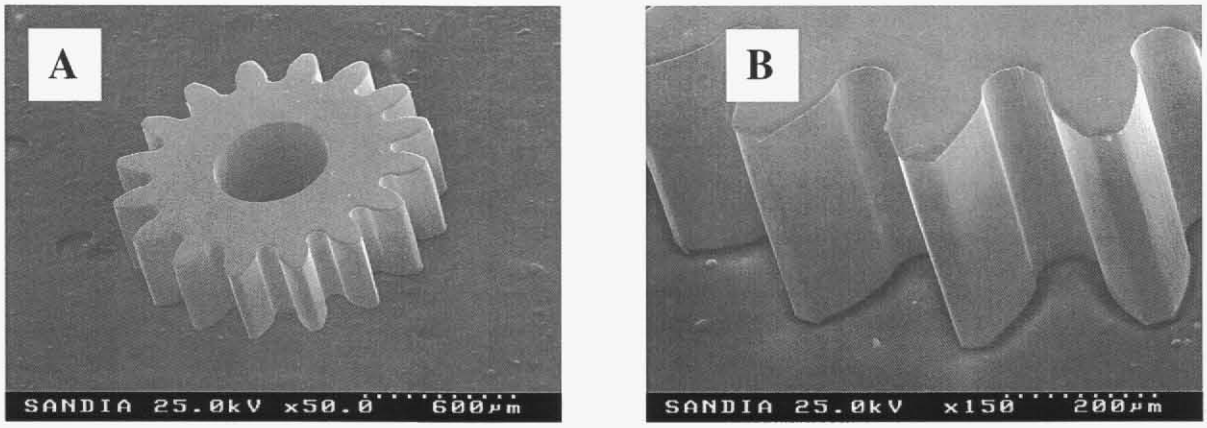

Figure 28: (a) Low and (b) medium magnification micrographs of cleaned microengine parts electroformed in SU8 molds.

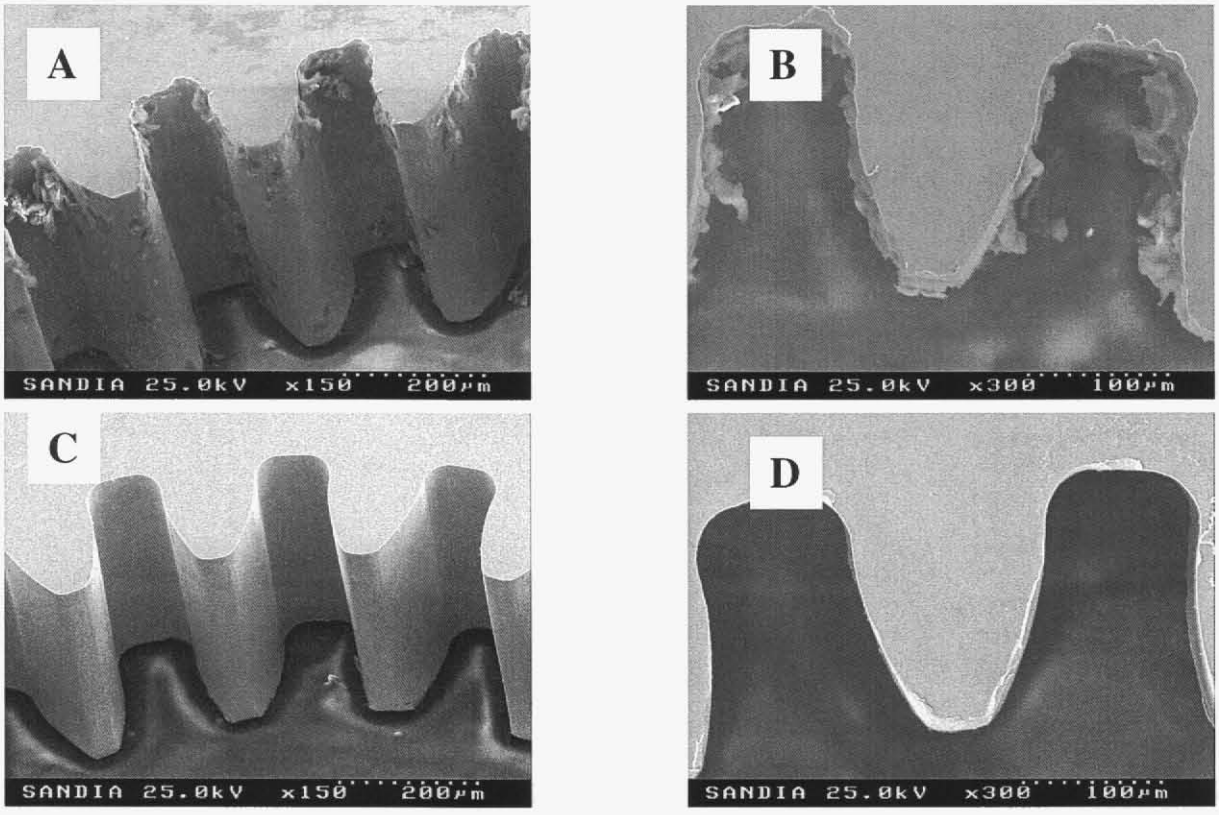

Figure 29: (a) Oblique and (b) top views of as released microengine parts electroformed in SU8 molds. (c) Oblique and (d) top views of microengine parts after cleaning.

As metrology of the electroformed parts was carried out, cross-sectional microphotographs of microengine parts showed a sidewall runout of the order of one or two microns for every 400 microns in height.

After the first microengine design was fabricated using SU8 molds, the parts were redesigned with: a slightly different contour; etch vias to facilitate the release of the electroformed parts; and with holes to introduce press-fit pins to stack parts and thus create thicker parts.

LIGA Based Fabrication

After successfully electroforming the second microengine design in SU8 molds, LIGA microengine molds were created for the same design. A gold mask of the desired mold pattern was creating by plating 30 microns of gold in photoresist patterned on a 100 micron thick silicon wafer. A LIGA PMMA substrate was prepared by solvent bonding a precut 600 micron thick PMMA disk to a metallized, 650 micron thick silicon wafer.

The substrate was exposed at the Advanced Light Source (ALS) Beam Line 3.3.2 at Lawrence Berkeley National Laboratory. The exposure conditions (filter set and exposure time) resulted in a top PMMA dose of 4.58 kJ/cm3 and a bottom dose of 3.15 kJ/cm3. The exposed PMMA was developed at 21 °C in GG developer for a period of 31 hours. After development, the molds were placed in a nickel watts electroplating bath and the LIGA microparts were overplated. The excess nickel was removed by lapping and polishing down to a thickness of 500 microns; the PMMA was dissolved in acetone; and the polished parts were released by etching the electroforming seed layer in an aqueous ammonium hydroxide/hydrogen peroxide etch.

Since LIGA uses PMMA as the x-ray sensitive photoresist and PMMA is soluble in a variety of solvents, LIGA microengine parts were devoid of any photoresist debris after cleaning in acetone (Figure 30). The sidewall surface roughnesses of the LIGA microengine parts was of the order of 1micron rms or better.

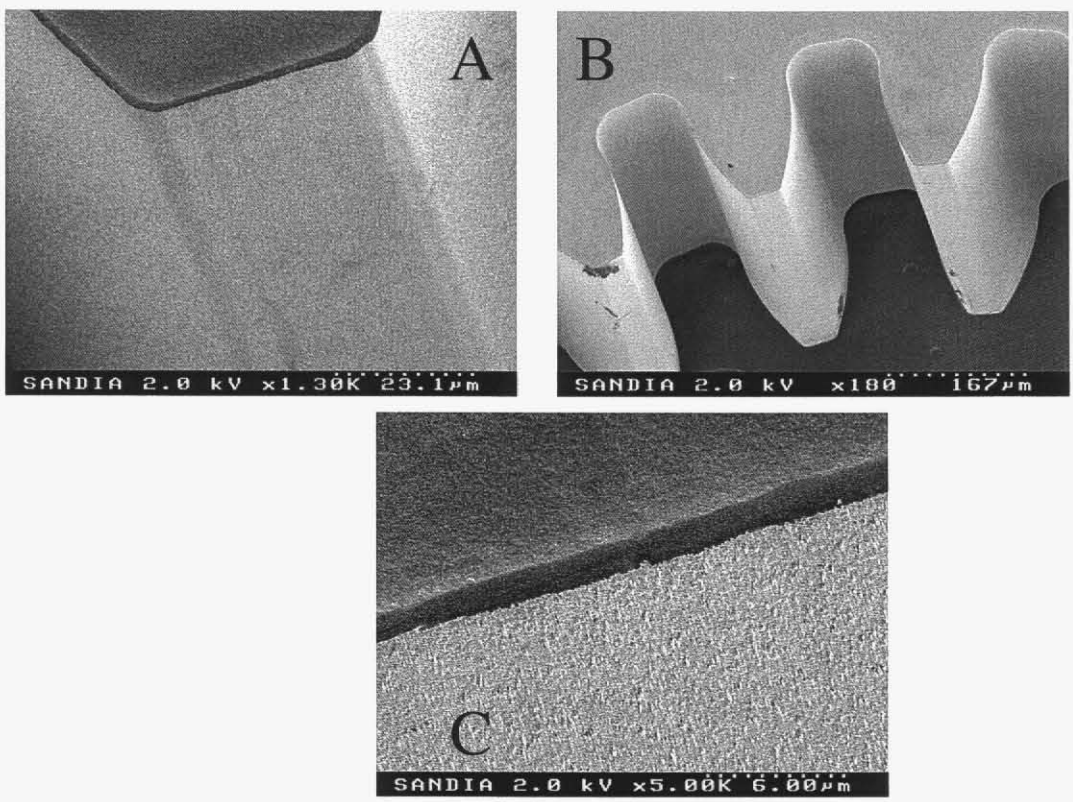

Figure 30: (a) Low, (b) medium, and (c) high magnification micrographs of LIGA microengine parts immediately after an acetone clean.

Final Assembly

The initial set of SU8 parts were partially assembled as shown in Figure 31. This assembly included the housing, rotor, stationary gear, and gear plate for one end of the engine. The assembly was used to study how the parts fit and moved together. From this assembly, it became evident that a new method was needed to carry out metrology of an assembled unit. Thus, an x-ray based inspection procedure was devised.

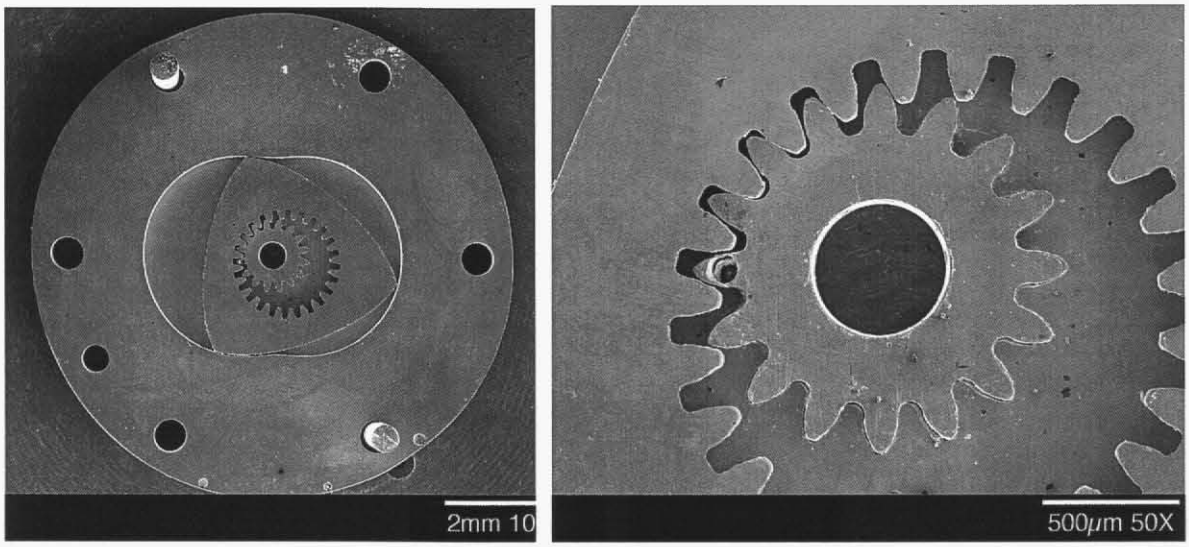

Figure 31: Partially Assemble Engine from SU8-fabricated parts

In this novel procedure, an x-radiograph of the assembled Stirling engine was taken using a Faxitron Model 43855B Dual Cabinet (which has a 0.5 mm source size), bare single R (SR) Kodak film, a 54" film-to-source distance, and an 80 kV x-ray beam at 36 mAmin (Figure 32). Flaws are seen in a tooth in the central gear, near a tooth on the rotor, and in a few spots in the body of the device, but the overall structure of the engine is well formed. In order to measure the gaps between the rotor and the body, another radiograph was taken at 60 kV and 15 mAmin. This produced a lighter image of higher contrast, effectively collapsing the 3 dimensional parts into a plane, which facilitates the use of conventional optical metrology tools that are inapplicable to 3D assemblies. Using a View Engineering Voyager V6X12 microscope [ref. 12] in transmission mode on this latter film, a number of measurements were made on the edge of the stator and the body and saved as two series of x,y coordinates, or point clouds, for each part. By fitting these point clouds to a function, it was possible to determine the size of the gap where the parts came closest (Figure 33). It was possible to move the rotor and repeat this process in any position. An average gap of 10.2 microns was measured.

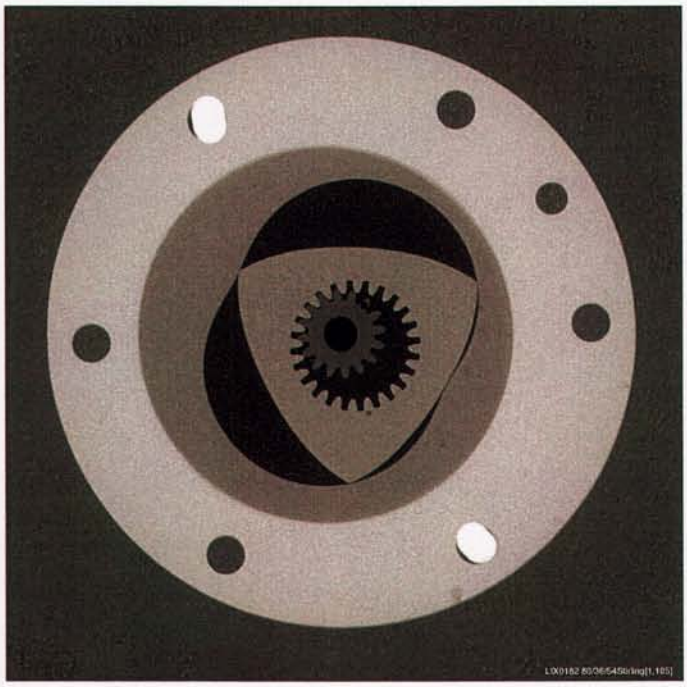

Figure 32: X-ray radiograph of assembled engine.

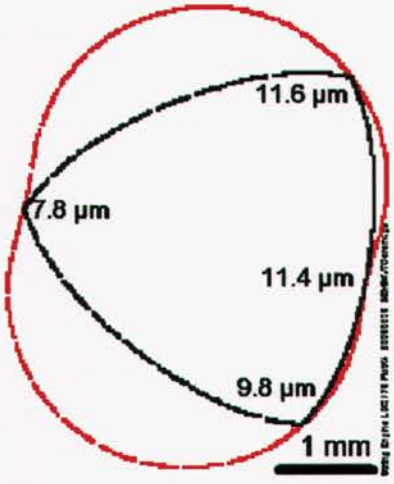

Figure 33: Point cloud collected from radiograph and the measured gaps.

The parts fit together well and moved freely. However, we did not assemble the entire engine because we had determined the need for various changes in the design.

The LIGA parts were also hand assembled and examined for fit and motion. Microscopic examination showed that gaps between components were 10 microns or less. The eccentric shaft proved to be difficult to fabricate and was not completed by the end of the program. Consequently, the complete engine was not fabricated and tested. Figure 34 shows different views of the partially assembled engine. Figure 35 shows a micrograph of the gap between the rotor and the housing.

Figure 34: Optical photographs of partially assembled LIGA engine.

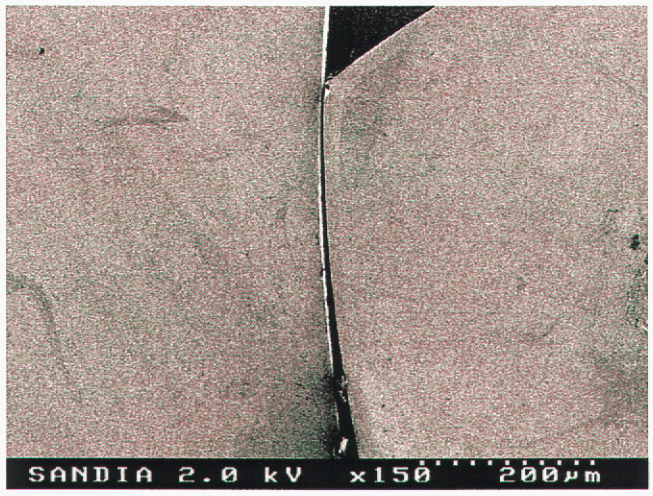

Figure 35: Micrograph showing a gap between parts of the order of 10 microns.

Conclusions for engine

The Stirling cycle has many advantages for a microengine. We have demonstrated a piston micro-Stirling engine as a heat pump, although higher pressure and frequency is needed for efficient operation. We have also demonstrated the fabrication of components for a rotary micro Stirling engine using through-mold electrodeposition in SU8 and LIGA molds. The prototyped nickel parts are hundreds of microns in thickness and have the dimensional tolerances required by the Stirling engine cycle.

This page intentionally left blank.

NUMERICAL SIMULATION OF MICROCOMBUSTION

This section reports simulation results of operating conditions for micro-combustors and potential implications to the integration of these combustors in a micro-Stirling engine. In addition to the description of the basic tools used for the simulation of surface, gas phase chemistries and heat management mechanism, the report contains recommendations for initial designs of excess-enthalpy micro-scale combustors. The integration of the micro-combustor with the micro-Stirling engine requires the choice of optimum heat management resulting from combustion-related heat release. Issues of heat management and integration with the micro-scale Stirling engine are pursued using CFD simulations.

We found that by choice of the operating conditions and channel dimensions energy conversion occurs by catalysis-dominated or catalysis-then-homogeneous phase combustion. The main parameters controlling the rate of combustion are the dimensions of the combustor, the flow rates imposed, and the mixture equivalence ratios. For Platinum alloys that can sustain temperature above 1000 K, transitions to homogeneous chemistry is achieved at relatively fuel-lean conditions (equivalence ratios of the order of 0.3 for hydrogen-air mixtures).

We have developed a suite of simulation tools both in support of the design of the prototype combustors, and to investigate more fundamental aspects of combustion at small scales. The computational tools that were developed include:

3D-CFD using Detailed Chemistry

We used a commercial code, CFDRC's CFD-ACE [ref. 13], that can handle complex geometries. This is a finite volume code in which various complexities of surface and homogeneous chemistry and transport models may be implemented. Structure designs were established with CFD-GEOM in a 2D and 3D geometry with variations in diameters. We have used the Chemkin library (which is used in CFD-ACE) to specify the chemistries and transport properties of gas-phase species. The steady state operation of an excess-enthalpy micro-combustor was modeled using CFDRC's CFD-ACEU solver. The mesh was constructed using CFD-GEOM (another product of CFD-ACE) and parameterized to allow for quick refinement or redesign of the combustor. The discussion below illustrates the model assumptions, highlights the basic trends of the final combustor temperature as a function of the more pertinent design parameters, and provides recommendations for 3 different operating conditions based on 3 different combustor geometries. Two of these geometries are based on experimental dimensions based on using a tube-in-a-tube geometry in this project.

Direct Numerical Simulation Capability for Catalytic-Channel Flows

We developed two high-fidelity simulation codes capable of investigating fundamental combustion issues associated with micro-combustion. While commercial CFD codes like CFD-ACE allow for steady-state engineering simulations of microcombustors, unsteady codes for treating microcombustion with coupled detailed gas-phase and surface chemical kinetics do not presently exist. What follows is a brief description of two new simulation capabilities, and a demonstration of one of these new codes to study the underlying combustion phenomenon in a configuration qualitatively similar to the experiment.

The first new code solves the low-Mach number reduced form of the conservation equations of mass, momentum, energy, and species in the cylindrical coordinate system. The simulation code employed is based upon the spectral element method and a stiffly-stable time splitting scheme that couples the "thermo-chemistry" and the "hydrodynamic" subsystems which, respectively, are comprised of the conservation equations of energy and mass of all species; and the conservation equations of mass and momentum [ref. 14,15,16,17,18,19]. The thermo-chemistry component is integrated fully implicitly without any further time or operator splitting while the "hydrodynamic" subsystem utilized a second order mixed explicit-implicit scheme. An interface to CHEMKIN III [ref. 20] gas-phase and surface-chemistry is incorporated in the code, enabling detailed gas-phase and surface reactions to be fully coupled with the hydrodynamics and with each other in the code.

The second new code solves the compressible form of the reactive Navier-Stokes conservation equations for mass, momentum, energy, and species in a Cartesian coordinate system. The simulation code is an extension of a parallel high-order finite difference direct simulation code, S3D [ref. 21]. Reactive adiabatic and isothermal wall boundary conditions were developed and implemented in S3D, and the chemistry source terms are integrated implicitly. Like the spectral element code, an interface to CHEMKIN III [ref. 20] gas-phase and surface-chemistry is incorporated in the code, enabling detailed gas-phase and surface reactions to be fully coupled with the hydrodynamics and with each other in S3D. This code was tested with detailed hydrogen-air gas phase chemistry and a skeletal mechanism for Platinum surface reactions in an adiabatic channel. The results give qualitative agreement with the spectral element code in terms of transient light-off distance in the channel.

Direct numerical simulation of transient light-off of a catalystic microcombustor

To perform a feasibility study using the spectral element code we considered a simplified system which consists of a straight tube with its inner surface being catalytic (platinum). "Parabolic" velocity profiles were assumed on the inflow boundary; the no-slip boundary condition was applied on the wall; and on the catalytic surface of the tube, the balances of the flux of species and energy were enforced. Furthermore, we assumed that there was no heat loss from the reactor tube to the ambient. The zero-Neumann boundary condition was implemented in its weak form on the outflow boundary for all dependent variables. With the reactor being 0.2 cm in diameter and 2.0 cm in length, the numerical results indicated that for the particular mixture used in the simulation, a premixed flame cannot propagate or exist within this tube in the absence of surface reactions. To ignite the mixture in the presence of a catalytic active surface, a hot spot was applied near the entrance of the numerical domain.

Detailed hydrogen-air gas-phase chemical kinetics [ref. 22] and realistic transport [ref. 23] were utilized in the simulations. In particular, the chemical kinetic scheme consists of nine species (H_2, N_2, O_2, O, H, OH, H_2O, H_2O_2, HO_2) and twenty reversible reactions. The catalytic surface was modeled by the reaction H2 -> 2H, since the capability of simulating a detailed surface reaction scheme is currently being implemented and tested. We will be performing simulations with more complex methane-air kinetics as used in the experiment.

Following an initial transient associated with ignition delay, the numerical results reveal that, in the presence of catalytic reactions, a stable reaction zone can be realized and its structure is qualitatively similar to experimental observations. Figure 1 shows the computed species mass fraction isocontours as well as that of temperature of the reaction zone. It is evident that gas-phase combustion is anchored on the catalytic wall near the entrance of the reactor and that it extends about two diameters in length downstream. The reaction zone is tightly coupled with the wall reactions and is much broader in extent than a laminar premixed flame. In fact, combustion is shown to occur in a distributed reaction zone. Diffusion in the radial direction, at a distance of about five diameters downstream, homogenizes the scalars in the radial direction. The heat release also accelerates the flow and the axial component of velocity depicted in the Figure 1 which clearly shows the flow divergence (acceleration) driven by chemical heat release. In the present simulation, H_2 is the deficient reactant and is completely consumed in the reactor.

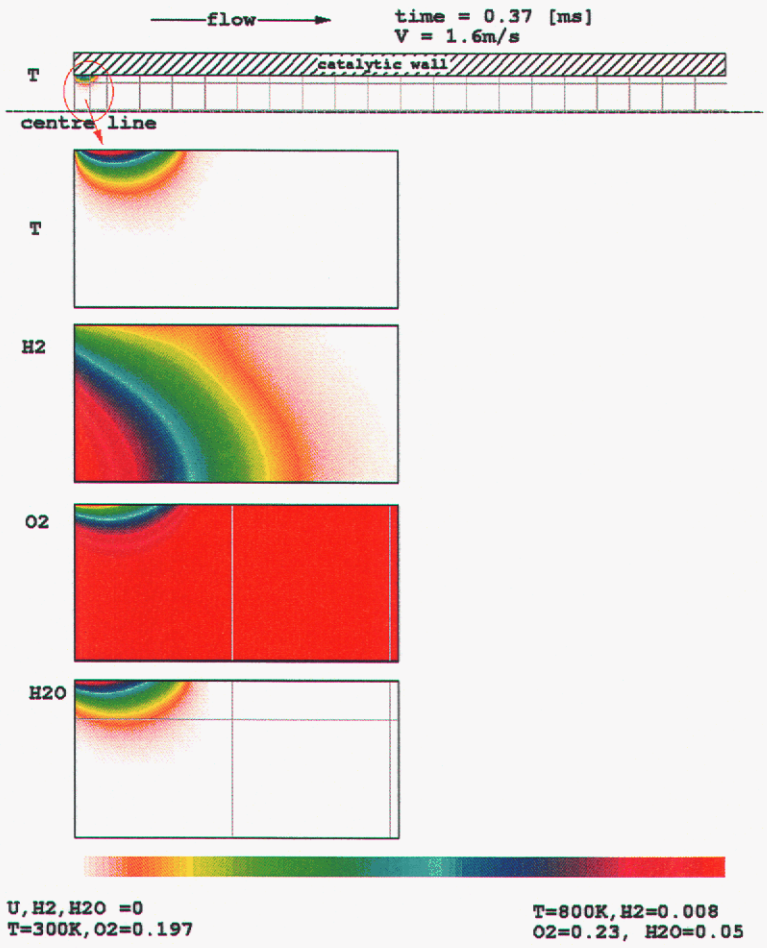

Figure 1: Ignition light-off in a hydrogen/air Pt catalytic micro-combustor channel.

CFD-ACE Engineering computations in support of prototype combustor design

Model Implementation

Kasemo modeled catalytic chemistry mechanism was used for Pt-Hydrogen heterogeneous chemistry and Warnatz's gas phase mechanism for hydrogen-air chemistry. The combined mechanisms are found to yield optimum convergence of the CFD-ACE solver and have been determined by Appel *et al.* [ref. 24] to yield reasonable comparisons with experiments. All components of the structure assumed a preheated temperature of 340 K. The outer walls of the channels are assumed to be adiabatic, although the adiabatic conditions may be easily modified to represent heat transfer to the regenerator of the Stirling engine.

Run Conditions

Three different combustor dimensions are described in this report. They correspond to varying both the inner and outer diameters of the tubes as well as variations in the length of the channel. The simulations presented here are based on hydrogen-air mixtures in which the equivalence ratio is varied according to the following form: $[\phi\ H_2 + 0.5(O_2 + 216N_2)]$. We have also implemented methane-hydrogen-air runs, which are not shown here for purposes of brevity. When appropriate, results for the methane-hydrogen-air simulations are contrasted with those of hydrogen-air alone. Table 1 summarizes the three dimensions considered. The channel length indicated in the table corresponds to twice the width of the combustor. The inlet mixture is preheated to 340 K in all cases considered.

Table 1. Summary of combustor dimensions considered.

Cases	Small Tube I.D. (mm)	Small Tube O.D. (mm)	Large Tube I.D. (mm)	Combined Channel Length (cm)
A	1.0	6	12	4
B	0.5	0.787	1.787	4
C	0.5	0.787	1.787	2

Within these three cases (A through C), different simulations were implemented in which the mixture equivalence ratio and the inlet velocity were varied. Tables 2 and 3 summarize the various simulations under the first two cases, figures 2-4 take a more in-depth look at simulations conducted under case C. Also shown are the maximum temperatures achieved in the different simulations. Case A has been modeled in a 3D geometry. The simulations show negligible differences when examining all aspects of chemistry and thermal conditions to the results found for the 2D cases used for this report. The highlighted conditions (in yellow) correspond to operating conditions that were selected for further discussion at the different combustor dimensions. Results from these operating conditions are discussed in detail later in this section.

Effect of Equivalence Ratio

Table 3 shows that increasing the equivalence ratio also increases the final temperature, this same trend can be seen by the data presented in Tables 1 and 2. At relatively low equivalence ratios (e.g. at $\phi = 0.24$ or lower), homogeneous chemistry remains insignificant, and most of the heat release is accounted for by heterogeneous chemistry. At lower ratios the temperature will also decrease with increasing fluid flow due to a decrease in residence time with the catalytic surface.

Table 2. Inlet conditions and maximum temperature (K) for Case A.

		Equivalence Ratio, ϕ			
		0.18	0.20	0.24	0.28
Velocity (m/s)	0.05	534	607		
	0.10	534	608	766	**1180**
	0.20	534	608	770	1194
	0.30	534	608	762	1184

Table 3. Inlet conditions and maximum temperature (K) for Case B.

		Equivalence Ratio, ϕ			
		0.18	0.24	0.28	0.31
Velocity (m/s)	0.9				
	0.7		756	**1187**	1252
	0.5		757	1183	1250
	0.3	534			

Effect of Inlet Velocity

It is generally understood that increasing the inlet velocity for a given length of a channel reduces the residence time for complete combustion; however, the present results show that increasing the inlet velocity still results in enhancements of the final temperature over a range of equivalence ratios where homogeneous chemistry is present. This is due to a large extent to the reduced dimension of the channels, such that diffusion of reactants to the surface is enhanced, resulting in the rate of transport of fresh reactants in the channel being the limiting rate. Therefore, the present simulations show that the final temperature in the channel may be increased by increasing the inlet velocity by a ten to one ratio over the region detailed. It is important to note that Case A provides the main exception to the overall trends observed for small channels. Here, increasing the velocity from 0.2 to 0.3 m/s resulted in a reduction in the temperature, again emphasizing the important balance between axial and streamwise transport processes at the micro-scale.

The inlet velocity also plays a critical role in channel length over which the specific combustion reactions occur. Looking at one of the more critical reaction steps (step 10 in the Warnatz's gas phase mechanism) we see that the channel length over which this reaction occurs will increase with increasing velocity. The distance at which the maximum rate of change for this reaction occurs will also propagate further down the channel with increasing velocity at a reasonably constant rate with change in the equivalence ratio.

Effect of Preheat Temperature

Although not shown here, the preheat temperature plays a key role in determining the distance at which significant changes in heterogeneous and homogeneous chemistries occur. This distance is strongly influenced by the choice of the fuel and the equivalence ratio. Overall, we found that under the same flow conditions, methane-hydrogen-air mixtures result in longer residence times. Due to the conductivity of the inner tube the maximum temperature of the system is attained very near the end of the buffer. By preheating the fuel the backward heat flux through the fluid is decreased into regions that my not be as structurally stable.

Discussion of the General Structure of the Combustion Process at Selected Conditions

The general structure relating to thermo-chemical scalars at three simulations from the three cases considered is discussed. This discussion illustrates some of the pertinent physics involved in homogeneous and heterogeneous chemistry in the micro-channel. These cases are highlighted in yellow in Tables 2-4.

Case A

Case A corresponds to the large dimension channel at an inlet velocity of 0.1 m/s and an equivalence ratio (Φ) of 0.28. The simulation produced a temperature gradient with most of the heat increase occurring near the inlet (Fig. 2). The maximum temperature produced under these operating conditions is 1180 K. The bulk of H_2 consumption occurs within a distance of 1 to 2 mm from the inlet (Fig. 3). This consumption is correlated with the H_2O formation as shown in Fig. 4. There is no complete conversion of H_2 into H_2O, as suspected, because of the relatively low temperatures in the channel. Beyond the short distance where the bulk of the fuel is converted to products, the concentrations of all major species in the channel remain unchanged. To a large extent, this may be attributed to the saturation of the platinum surface site itself by O

atom site species (with a maximum mass fraction of 0.82 sustained after the short distance) as shown in Fig. 5. The conversion of O through chain branching reactions is very slow at relatively low temperatures. Therefore, the lean conditions tend to saturate the platinum surface quickly and reduce the level of surface chemistry necessary for a complete combustion. Figures 6 and 7 show the interaction of the species H and OH at the catalytic surface respectively. This data echoes the results found by Appel et al. (2002) in their validation of reaction schemes concerning hydrogen-air mixtures over platinum.

Case B

Case B corresponds to the same length channel as Case A, but with reduced channel diameters as summarized in Table 1. It corresponds to an inlet velocity of 0.7 m/s and an equivalency ratio of 0.28. The simulation produced a longer temperature gradient than Case A however most of the heat increase still occurred near the inlet due to the high conductivity of the platinum solid (Fig 8). The maximum temperature in the channel is 1187 K. Figure 9 shows the evolution of the reaction rate corresponding to the reaction, $HO_2 + H \Leftrightarrow OH + OH$. This reaction is associated with the onset of ignition in hydrogen-air mixtures. Therefore, its increase downstream of the catalysis-dominated region indicates a transition to homogeneous chemistry. Significant reduction in H_2 occurs within the first 1 to 2 mm in the channel (Fig. 10). Again, this is correlated with the formation of H_2O as shown in Fig. 11. The problem of surface reaction saturation is still evident, as shown by profiles of the site species, O (which is also maintained at a mass fraction of 0.82) as shown in Fig. 12. Figures 13 and 14 show the interaction of the species H and OH at the catalytic surface, respectively, with far lower values of mass fraction present.

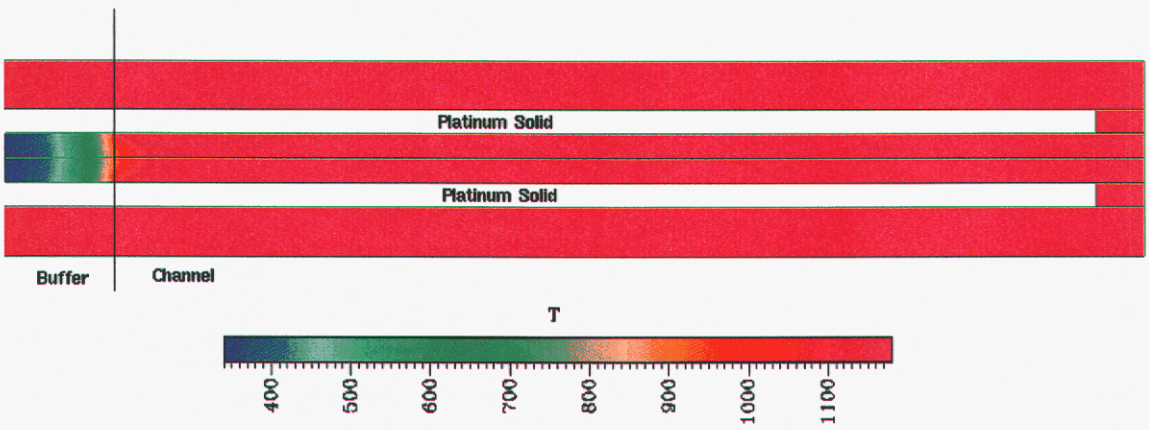

Figure 2 . Temperature for Case A.

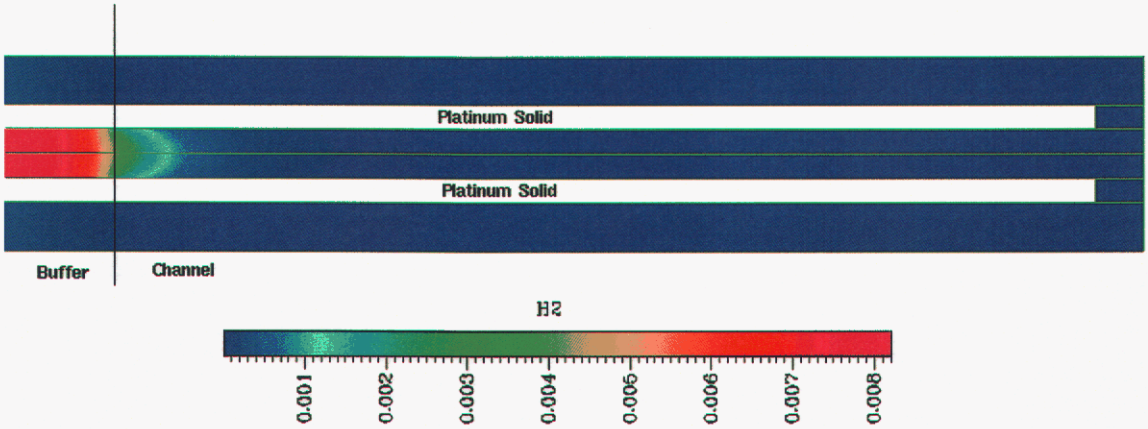

Figure 3. H_2 Species Mass Fraction for Case A.

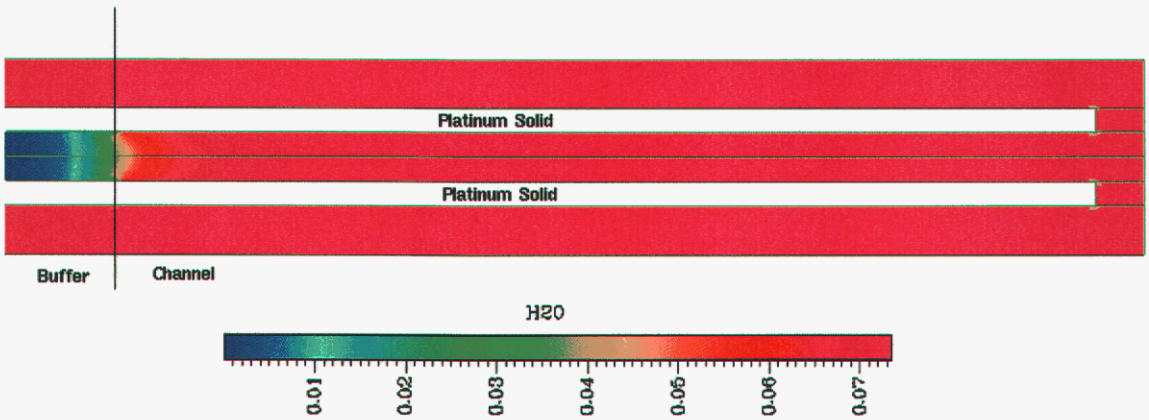

Figure 4. H_2O Species Mass Fraction for Case A.

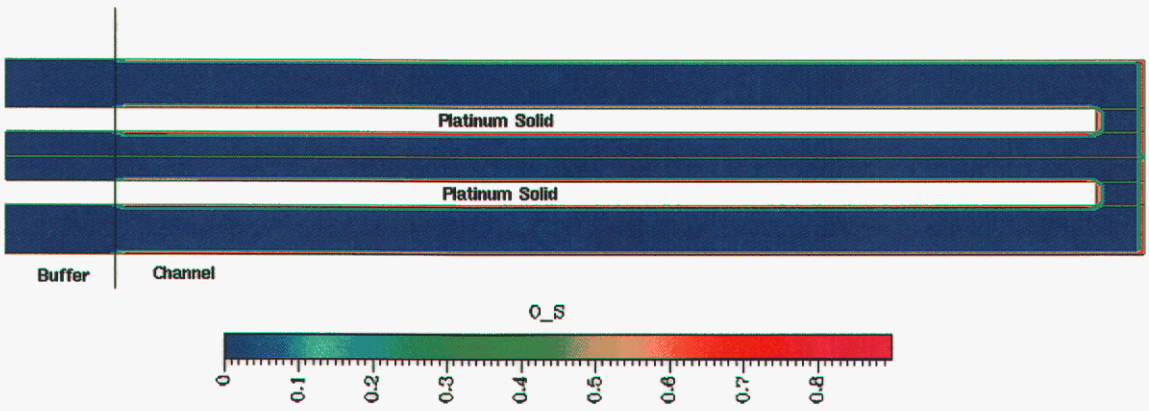

Figure 5. O Catalytic Surface Site Species Mass Fraction for Case A.

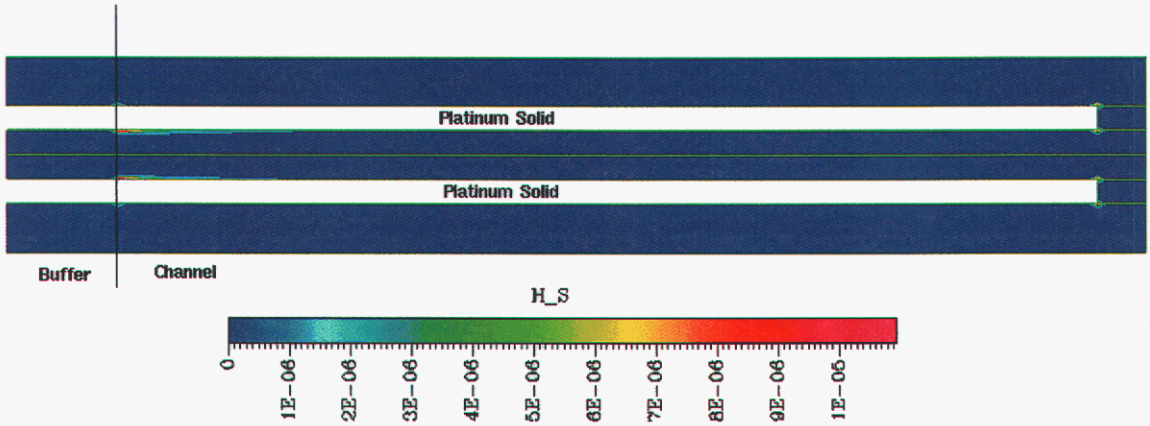

Figure 6. H Catalytic Surface Site Species Mass Fraction for Case A.

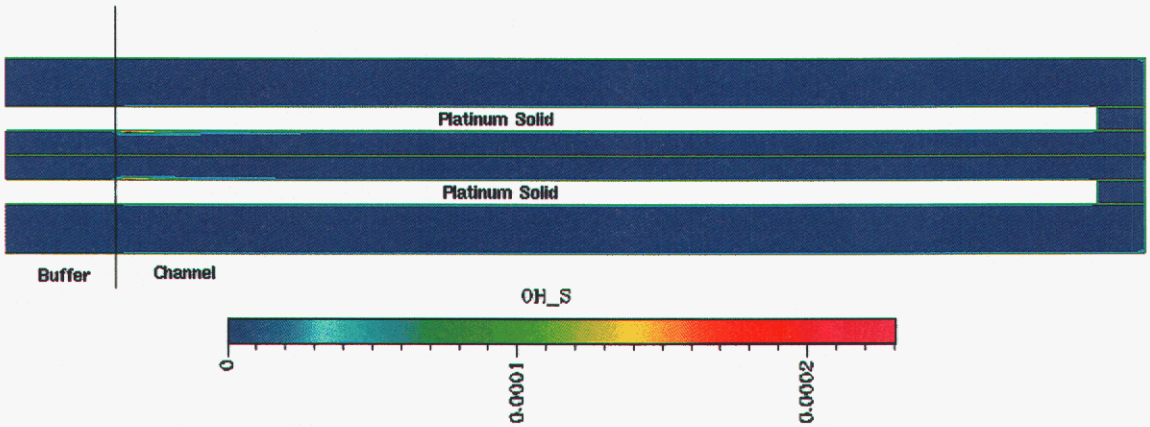

Figure 7. OH Catalytic Surface Site Species Mass Fraction for Case A.

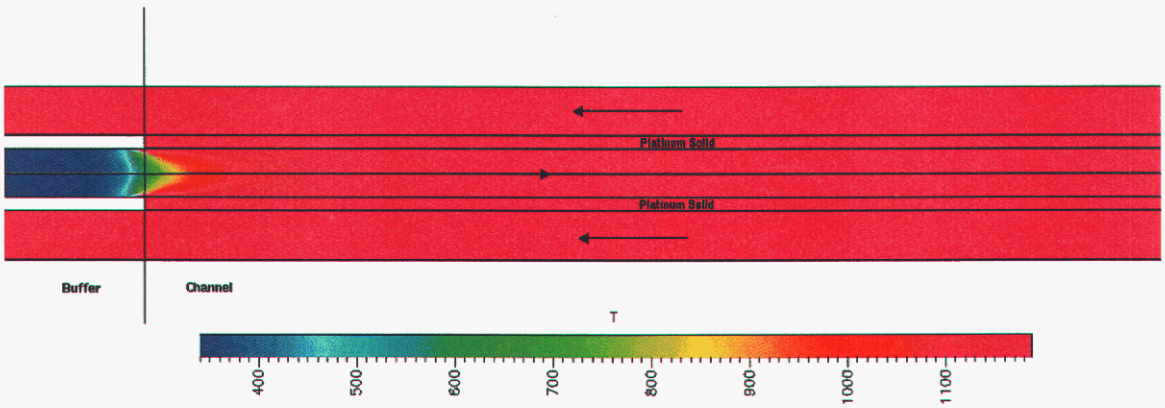

Figure 8. Temperature contours for Case B.

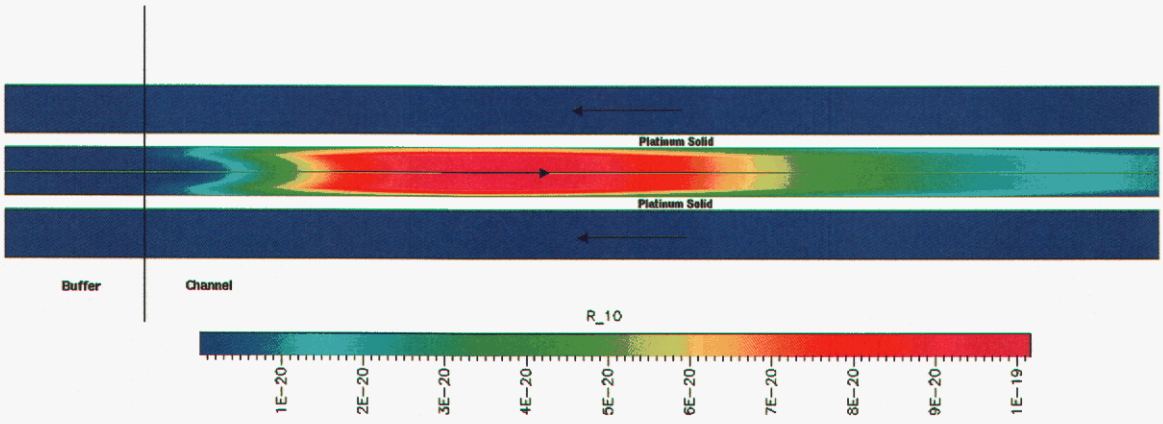

Figure 9. Contours of the reaction, $HO_2 + H \Leftrightarrow OH + OH$, for Case B.

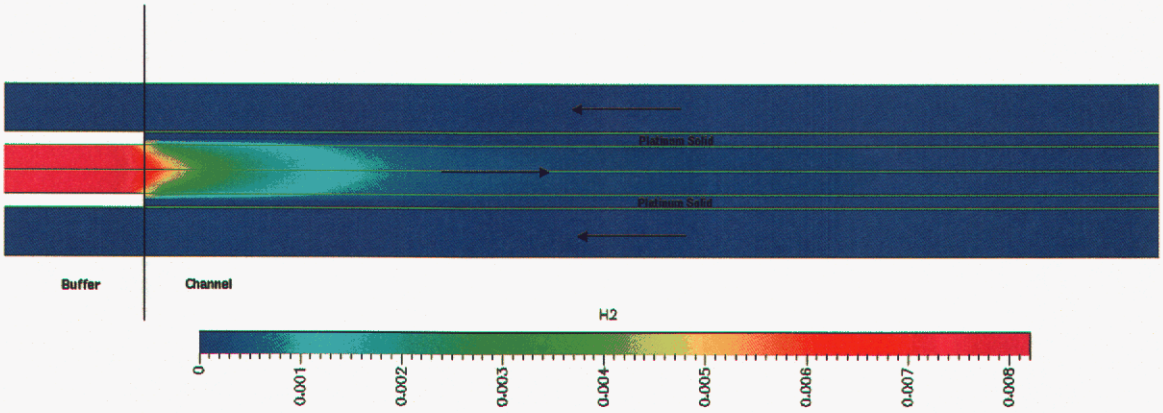

Figure 10. H_2 Species Mass Fraction for Case B.

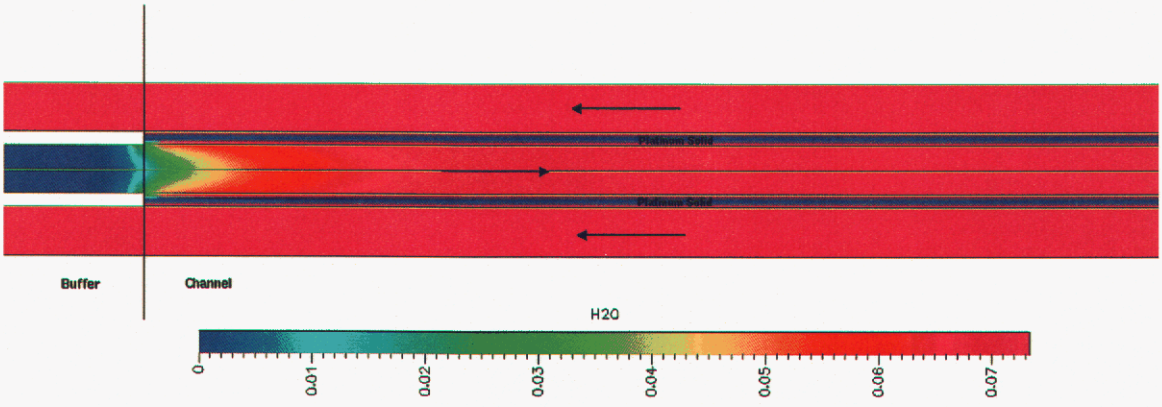

Figure 11. H_2O Species Mass Fraction for Case B.

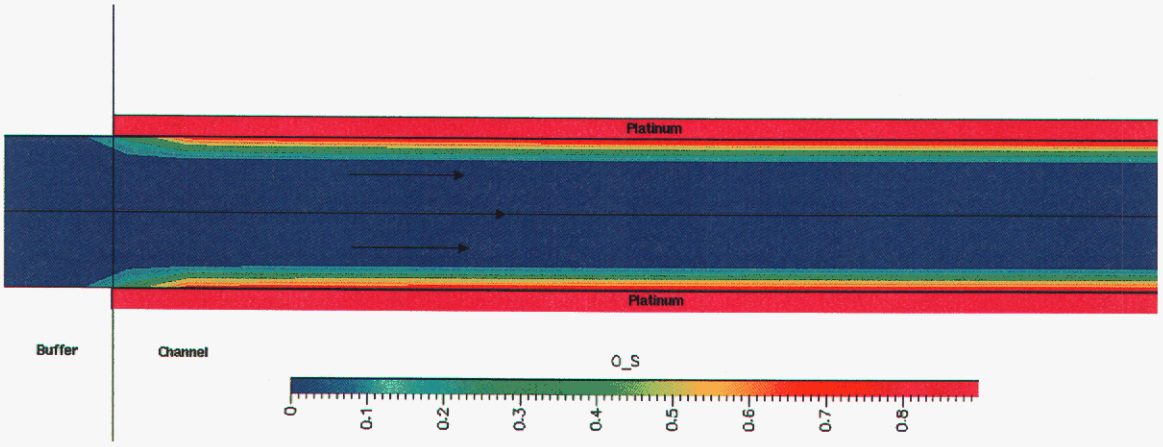

Figure 12. O Catalytic Surface Site Species Mass Fraction for Case B.

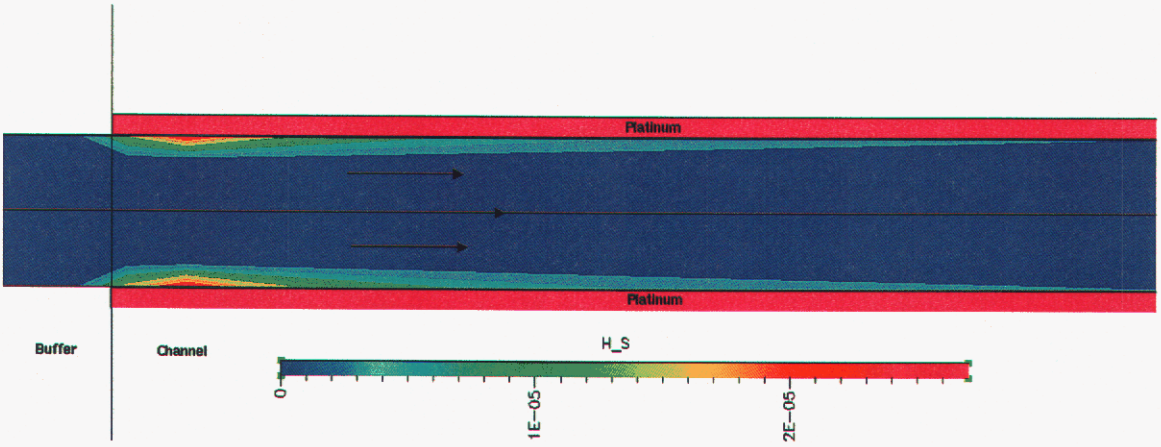

Figure 13. H Catalytic Surface Site Species Mass Fraction for Case B.

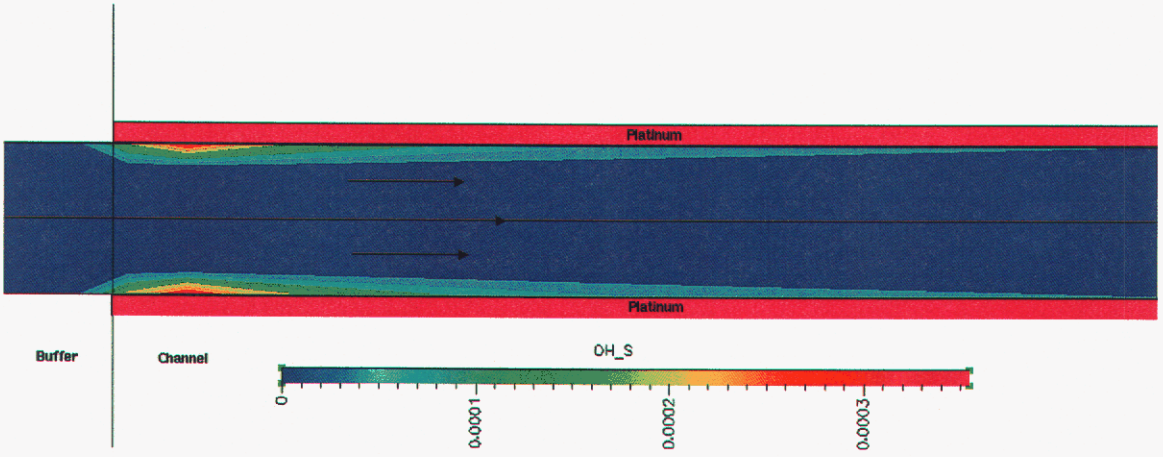

Figure 14. OH Catalytic Surface Site Species Mass Fraction for Case B.

Case C

In contrast with Case B, Case C is characterized by half the channel length. The inlet velocity is 0.7 m/s and an equivalence ratio is 0.31. The simulation results in a temperature gradient that is similar to Case B as shown in Fig. 15. The maximum temperature produced in this simulation was 1257 K, which is higher than Cases A and B. Similarly to Case B, Case C is also characterized by a transition to homogeneous phase chemistry as illustrated by the contours of the reaction, HO2 + H $\Leftrightarrow$ OH + OH, shown in Fig. 16. Figures 17 and 18 show that the consumption of H2 is accompanied by the formation of H2O in the first 1 to 2 mm in the channel. Again, significant saturation of the catalytic surface by O site species (Fig. 19) results in the reduction of catalytic chemistry downstream and the limited formation of H and OH radicals on the surface (Figs. 20 and 21).

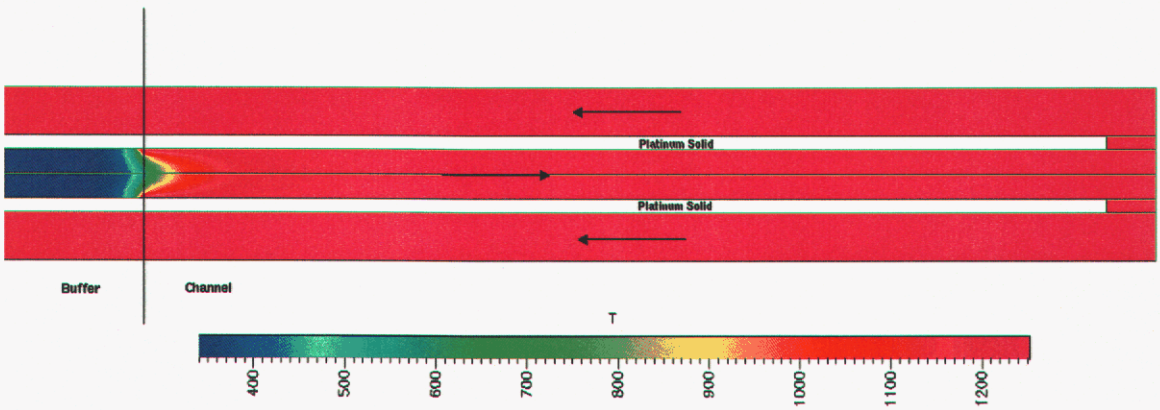

Figure 15. Temperature contours for Case C.

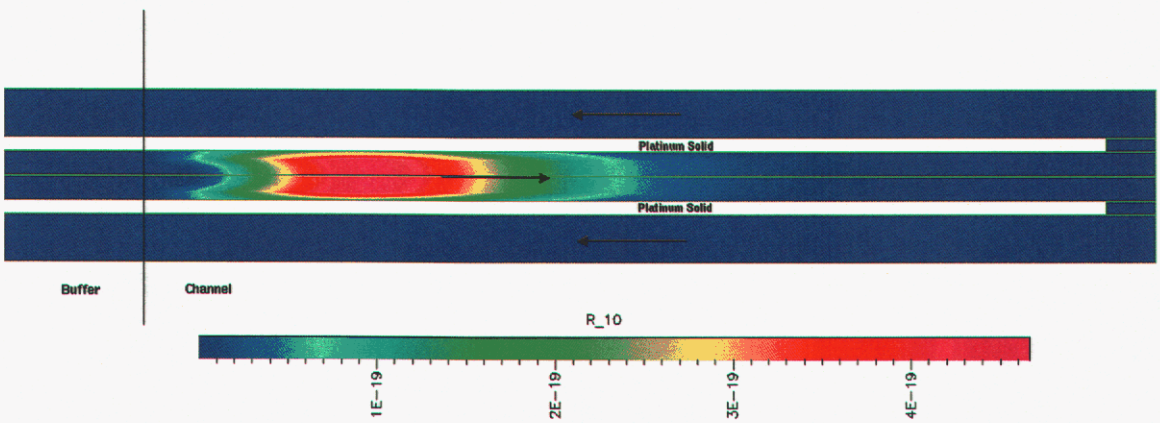

Figure 16. Contours of the reaction, HO_2 + H $\Leftrightarrow$ OH + OH, for Case C.

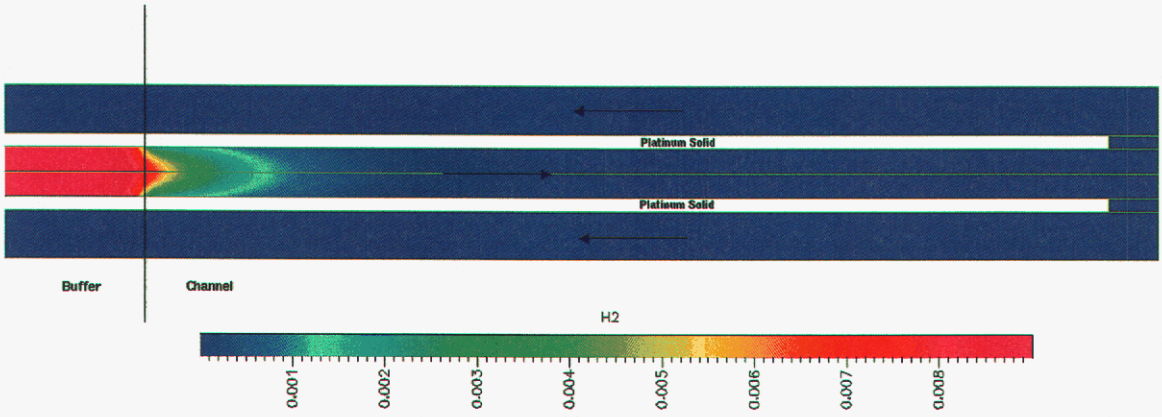

Figure 17. H_2 Species Mass Fraction of Case C.

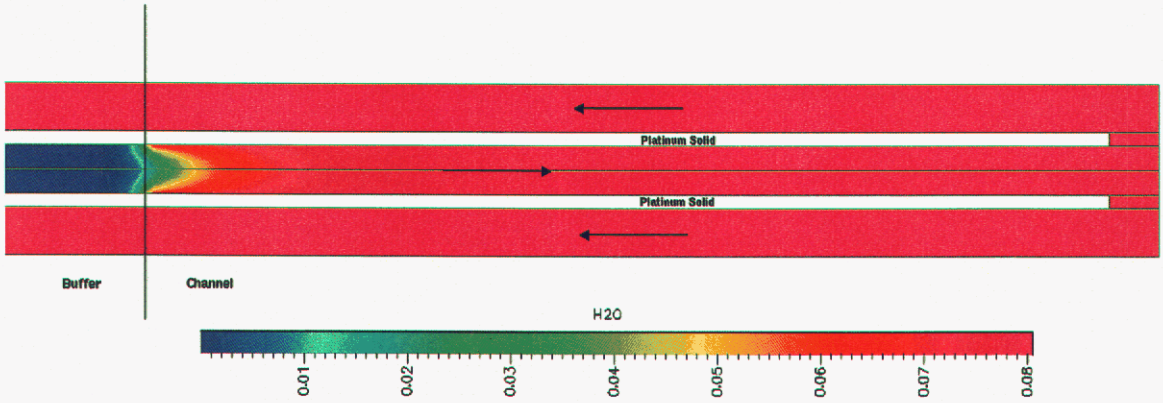

Figure 18. H_2O Species Mass Fraction for Case C.

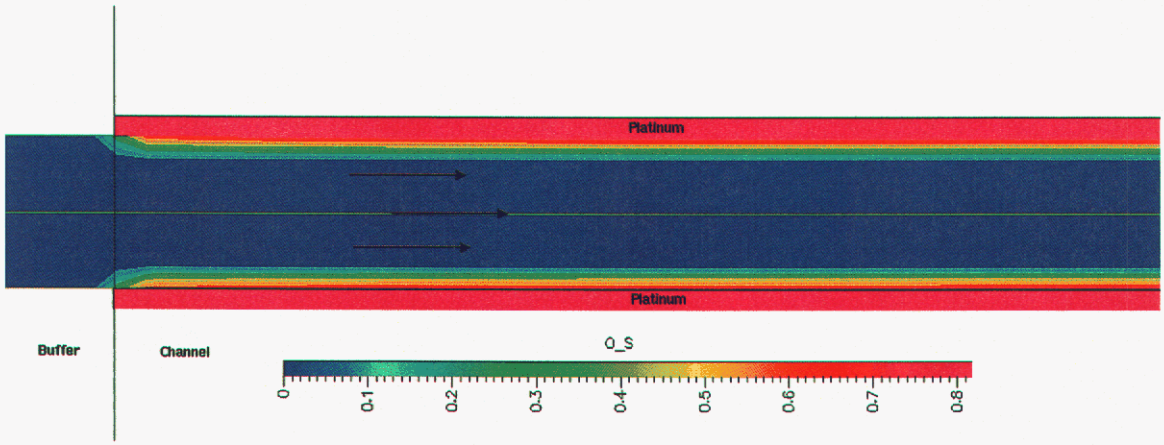

Figure 19. O Catalytic Surface Site Species Mass Fraction forCase C.

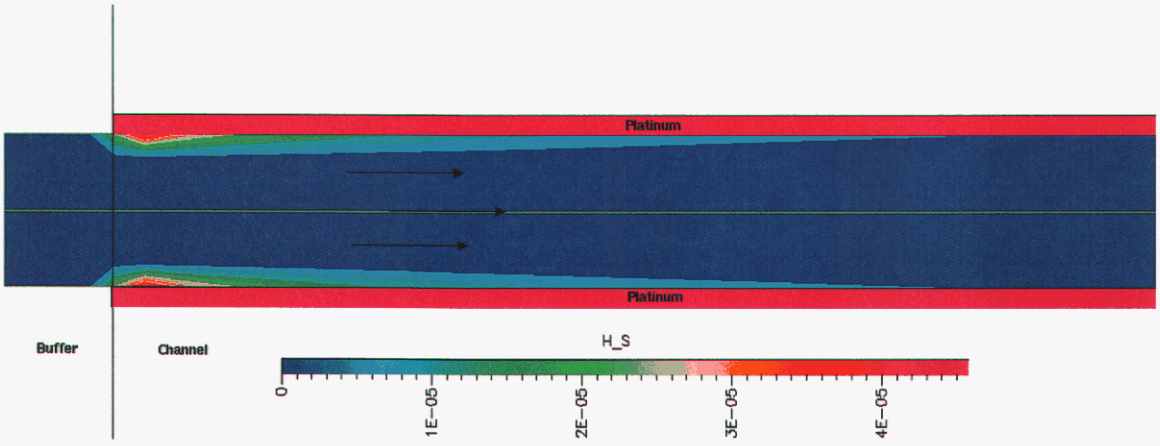

Figure 20. H Catalytic Surface Site Species Mass Fraction for Case C.

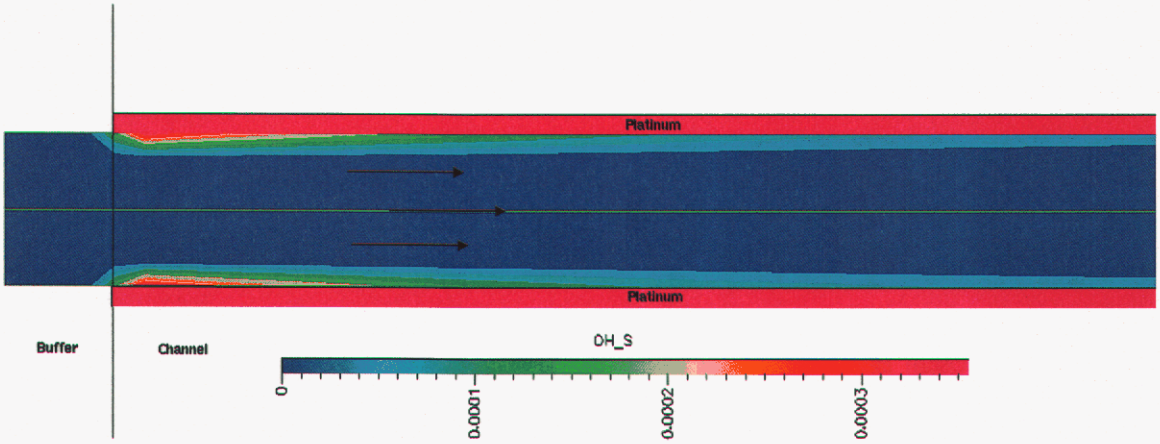

Figure 21. OH Catalytic Surface Site Species Mass Fraction for Case C.

Finally, Figs. 22, 23 and 24 show the evolution along the length of the channel of temperature, H_2 mass fraction, and the rate of reaction $HO_2 + H \leftrightarrow OH + OH$. The figure illustrates clearly the relatively fast evolution of chemistry in the channel and the onset of homogeneous chemistry.

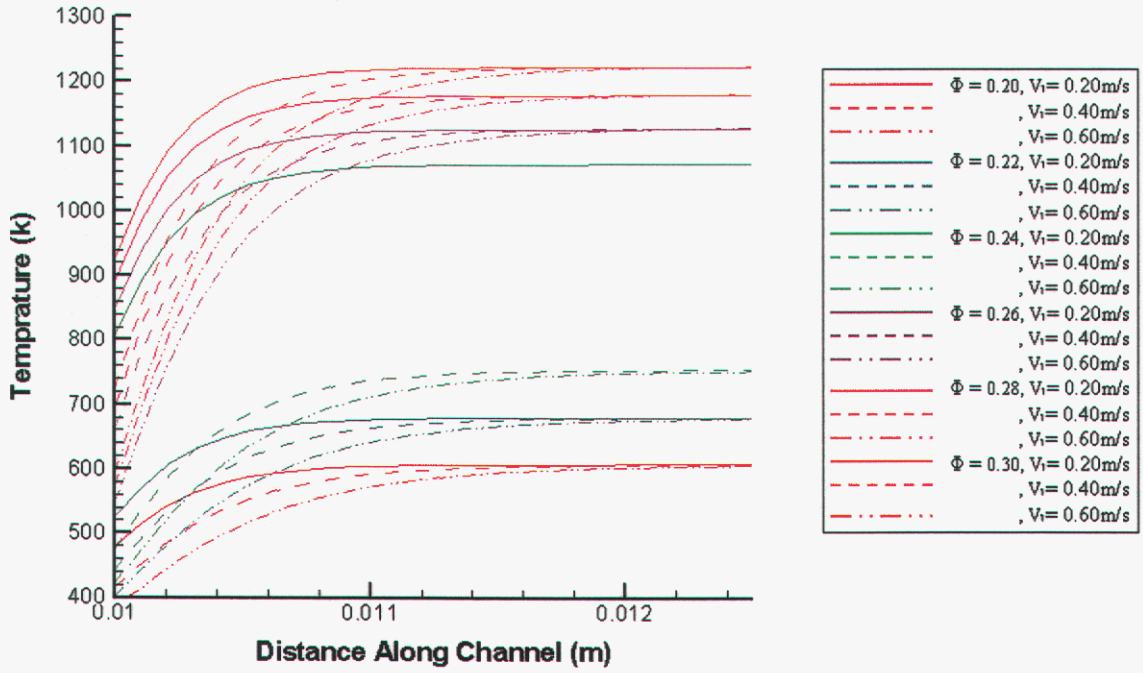

Figure 22. Effects of change in the combustors temperature over variations in fuel equivalence ratios (Φ) and inlet velocity (V).

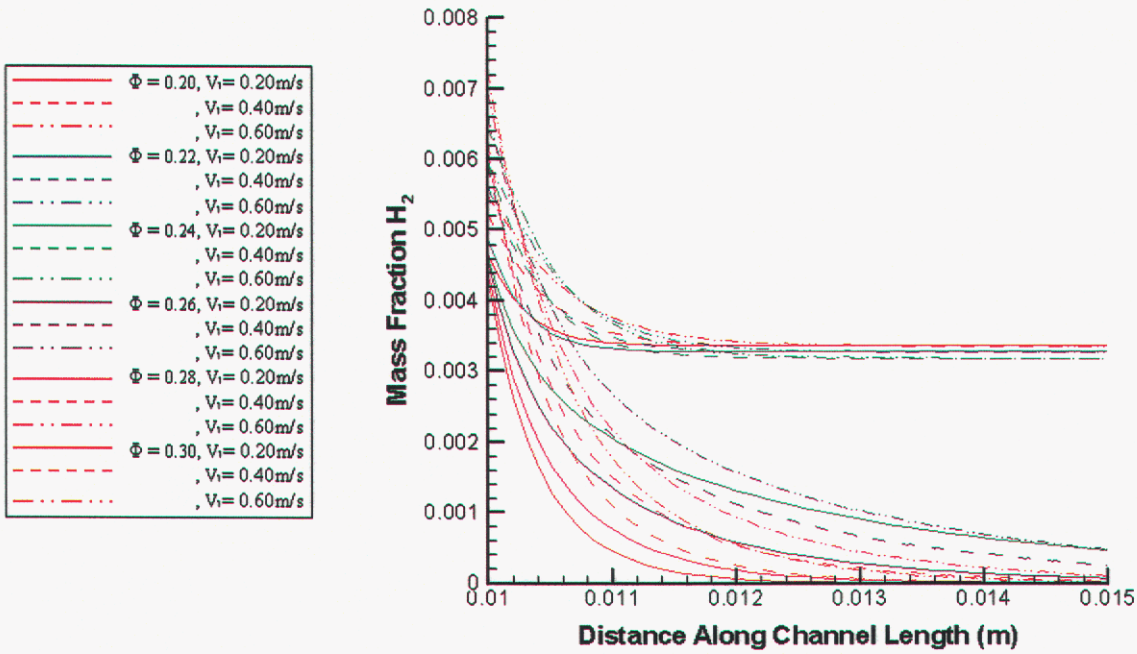

Figure 23. Changes in the mass fraction of H_2 along the channel with variation in fuel equivalence ratios (Φ) and inlet velocity (V).

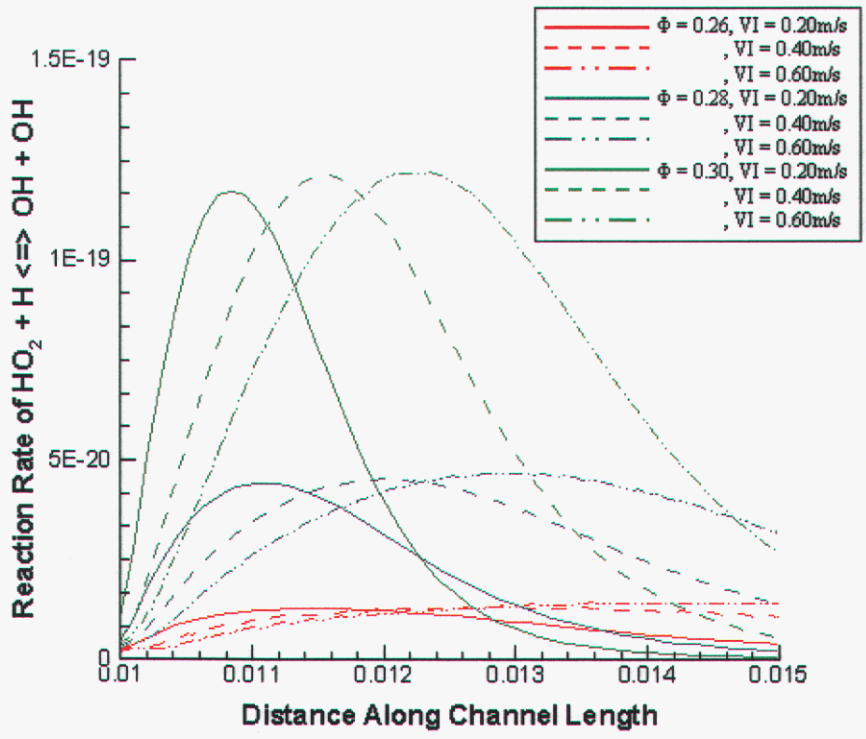

Figure 23. Changes in the relative intensity and location along the channel of reaction step $HO_2 + H \leftrightarrow OH + OH$ with variation in fuel equivalence ratios (Φ) and inlet velocity (V).

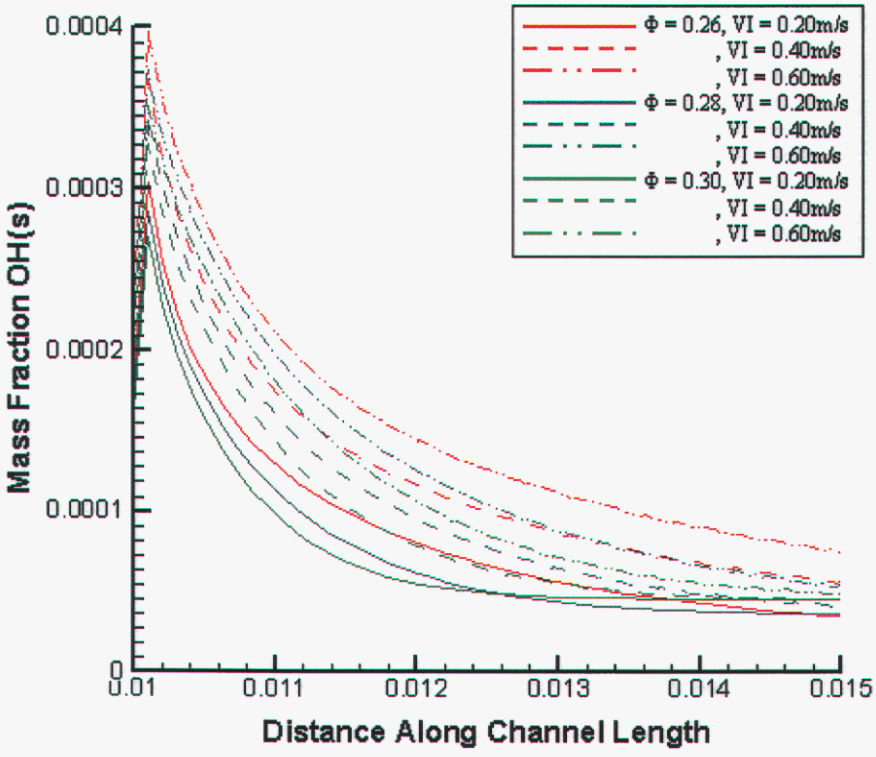

Figure 24. Changes in the mass fraction OH at the surface along the channel with variation in fuel equivalence ratios (Φ) and inlet velocity (V).

Thermal Management Strategies for Micro-scale Combustors

Role of Conduction Fins

The third set of simulations were concerned with identifying the relative roles of heat conduction, convection and radiation in transferring heat from the combustor to the regenerator as shown in Fig. 25. It is concerned with the implementation of a fin from the combustor to the regenerator. Normally, the regenerator may be made up of a porous material; but, at the scales considered here, an equivalent regenerator may be made up of a channel as shown below.

Working with only methods of convection and ignoring any heat loss through radiation we find that a conductive substrate with an extensive surface area operates best at heating a working fluid, for our simulations air. The model, as seen in Figure 25 shows a fin structure protruding slightly into the combustion chamber and extending out through a conductive porous media used to heat the working fluid.

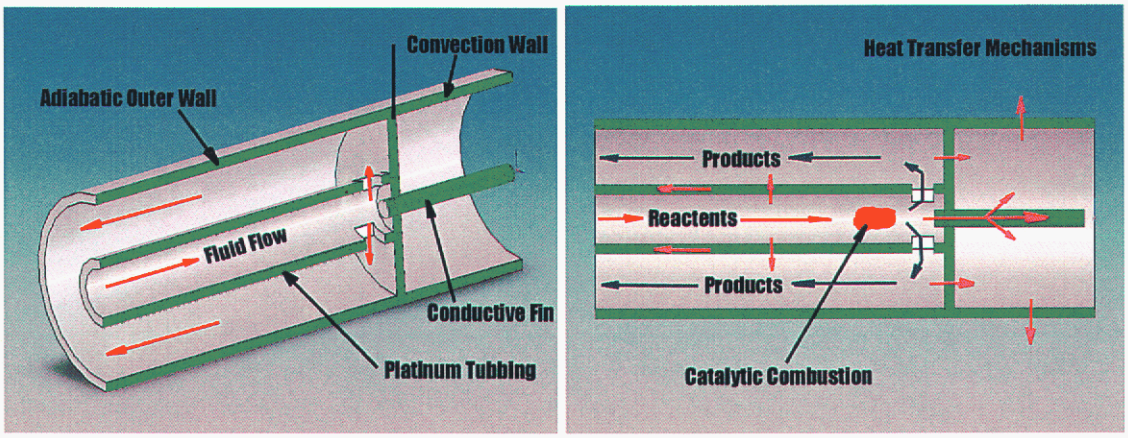

Figure 25. 2D geometry with axis-symmetric flow along the centerline was used to model the 3D tube within a tube combustor with a central fin extruded into a heat reservoir utilized through a working fluid such as air.

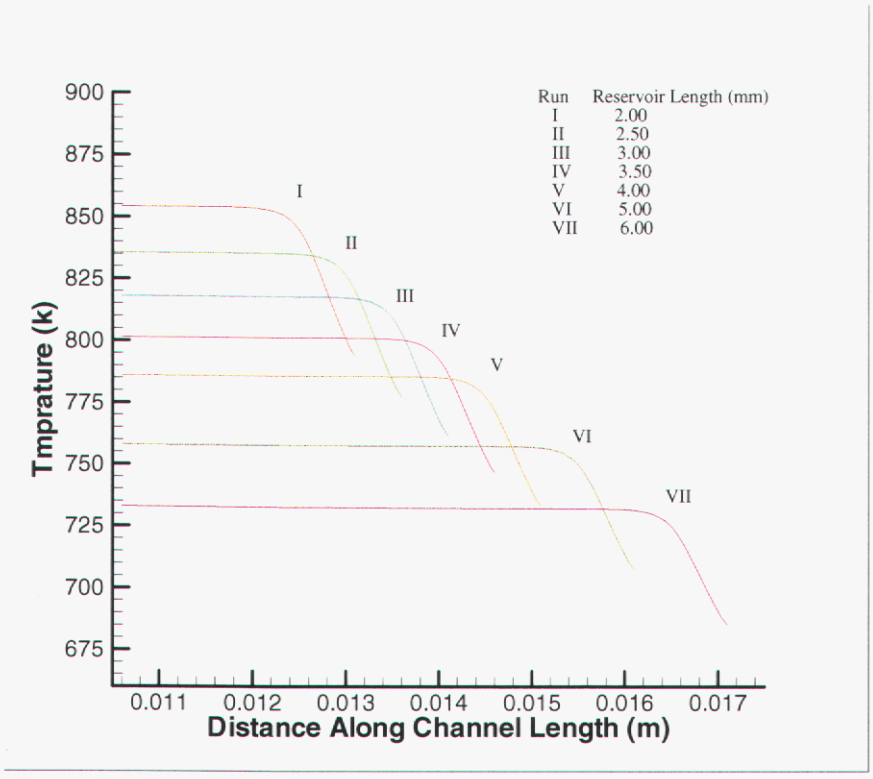

Figure 26. Temperature along the symmetry line of the heat reservoir with change in overall reservoir length.

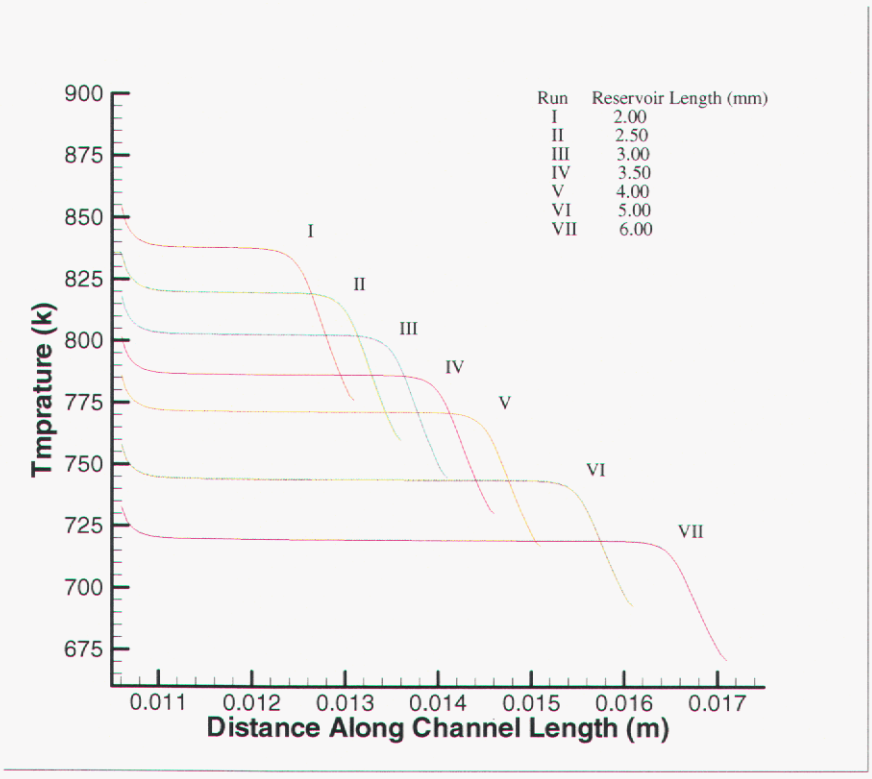

Figure 27. Temperature along the outer wall of the heat reservoir with change in overall reservoir length.

Role of Radiation

Trade-offs between different partition materials (transparent glass and highly emitting metal) and the role of a buffer zone between the combustor and the regenerator were explored. In the regenerator the heat from combustion is transferred to a working medium. It is separated from the combustor by a transparent plate. The regenerator consists of two sections; the buffer zone and the porous medium. The production of heat in the combustor is a continuous process while the conversion of this heat energy to power in the Stirling engine is an intermittent process depending on the working cycle of the engine. Hence a porous medium is used in the regenerator to store the heat of combustion during the idle phase of the engine cycle. The buffer zone is provided to alter the view factor between the transparent plate and the wall of the porous medium. Four cases were studied by varying the length of the buffer zone.

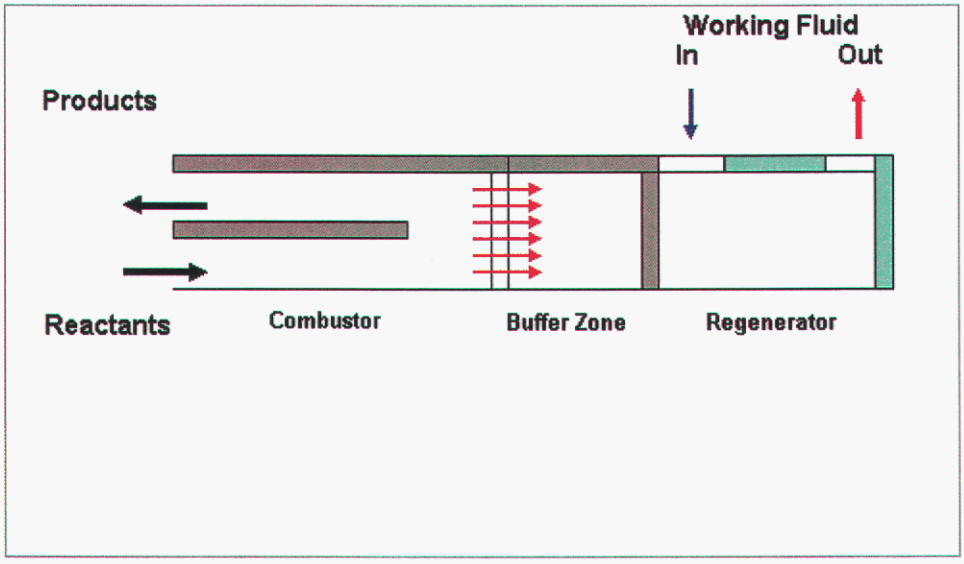

Figure 28. Schematic of the combustor

Run Conditions

The total length of the combustor is 2.075 cm, the inner tube inner diameter is 0.5 mm and the outer tube inner diameter is 2mm. The thickness of the tube is 0.15mm. The length of the buffer zone which determines the view factor for the amount of heat transferred by radiation is varied for the four cases studied given in Table 4.

	Length of the buffer zone(mm)
Case 1	1.25
Case 2	2.5
Case 3	3.75
Case 4	0.0

Table 4: Cases for which the distance of the porous medium from the glass plate is varied.

The porous medium is 2.5 mm in length with porosity and permeability 0.8 and 0.5m^2 respectively and has the working fluid flowing through it. The inlet velocities of the gas and the working fluid into the combustor and the porous medium respectively are 20cm/s.

The radiative properties are specified in Table 5 for all the volumes and surfaces. Here the gas is considered as a non participating medium.

	Emissivity			
Wavelength band(microns)	0-0.4	0.4-0.7	0.7-1000	1000-infinity
Glass	0.0	0.0	0.3	0.0
Gas	0.0	0.0	0.0	0.0
Platinum	0.0	0.3	0.08	0.0

Table 5: Radiative properties over the wave length bands [ref. 25,26]

Methodology & Results

CFDRC's CFD-ACE code was used for the purpose of simulation. It is a finite volume code in which various models like radiation model, heat transfer model and flow model can be implemented. The structure design for the combustor was built using CFD-GEOM (another product of CFDRC).There are three methods available in CFD ACEU solver to solve the radiation transfer equation in the radiation model. They are:

1. Surface to surface method
2. Discrete ordinate method and
3. Monte Carlo method

The discrete ordinate method can be applied to surfaces that are gray or non-gray either having a participating or a non-participating medium between them. The surface to surface method can applied for surfaces that are gray and that have no participating medium between them. The Monte Carlo method also requires a presence of a non-participating medium between the surfaces. Since the process of combustion produces gases that do participate in radiation Discrete Ordinate method was selected to solve the radiation transfer equation [ref. 27]. The radiation transfer equation is solved in pre-selected discrete directions. The emmisivities of the surfaces were specified as a function of wavelength over specified bands of wavelengths. The bands of wavelength selected were visible region and infrared region.

The radiation emitted by hot platinum heats up the surface of the porous medium. Glass is used as the transparent medium [ref. 26] as it is transparent in the visible region and opaque in the infrared region. The view factor for radiation from the glass plate to the wall of the porous medium depends on the length of the buffer zone. Hence by varying this length the amount of heat transfer to the porous medium through radiation can be controlled. There is also heat transfer by conduction through the outer platinum tube to the wall of the porous medium. The working fluid is passed through the porous medium to absorb the heat for conversion to power.

In cases 1,2 and 3 the heat from combustion is transferred to the porous medium through the buffer zone. In case 4 the there is no buffer zone. The wall of the porous medium is in direct contact with the hot gases of combustion. Figure 29 summarizes the heat transferred to the porous medium for the four cases.

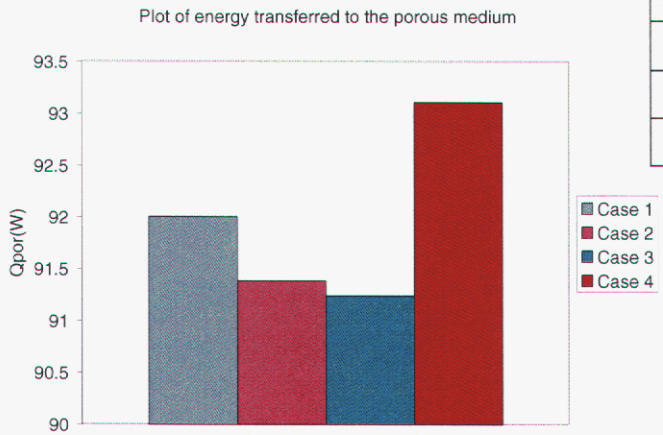

Q in W	Qin	Qout	Qpor
Case I	139.0344	4.70E+01	92.00277
Case II	139.0344	4.76E+01	91.38538
Case III	139.0344	4.78E+01	91.23905
Case IV	139.0344	4.59E+01	93.10562

Figure 29: Plot of heat transferred to the porous medium

Figure 30 shows the plot of the temperature at the outlet of the combustor. The outlet temperature for case 4 is the least compared to the other three cases indicating higher quantity of heat transferred to the porous medium.

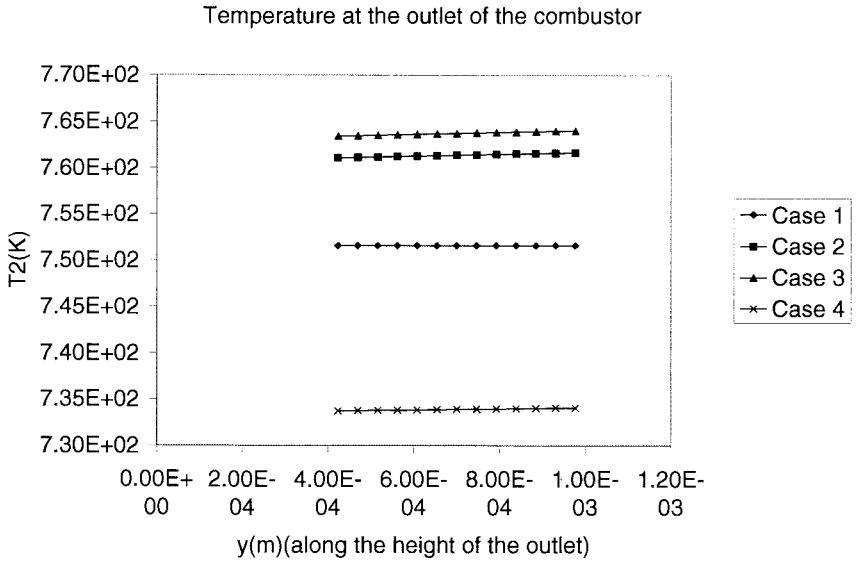

Figure 30: Plot of temperature at the outlet of the combustor

Table 7 shows the radiative heat flux and the percentage of total heat flux transferred through radiation through the wall of the porous medium facing combustor.

Table 7: Radiative heat flux.

	Radiative heat flux(W/m**2)	% of total heat flux transferred through radiation
Case I	256.54	4.61
Case II	289.5254	4.2
Case III	325.3595	4.1
Case IV	1129.99	53.9

Three more simulations were carried out with the same geometries as in case 4. In these simulations the inlet velocity of the working fluid into the porous medium was varied as 0.05, 0.5, 0.9 m/s respectively. The results are tabulated in Table 8.

Table 8: Energy transferred to the porous medium

Energy in W	Qin	Qout	Qpor
Case 4a	139.0344	1.15E+02	24.5339
Case 4b	139.0344	4.63E+01	92.7316
Case 4c	139.0344	4.08E+01	98.2273

The energy transferred to the porous medium is greatest in case 4c where the inlet velocity is 0.9 m/s and least in case 4a where the inlet velocity is 0.05 m/s. Figure 31 shows the plot of temperature at the outlet of the porous medium for the above three cases. Clearly the temperature at the outlet of the porous medium for case 4a is greater than that for case 4b and 4c. But the energy transfer-rate is least in case 4a. This is due to the fact that there is no new fresh working fluid in case 4a to absorb the energy from the combustor.

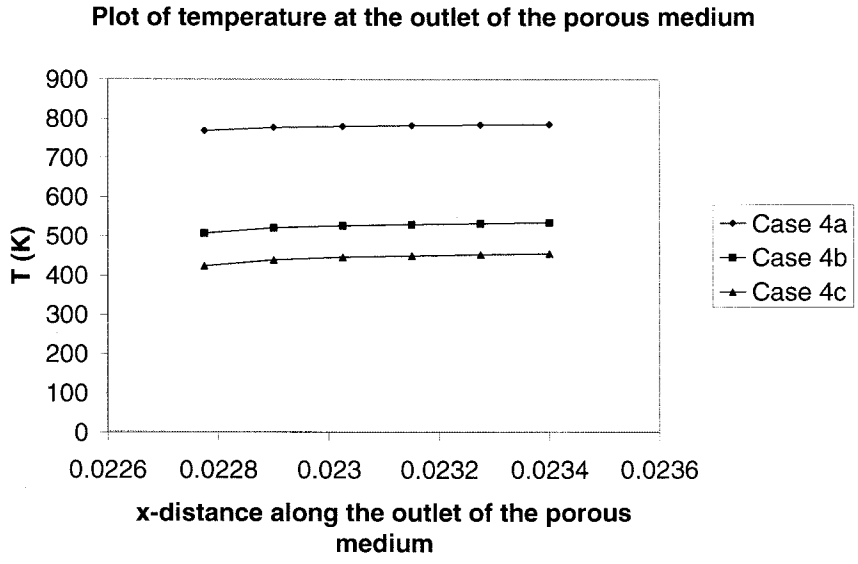

Figure 31: Plot of temperature along the outlet of the porous medium for the cases 4a, 4b and 4c.

Conclusion

From the above data it is clearly seen that the quantity of heat transferred through radiation cannot be neglected. As the length of the buffer zone is reduced the total energy transferred to the porous medium increases. Hence it is recommended to have a regenerator without a buffer zone. Also the radiative heat flux through the wall of the porous medium facing the combustor increases by 9 percent for every 0.15 mm decrease in the length of the buffer zone. Finally for the case with no buffer zone the heat transferred through radiation constitutes 50 percent of the total heat flux across the wall of the porous medium. Hence radiation cannot be neglected. It is recommended to have the inlet velocities for the porous medium to be in the range of 0.2 to 0.5 m/s. Below 0.2 m/s the energy transfer is not efficient as all the energy is lost to the outlet of the combustor, greater than 0.5 m/s the temperature increase in the working fluid is less.

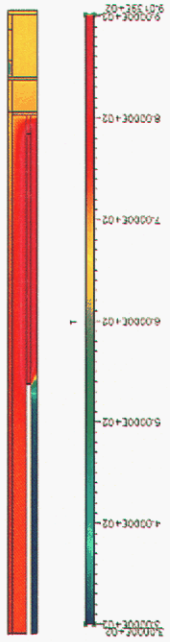

Figure 32: Temperature contour plot for case1.

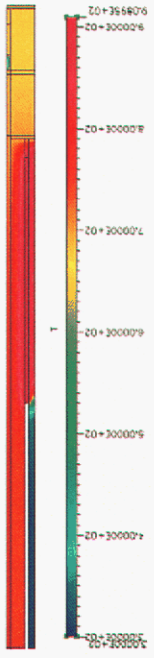

Figure 33: Temperature contour plot for case2.

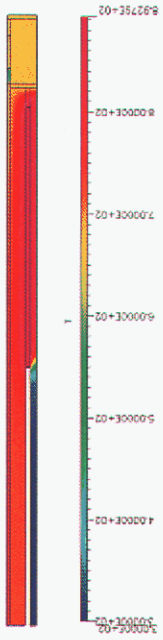

Figure 34: Temperature contour plot for case4.

Simulation Conclusions

The above studies of the mode of chemistry and the roles of conduction, radiation and convection in the thermal management of micro-scale combustors provide some important guidelines to improve the design of these combustors and their integration in a heat engine.

1. Channel dimensions play a dominant role in determining the mode of combustion inside the channel. The present results show that by reducing the channel size, homogeneous chemistry (gas phase chemistry) was achieved resulting in relatively higher temperatures than heterogeneous (catalytic chemistry).
2. Both conduction and radiation play important roles in heat transfer to the regenerator, and both modes of transfer should be used in combination to increase the fraction of heat that is transferred to the regenerator.
3. For conduction, the establishment of a direct connection between combustor and regenerator through a fin results in increased rates of heat transfer to the regenerator.
4. Radiation from an opaque metal is far more efficient than that of a transparent material, such as glass. The heat metal emits radiation to the regenerator directly. The relative inefficiency of glass in transmitting radiation to the regenerator eliminates the need for a buffer zone used to modulate the view factor to the regenerator.

This page intentionally left blank.

MICROCOMBUSTION EXPERIMENTS

The purpose of the experimental effort in micro-combustion was to study the feasibility and explore the design parameters of excess enthalpy combustors. The efforts were guided by the necessity for a practical device that could be implemented in a miniature power generator, or as a stand-alone device used for heat generation.

The main requirements of such a combustor are reduced size and increased power output. As will be shown subsequently, both the excess enthalpy concept and the catalytic mode of combustion proved indispensable in satisfying these requirements. The principle of operation is shown in figure 1 (top). Fuel and oxidizer, in this case methane and oxygen, would flow through an inner channel with bulk velocity u_i and exit as products with bulk velocity u_e from an opening at the outer channel. For the device to be easily operable, ignition had to take place at the exit, and a flame had to propagate backwards through the space between channels and anchor at the tip of the inner tube, as shown in the figure. This, in turn, implies that the velocities had to be small enough in these areas for flame flash-back to occur. At the same time, power requirements dictate that the volumetric flow-rate of the premixed gases through the device be as high as possible. These two velocities act as the main design parameters of the problem.

The practical implementation of the device is shown in the middle of figure 1. Solid tubes, made of 80% Platinum - 20% Iridium were used in the construction of the catalytic inner channel. Crystal tubes were used for the outer channel, and air-curing ceramic adhesive was used for sealing joints and ends of the device. Some devices were constructed with a stainless inner tube, to isolate the effect of the catalyst in the combustor. A basic configuration that was used extensively is shown in figure 1: an inner metal tube of 500 μm (ID) within an outer crystal tube of 3 mm (ID). One particular condition of flow-rates (25 cc/min CH_4 and 50 cc/min O_2) corresponding to stoichiometric premixture leads to the cases shown in the photograph of figure 1. Since this is homogeneous premixed combustion, similar results could be obtained with stainless inner tubes. This particular condition corresponds to values of $u_i = 6.3$ m/s and $u_e = 0.4$ m/s. The latter allows flash-back to occur, and a flame to be stabilized at the tip of the inner tube. The former is much higher than the stoichiometric (adiabatic) flame speed ($s_L \sim 0.35$ m/s) and hence no back-propagation is seen –at first- within the inner tube. Power production can be calculated to 2.8 W, assuming full burning and no heat losses. Such a configuration can be scaled up to satisfy higher power requirements, as long as the exit velocity u_e is kept small enough for flash-back to occur. While no catalyst is needed in this configuration, combustion is localized in a small space, where temperatures can be very high and control of the heat losses is minimal.

The presence of the catalytic tube leads to a different combustion mode, as shown in figure 2. After an initial period during which the temperature of the metal solid increases, catalyst ignition takes place, the visible homogeneous flame disappears from the tip of the inner tube, and the combustion is happening inside the inner tube. This transient behavior can be seen in the composite photograph of figure 3. Heating of the inner tube is taking place during the first 230 s, as evidenced by the increasing radiation emanating from the catalytic tube. Approximately at this time, the radiation from the metal increases substantially, the bluish homogeneous flame disappears, and a glowing 'plug' indicating the presence of catalytic combustion travels upstream. The camera was stopped down between the pictures taken at t = 290 s and 390 s, so as to bring out the details of the radiating material. Specifically, as can be seen in the later instances in the sequence, it is the inner catalytic tube that radiates, and hence combustion is taking place

inside it. Steady state is achieved at about 1000 s, when the catalytic front has traveled to the bottom of the tube. Both the initial heating period as well as the propagation of the catalytic front depended strongly on the preheating of the inner tube. At the base of the device (not shown in the figure) is a large metal mass of stainless fittings used for gas delivery. The large thermal inertia of this mass acts as a heat sink, slowing in effect the heating of the metal tube. The effect is compounded by the large heat losses to the ambient environment though conduction of the exposed outer tube, as well as by radiation. Substantial preheating of the catalyst must take place before either catalytic ignition or propagation can take place and this is the reason for the especially long times seen in this particular example. If the flame were to be extinguished and the whole sequence repeated, the time required would be in the order of 1-2 s. The same effect could be accomplished by preheating the fittings at the bottom of the device, and ultimately eliminating them in the case of a practical system. This sequence of events relating to catalytic combustion was never seen for a stainless inner tube, even after one hour of operation and preheating of the metal fittings.

A similar configuration (tube-within-a-tube) was chosen for a next implementation of the device, shown in figure 4. The exposed length of the catalyst tube was reduced to 10 mm, corresponding to the active length of catalytic combustion seen in figure 2. The catalytic tube size was increased to 1 mm (ID), thus quadrupling the area, and potentially the flow-rate and the power production. Additionally, most of the outer tube surface was shielded using ceramic, in order to minimize the heat looses to the environment. These resulted in a device that had virtually no catalytic ignition and propagation lag. A particular case of the device under combusting condition is also shown in figure 4_exp. Under the available infrastructure the maximum flow-rates were limited, and as a result values of 50 cc/min CH_4 and 100 cc/min O_2 were used, resulting in a velocity of $u_i = 3.15$ m/s and an estimated power generation of 5.6 W. The effectiveness of the shielding was judged by thermometry: a thermocouple was embedded in the ceramic plug before it cured, and a temperature of 420 K was obtained. This indicates that the temperature gradients resulting in heat fluxes towards the ambient can be minimized.

As will be shown subsequently, the temperatures prevailing during the catalytic combustion are much smaller than the ones during the homogeneous flame case. This, in turn, implies the possibility for reduced heat losses, as well as for control of a realistic device. Scaling of the device to larger sizes, and in particular, making it amenable to higher flow-rates and heat generation is easily accomplished for an excess enthalpy combustor employing a catalyst. Another design that was examined during this study is shown in figure 5. The design is a departure of the axially symmetric cases that were easier to build as prototypes. It relies on a 2D 'stamp' configuration, whereupon a ceramic base is used to form the combustor walls and act as heat shield. The combustor shown in figure 5 was fitted with a sapphire window, so as to make the inside visible. A catalytic tube of 1-mm ID was used to form the inner channel in this case, with dimensions similar to the one used in the previous axisymmetric configuration. The combustor was operated at the same flow-rates, resulting in theoretical heat generation of 5.6 W. In this combustor, as was the case in the previous configurations, the size of the exit opening has to be large enough to allow for small exit velocities (~ 0.4 m/s) under given flow-rate through the device.

In order to acquire as much quantitative information as possible regarding the operation of the catalytic excess enthalpy combustors, a series of experiments were conducted. While all the experimental prototypes offered optical access, in practice the only technique that could be used

in-situ was optical pyrometry. A single-color radiographic camera was used for that purpose. It was found that the results were purely qualitative, because of the presence of the crystal and the continual fouling produced by combustion products. A simpler configuration was studied instead, namely the combustion using a single catalytic needle. As shown in the left side of figure 6 a flame could be established at the tip of the catalytic needle, similar in all respects to the ones used in the first combustor prototypes (0.5 mm ID, length ~35 mm). In the absence of heat recirculation, i.e. without the excess enthalpy of the products, no catalytic combustion could be initiated or propagate along the catalytic tube. This case corresponds roughly to the ignition phase of an excess-enthalpy combustor. The two cases are not identical, as the outer tube of the former case acts as a heat shield. The present case, with the associated large heat losses incurred to the environment, may be considered as a 'worst-case' of the excess enthalpy combustor. To mimic the presence of the heat recirculation, and in order to induce catalytic ignition, an external heat source was applied at the metal needle. Catalytic combustion would initiate, as shown in the middle of figure 6, and upon removal of the external source the catalytic front would propagate upstream and stabilize at the bottom of the needle, as shown in the right side of figure 6.

Temperature and major species composition was measured at these two extreme conditions, using the multiscalar measurement capabilities of the Turbulent Combustion Laboratory. Simultaneous line measurement of Raman/Rayleigh and CO Laser Induced Fluorescence provided information on major species mass fractions and temperature along a 6-mm line of the laser probe. The resolution, based on individual probe elements was 200 μm. The measurements consisted of an ensemble of 50 laser shots taken at 2 mm vertical distance from the needle tip (corresponding to 4 inner diameters). A scaled schematic of the probe volume is shown in figure 6. Distancing the laser probe from the tip of the tube was necessary to avoid stray-light reflection from the metal. As a result, the measurements do not capture the exit gas composition and temperature; rather, entrainment from the ambient air results in temperature reduction as well as dilution of the combustion products. Since the flow is laminar (cold Reynolds number of ~300) the data from each probe element were averaged to produce a measurement of the laminar properties in the field. For the case of catalytic combustion, the highest temperature of the metal surface was also measured by radiography. The result is somewhat qualitative in nature due of uncertainties in the emissivity of the metal surface under hot conditions.

The spatial profiles from the homogeneous flame and the heterogeneous catalytic case are shown in figure 7. Both were operating under stoichiometric conditions ($\phi = 1$) and flow-rates of 25 cc/min CH_4 and 50 cc/min O_2, corresponding to the results shown in figures 1 to 3. Temperature and major product species H_2O and CO_2 mass fraction are plotted against radial coordinate r, normalized by the inner diameter of the tube d. Immediately apparent from this figure is the pronounced difference between the two cases. Temperatures in the flame case are much higher than in the catalytic case. While both measurements are biased towards lower values due to air entrainment, it is clear that the homogeneous flame case reaches temperatures close to the adiabatic (~3000 K) whereas the exit products of the catalytic tube show a peak temperature of 500K, corresponding to the lower temperatures that prevail during catalytic combustion, as well as heat losses along the length of the tube. The H_2O and O_2 profiles also show very pronounced differences. The results point to another difference between the two cases: the spreading rate of the flame is much higher than the catalytic case. A value of 0.45 is expected for Y_{H2O} at equilibrium; the flow-field within the homogeneous flame shows the effects of entrainment from the ambient, evidenced by the broadening of the water profile and lowering of maximum value.

A parametric study of the catalytic combustion case was also carried out. The methane flow-rate was kept constant (25 cc/min) while the oxygen flow-rate was varied between 35 and 75 cc/min. In this manner the premixture strength was varied between ϕ= 1.33 and 0.68 respectively. The multiscalar technique was used for measurements temperature and composition, in the same manner as before, while the radiographic technique was used to measure temperature of the metal catalyst. The two techniques were applied separately in similar conditions. The maximum product temperatures (T_{max}) recorded in the flowfield are plotted in figure 8 against mixture strength. The nitrogen mass fraction is also plotted at the right ordinate. Since nitrogen was not part of the premixture flowing through the tube, we may use that measurement to correct the bias due to entrainment. Specifically, all of the nitrogen is attributed to air entrainment ($Y_{N2}^{air} \approx Y_{N2}^{*}$), and the proportional contribution of air entrainment to the oxygen mass fraction can be calculated as $Y_{O2}^{air} \approx Y_{N2}^{air} / 3.25$. Then the 'corrected' oxygen fraction that originated in the premixed stream becomes $Y_{O2}^{corr} \approx Y_{O2}^{*} - Y_{O2}^{air}$ (starred quantities refer to the original mass fractions measured in the field). The final mass fractions (Y_i) can be calculated by a simple renormalization to unity, using Y_{O2}^{corr} and the originally measured Y_i^{*} mass fractions for the rest of the species: $Y_i = Y_i^{*} / (\sum Y_i^{*} + Y_{O2}^{corr})$. Finally, a corrected temperature can be calculated using a simple enthalpy conservation, and assuming equal heat capacities for all gases in the mixture: $T\,(1 - Y_{N2}^{air} - Y_{O2}^{air}) = T^{*} - (Y_{N2}^{air} + Y_{O2}^{air})\,T_o$, where T_o is the ambient temperature. This corresponds to a simple mixing rule that assumes ambient air at T_o, mixing by entrainment with hot products at temperature T, to produce the measured biased temperature T^{*}. Figure 8 shows the results for the corrected temperature measurement. It should be noted that the above correction becomes inaccurate in areas where air dominates the mixture, since the term $(1 - Y_{N2}^{air} - Y_{O2}^{air})$ becomes smaller than the experimental accuracy leading to non-physical 'corrected' temperatures T. Equally, the above simple correction scheme cannot work in the high temperature regions of the flow-field, because the assumption of constant c_p becomes tenuous. For these reasons no correction of the spatial measurement profiles through the homogeneous flame (figure 7_exp) was attempted.

The maximum temperature of the exit gases (corrected) is also plotted in figure 9, along with the temperature of the catalyst surface determined by radiography. The effect of the heat losses to the environment is apparent by the difference between the temperatures. Equally evident is the difference between the highest temperature achieved during catalytic combustion and the ones achieved through homogeneous combustion (figure 7). The monotonic trend of T_{gas} versus ϕ can be understood in terms of heat losses: the leaner premixtures correspond to higher total flow-rates which lead to smaller transient times through the needle, and hence smaller heat loss to the ambient. A similar argument may explain the shape of $T_{catalyst}$: based on the classic behavior of the adiabatic flame temperature in homogeneous flames we may expect a maximum at values slightly richer than stoichiometric. The presence of a monotonic trend of higher heat losses for the richer mixtures shifts this maximum to a value of $\phi < 1$.

The fuel and oxygen composition maximum measured at the centerline (and corrected) is shown in figure 10. Unburned fuel can be seen in the products for the rich cases and the reverse is true for oxygen in the lean cases. The small presence of fuel in the lean case, where it is the deficient species, is probably due to experimental errors. The mass fractions of the major products (Y_{H2O} and Y_{CO2}) are plotted in figure 11. The values expected under fully burning stoichiometric mixture are also shown by dotted lines. The profile of Y_{CO2} reaches a value close to the theoretical one at $\phi = 1$, while

Y_{H2O} reaches a value higher than the expected one, at a rich condition. This is probably due to experimental errors, as well as errors in the correction process that was used. The two profiles are qualitatively very different in the rich cases, with the CO_2 composition showing a sharp decline past the stoichiometric condition, while the water composition shows a smooth behavior and a maximum value at $\phi \approx 1.2$. At this position the CO_2 composition shows a local minimum instead. The differences between major products can be better understood by examining the profiles of the intermediate species (CO and H_2) produced during methane oxidation. The measurements of Y_{CO} and Y_{H2} (corrected) are plotted in figure 12. Neither of the two species should be present in the lean combustion cases. This is seen in the measurements of CO, while the H_2 concentrations show small values that are probably due to experimental error. The levels of intermediate species peak for the rich combustion cases, and show a decline as ϕ increases further. The levels of CO are consistently much higher than the ones seen for H_2, consistent with the presence of the catalyst. The behavior of the major and intermediate species can be better explained by considering the water-gas shift reactions: $CO + H_2O \Leftrightarrow CO_2 + H_2$. These are very important during methane oxidation, and they reach a partial equilibrium at high enough temperatures. The peak observed for Y_{H2O} at $\phi \approx 1.2$ corresponds with a maximum of Y_{CO} at this location, while both Y_{CO2} and Y_{H2} show maxima at around $\phi \approx 1$. These trends correspond to shifts in the predominance of either forward or backward rates of the water-gas shift reactions, which affect CO and H_2O (as well as CO_2 and H2) in similar manner.

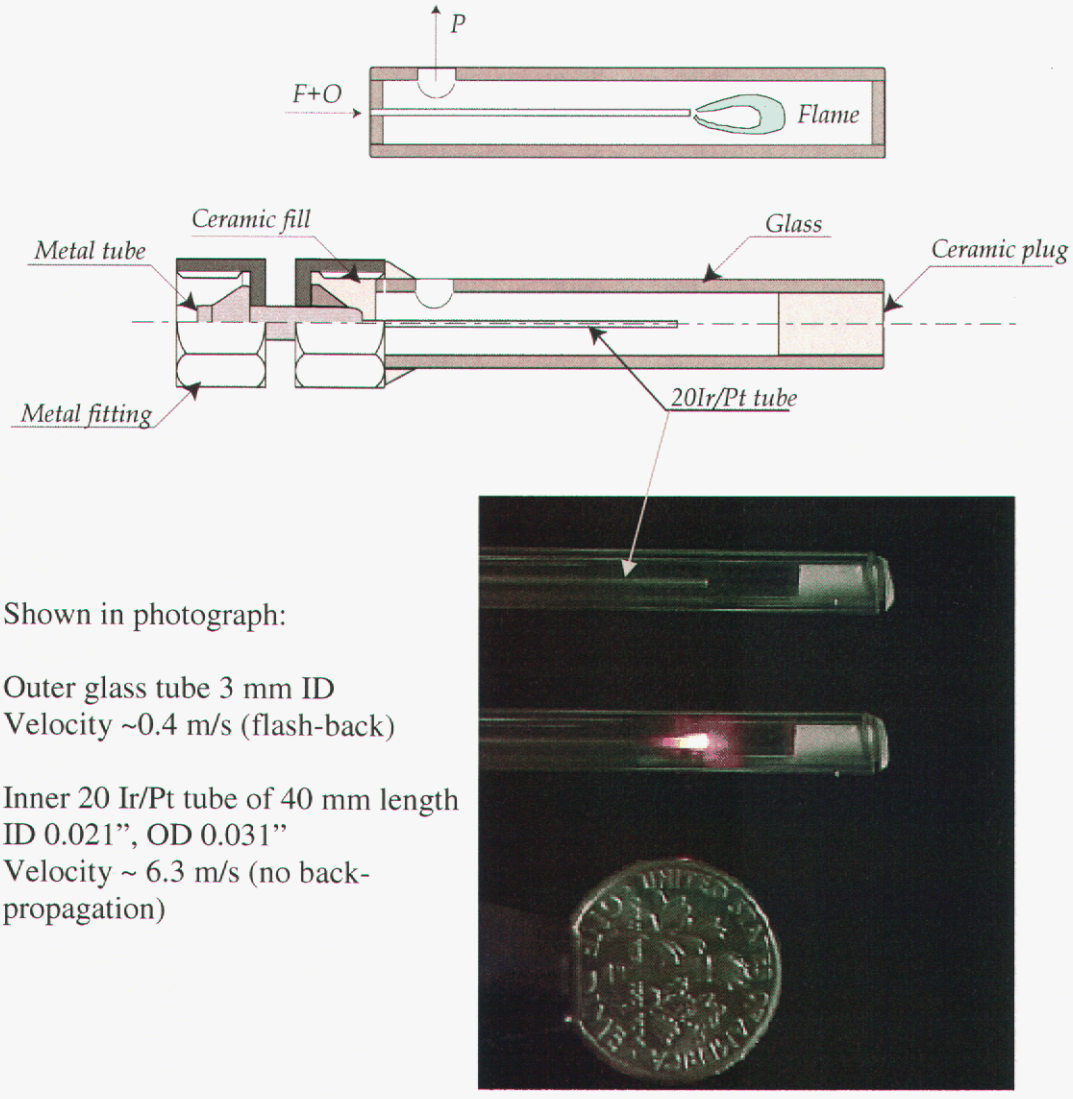

Figure 1. Excess enthalpy combustors. From top to bottom: conceptual drawing of the device, detailed drawing of tube-in-tube implementation, photograph of the working device. Power production under idealized conditions 2.8 W.

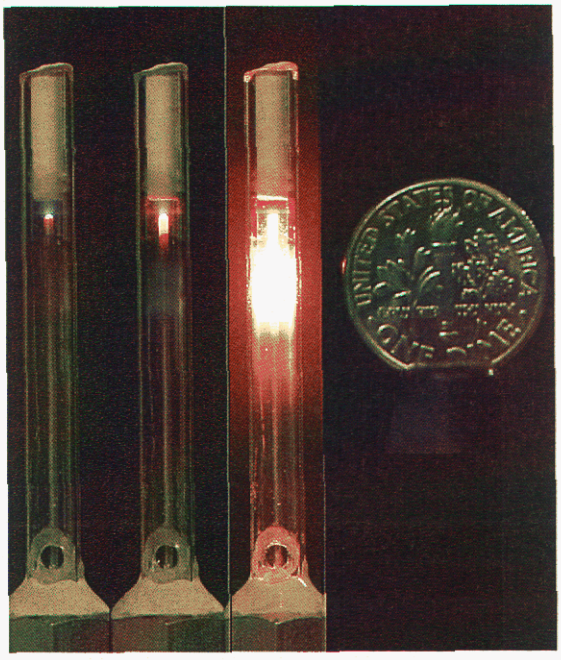

Figure 2. Photograph of a combustor in three different phases of operation. From left to right: ignition by flame flash-back, homogeneous flame at catalyst tip, heterogeneous (catalytic) ignition and combustion.

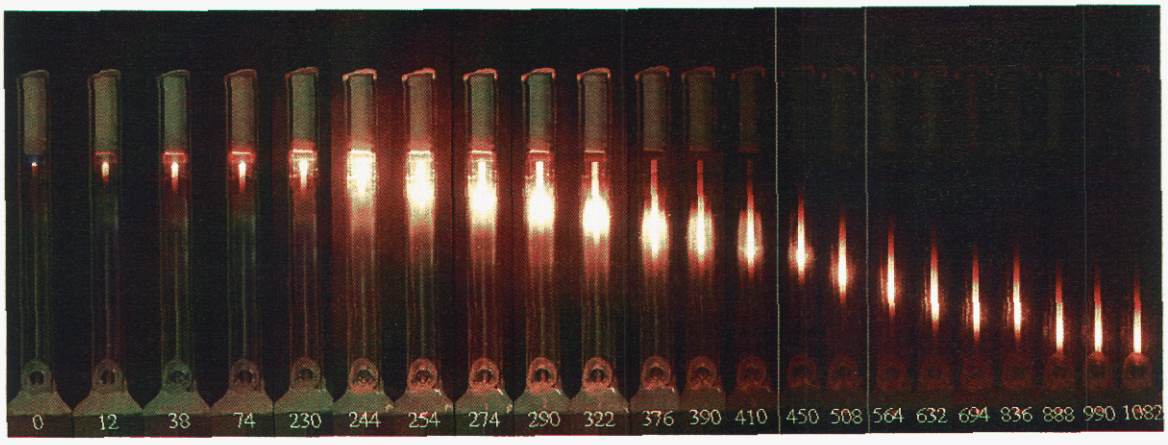

Figure 3. Composite picture of the combustion time sequence in an excess enthalpy combustor. The time in seconds after initial ignition is shown at the bottom of the figure.

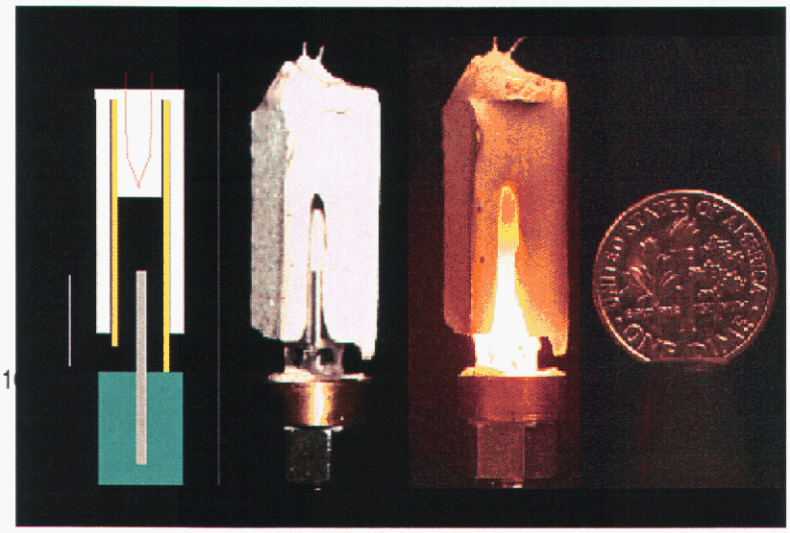

Figure 4. Schematic and photograph of a shielded excess enthalpy combustor. Power production under idealized conditions 5.6 W.

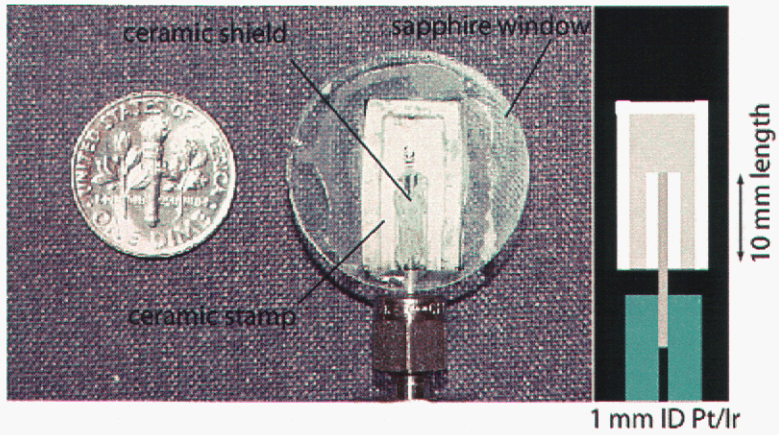

Figure 5. Schematic and photograph of a ceramic 'stamp' combustor. While never operated under such conditions, power production could reach 11 W.

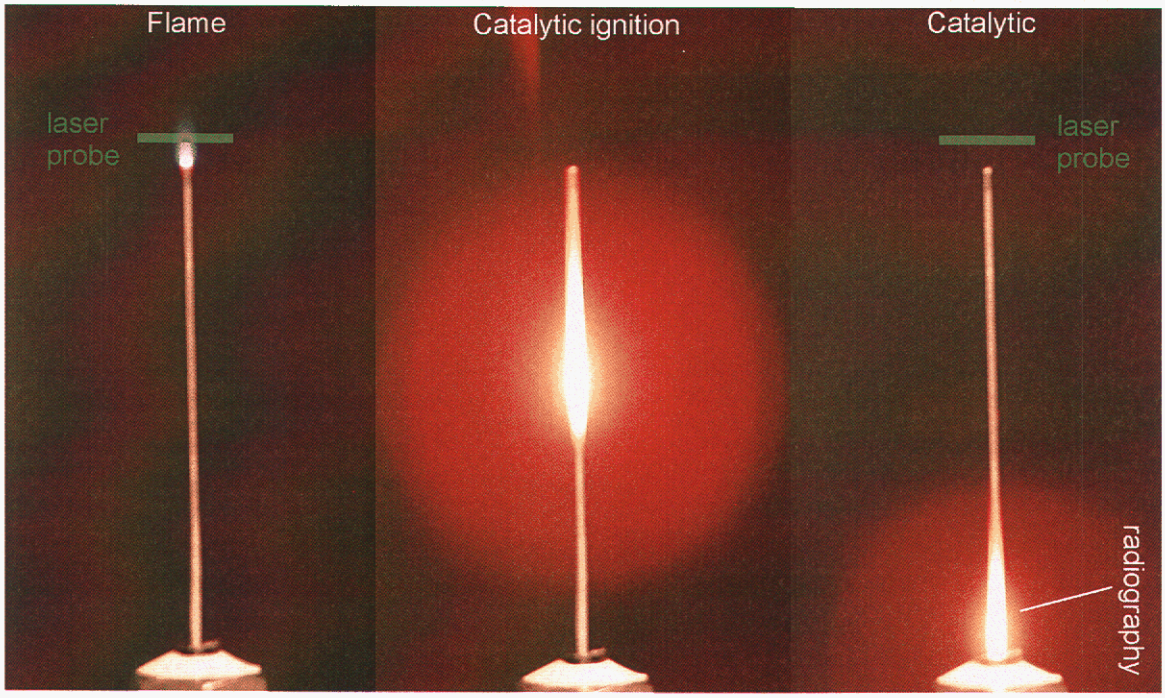

Figure 6. Multiscalar measurements at the tip of a catalytic needle, and radiographic thermometry of the catalyst surface. Left: measurements within the homogeneous flame at the tip of the needle. Middle: catalytic ignition by external heat source. Right: measurement of the products exiting the needle under catalytic burning, in combination with radiography of the metal surface. Probe position at x/d = 4. Relative probe size is drawn by green line.

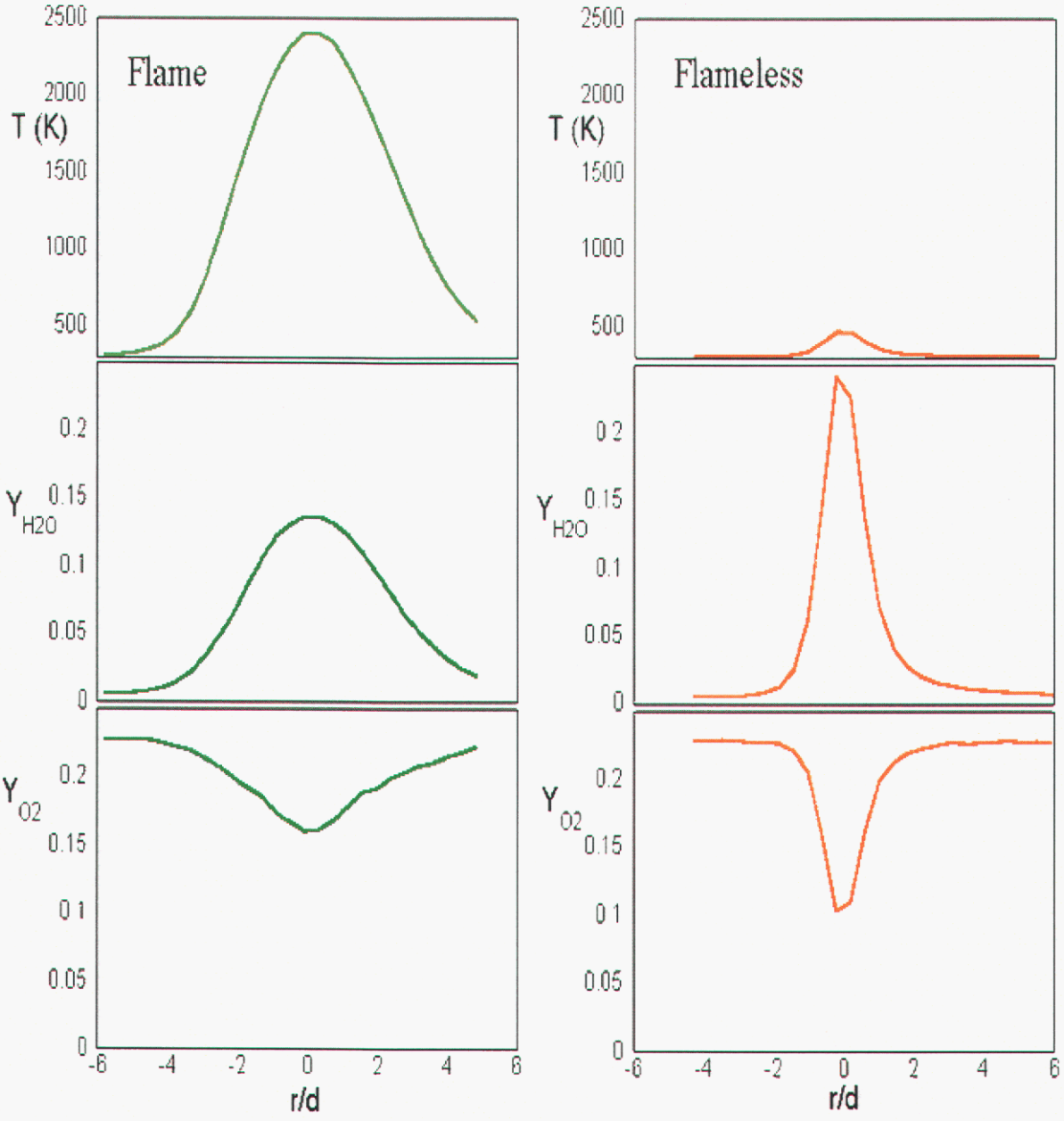

Figure 7. Temperature and major species mass fraction spatial profiles measured by the multiscalar technique for both homogeneous flame (left) and catalytic combustion (right). Measurements correspond to the base stoichiometric case ($\phi = 1$). Dotted line corresponds to centerline.

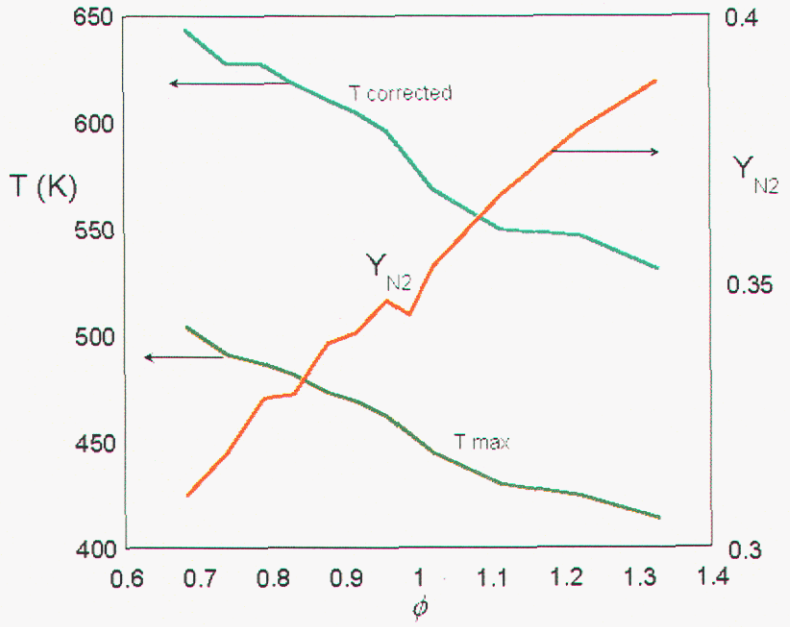

Figure 8. Temperature and nitrogen mass fraction measurements for the catalytic combustion case under varying stoichiometry. Y_{N2} was used to calculate the amount of air entrainment at the centerline and subtract its effect from the measurements. The case for temperature is shown in the figure.

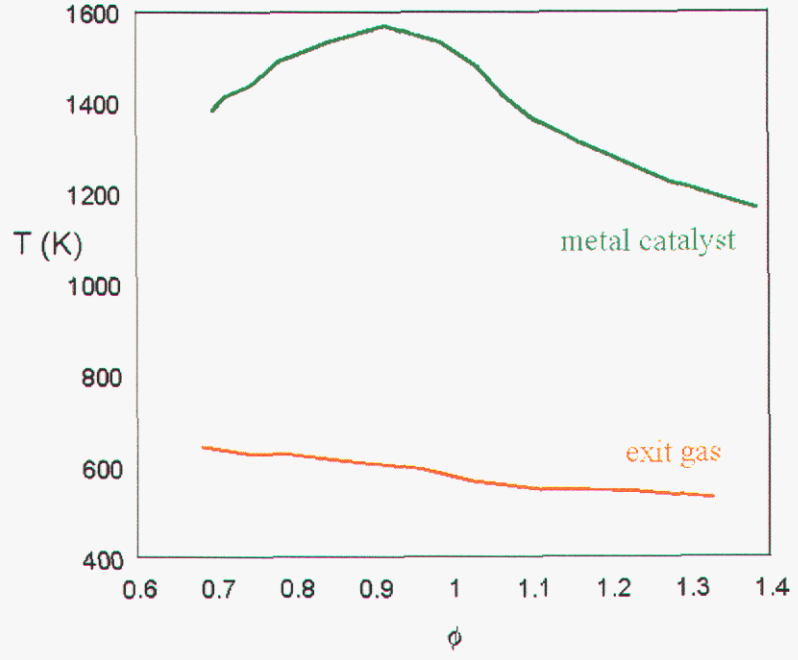

Figure 9. Temperature (maximum, corrected) of the exit gases in the case of catalytic combustion, along with the catalyst metal temperature (maximum) obtained by radiography.

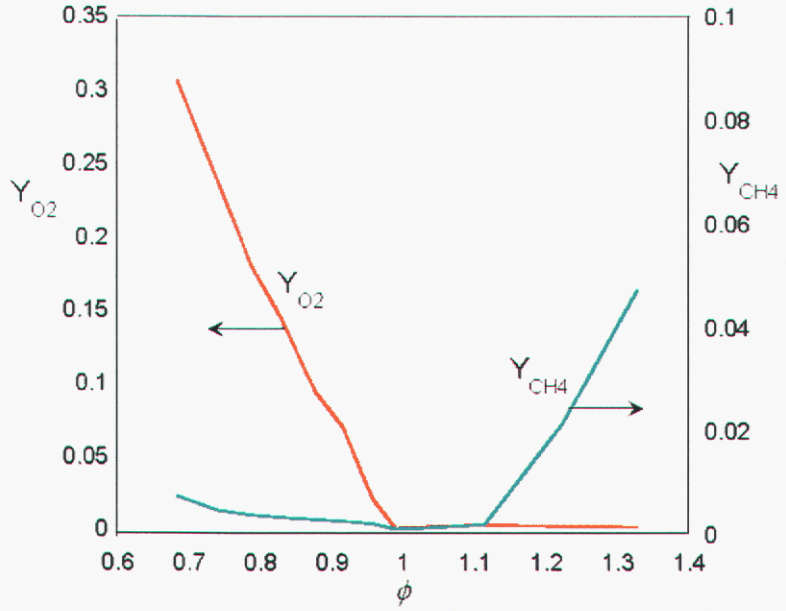

Figure 10. Fuel and oxygen composition as a function of stoichiometry for catalytic combustion.

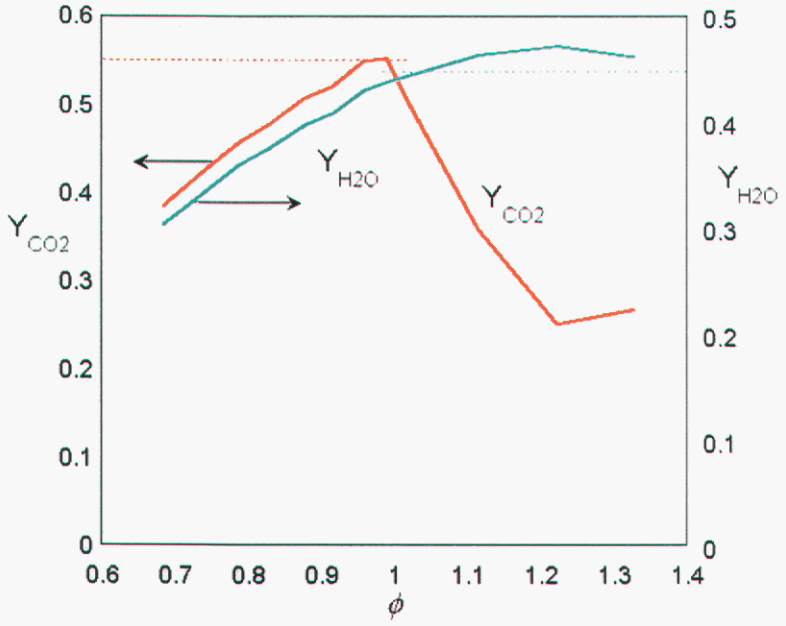

Figure 11. Major product species (CO_2 and H_2O) composition as a function of stoichiometry for catalytic combustion. Dotted lines show equilibrium stoichiometric composition under full burning.

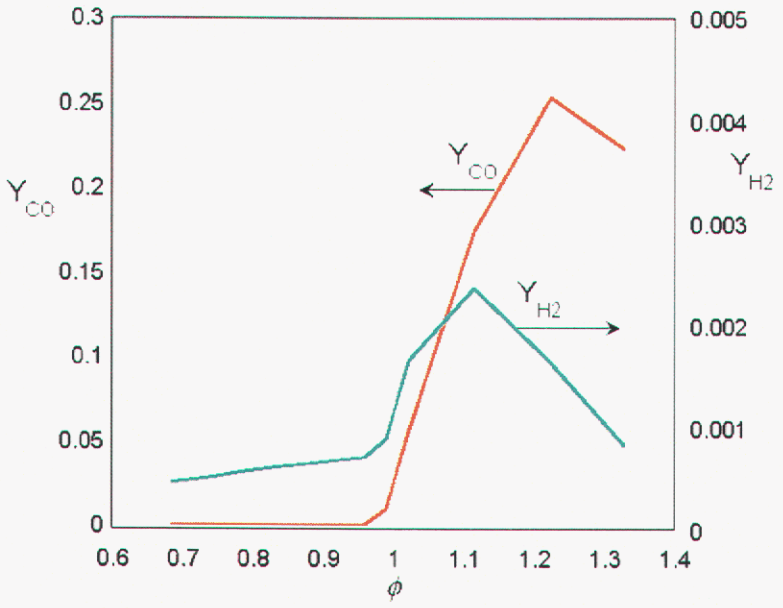

Figure 12. Intermediate species (CO and H_2) composition as a function of stoichiometry for catalytic combustion.

DISTRIBUTION

5	MS 9291	Brent Haroldsen
1	MS 9051	Jacqueline Chen
1	MS 9403	Alfredo M. Morales
1	MS 9401	Michelle A. Hekmaty
1	MS 9401	Karen L. Krafcik
1	MS 9292	Tom Raber
1	MS 9403	Bernice Mills
1	MS 9401	Joseph T. Ceremuga
1	MS 9051	Tarek Echekki
1	MS 9051	Jeremiah Lee
1	MS 9051	Shiling Liu
1	MS 9051	Adonis Karpetis
3	MS 9018	Central Technical Files, 8945-1
1	MS 0899	Technical Library, 9616
1	MS 9021	Classification Office, 8511 for Technical Library, MS 0899, 9616
		DOE/OSTI via URL
1	MS 0188	D. Chavez, LDRD Office, 1011

REFERENCES

[1] Manhattan Scientifics MicroFuel Cell™ Market Analysis presentation, http://www.mhtx.com/

[2] http://www.defense-update.com/features/du-1-04/feature-powering-land-warrior.htm

[3] NATIONAL ACADEMY PRESS, Committee on Electric Power for the Dismounted Soldier, Board on Army Science and Technology, Commission on Engineering and Technical Systems, National Research Council, Energy-Efficient Technologies for the Dismounted Soldier, 1997

[4] S. Feldman, DARPA Palm Power Workshop, November 14-15, 2000, Fort Lauderdale, FL, http://www.darpa.mil/dso/thrust/matdev/palmpower/presentations/feldman_part2.pdf

[5] DARPA FACT FILE, A Compendium of DARPA Programs, April 2002

[6] Martini, William R., Martini Engineering, Stirling Engine Design Manual, Second Edition, January 1983

[7] Dentinger, P. M.; Krafcik, K. L.; Simison, K. L.; Janek, R. P.; Hachman, J., *Microelectronic Engineering*, **61-62**, 1001-1007, 2002.

[8] Hruby, J., "LIGA technologies and applications", *MRS Bulletin*, **26** (4), 337-340, 2001

[9] Kelly, J. J.; Yang, N., Y., C.; Goods, S., H., "High Performance Nickel-Manganese Alloy for Microsystem Applications", SAND2003-8308

[10] Photoresist courtesy of Paul Dentinger, Karen L. Krafcik, and Kelby Simison. The photoresist consisted of 69% of solids SU8 R 50 resin (MicroChem), 3% of solids PAG (phenyl-p-octyloxyphenyl-iodoniumhexafluoroantimonate from GE Silicones) photo acid generator, 10% TIBA (triisobutylamine)/PAG by mole. The TIBA is a 10% solution by mass in PGMEA (Aldrich)

[11] F. A. Lowenheim, Electroplating, 218-219, McGraw-Hill, Inc., New York, 1978

[12] VIEW Engineering (http://www.vieweng.com) and "Inspection Strategy for LIGA Microstructures Using a Programmable Optical Microscope", Joseph T. Ceremuga, Georg Aigeldinger, SAND2004-2289, July 2004

[13] CFD-ACE (U) Module Manual Version 2002

[14] Brown, P. N. and Byrne, G. D. and Hindmarsh, A. C., "VODEPK: A Variable Coefficient ODE Solver", SIAM J. Sci. Stat. Comput., 10-5: 1038--1051, 1989

[15] Tomboulides, A. G., "Direct and Large-Eddy Simulations of Wake Flow: Flow Past a Sphere", Princeton University PhD Thesis, 1993

[16] Tomboulides, A. G. and Lee, J. C. Y. and Orszag, S. A., "Numerical simulation of low Mach number reactive flows", J. Sci. Comp., 12-2:139--167, 1997

[17] Tomboulides, A. G. and Orszag, S. A., "A quasi two-dimensional benchmark problem for low Mach number compressible codes", J. Comp. Phys., 146-2:691--706, 1998

[18] Lee, J. C. and Tomboulides, A. G. and Orszag, S. A. and Yetter, R. and Dryer, F. L. "Transient two-dimensional chemically reactive flow model: fuel particle combustion in a nonquiescent environment", Proceedings of the Combustion Institute 26-2:3059--3065, 1996

[19] Frouzakis, C. E. and Lee, J. C. and Tomboulides, A. G. and Boulouchos, K., "Two-Dimensional Direct Numerical Simulation of Opposed-Jet H2/air diffusion flame" Proceedings of the Combustion institute 27-1:571--577, 1998

[20] Kee, R. J., Rupley, F.M., and Miller, J. A., "Chemkin-II: A Fortran Chemical Kinetics Package for the Analysis of Gas-Phase Chemical Kinetics", SAND89-8009, 1989

[21] Chen, J. H. and Im, H. G., Proc. Comb. Inst., 28:211-218, 2000

[22] Yetter, R. A. and Dryer, F. L. and Rabitz, H., "A comprehensive reaction mechanism for carbon monoxide/hydrogen/oxygen kinetics", Comb. Sci. Tech. 79-1-3:97--128, 1991

[23] Coffee, T. P. and Heimerl, J. M., "Sensitivity analysis for premixed, laminar, steady-state flame", Comb. Flame. 50-3:323--340, 1983

[24] Appel, C., Mantzares, J., Schaeren, R., Bombach, R., Inauen, A., Kaeppelli, B., Hemmerling, B., Stampanoni, A., "An experimental and numerical investigation of homogeneous ignition in catalytically stabilized combustion of hydrogen/air mixtures over platinum," Comb. Flame 128:340-368, 2002

[25] Thermal radiative properties: metallic elements and alloys [by] Y. S. Touloukian [and] D. P. DeWitt. New York, IFI/Plenum [c1970]

[26] Thermal radiative properties: nonmetallic solids [by] Y. S. Touloukian [and] D. P. DeWitt. New York, IFI/Plenum [c1972]

[27] Joseph Peterson Co-worker, Junior in MAE at NCSU who worked on this project in summer 2002